Self-organized Dynamics of Mesoscale Particles and Droplets

A thesis submitted

in partial fulfillment of the requirements

for the degree of

Doctor of Philosophy

by

Sunny Kumar

Department of Chemical Engineering

Indian Institute of Technology Guwahati,

Assam, India

January 2018

C E R T I F I C A T E

It is certified that the work contained in this thesis entitled **"Self-organized Dynamics of Mesoscale Particles and Droplets"**, by Mr. Sunny Kumar, has been carried out under our supervision and that this work has not been submitted elsewhere for a degree.

Thesis Supervisors

Dr. Dipankar Bandyopadhyay
Associate Professor
Department of Chemical Engineering
Indian Institute of Technology Guwahati
Assam, India.

Dr. Ashok Kumar Dasmahapatra
Associate Professor
Department of Chemical Engineering
Indian Institute of Technology Guwahati
Assam, India.

January 2018

ACKNOWLEDGEMENT

Working for PhD has been an unforgettable experience for me and it would not possible without these people.

First and foremost, I would like to thank my thesis supervisors **Dr. Dipankar Bandyopadhyay** and **Dr. Ashok Kumar Dasmahapatra** for giving me an opportunity to perform research on "Dynamics of particles and droplets". I am very grateful to Dr. Dipankar Bandyopadhyay for his continuous guidance, essential advices, and stimulating discussions in the whole duration of my research. In spite of his busy schedule, he has always happily spent time in analyzing my problems and providing the required suggestions for the improvement of the work. I can proudly mention some of his notable qualities such as, patience during work, their depth of perfection and attractive presentation skills, which have always inspired me and will continue to inspire in future also. The experience of working with him will have far-reaching influence in my research and professional objectives in the times to come. I consider it an honor to work under him.

I would like to express my deepest gratitude to Dr. Ashok Kumar Dasmahapatra for his insightful comments, suggestions, and thoughts on my research work and spending the required time with me. His continuous encouragement and support has always given me a lot of inspiration to carry out this research work successfully.

I would like to thank my doctoral committee members, **Dr. Mahuya De, Dr. G. Pugazhenthi,** Department of Chemical Engineering and **Dr. Debasish Das**, Department of Biosciences and Bioengineering, for their valuable suggestions for the successful implementation of the thesis objectives.

My sincere thanks to my senior lab-members, **Mr. Amit Kumar Singh**, **Mr. Seim Timung, Mr. Bolleddu Ravi,** and **Mrs. Chitrita Kundu** for their co-operative assistance in learning the basics concepts and providing me constant source of encouragement throughout my stay at IIT Guwahati.

I am also thankful to present research group members **Mr. Bhaskarjyoti Sarma, Ms. Abhijna Das, Mr. Abhinav Sharma, Mr. Joydip Chaudhuri, Mr. Mitradip Bhattacharjee, Mr. Nilanjan Mandal, Mr. Saptak Rarotra, Ms. Satarupa Dutta, Ms.**

Snigdha Chakraborty, Mr. Vineet Kumar, Mr. Surjendu Maity, Ms. Tamanna Bhuyan, Mr. Abir Ghosh, Mr. Pritam Roy, Mr. Ankur Pandey, Mr. Manash Pratim Borthakur, Ms. Binita Nath and **Mr. Viswanath Pasumarthi.**

I cannot forget to thank my friends **Dr. Dharamashi Rabari**, **Mr. Amit Srivastava, Dr. Himadri, Mr. Rahul Patwa, Mr. Rahul Ramteke, Mr. Shyam Yadav** and **Mr. Suman** for the lovely support in making my stay at IIT Guwahati memorable.

I also acknowledgement the support from the **Analytical Laboratory** in Chemical Engineering, and **CIF** at IIT Guwahati for characterization facilities.

Above all, I would like to thank my **parents, and family members** for their love and support throughout for everything. Finally, my wife **Neha** deserve a special mention for her love and confidence in me and sharing many of my workloads during the time of need.

I dedicate this thesis to *My Family.*

SUNNY KUMAR

SYNOPSIS

Self-organized Dynamics of Mesoscale Particles and Droplets

Intelligent artificial robots are designed and developed to accomplish routine activities of daily human life. They are envisioned to alleviate the human work load, which are mainly repetitive in nature, in the diverse areas such as cleaning, washing, managing, communicating, computing, and treatment, in order to improve the quality of human life and their expectancy. The robots are also tipped to be employed for advanced technological events such as high-precision sensing, interaction with humans, operations of aircrafts or artilleries, energy harvesting, and environmental remediation. Interestingly, robot manufacturing is often inspired from the various living objects present in the nature, such as humans, plants, extra-terrestrial elements, animals, insects, bacteria, viruses, and parasites, among others.

The present era has witnessed the use of robots having different length scales ranging from a few meters to the level of a few nanometers targeting different applications. For example, a collection of macroscopic swarm ‘kilobots’ with programmable controllers and locomotive capacity can show collective artificial intelligence such as sync, transport, assembly to realize routine jobs. On the other hand, self-propelling micro or nanoscopic robots, also popularly known as micro or nanobots, find important futuristic applications in the domains of targeted drug delivery, payload transport, therapeutics, diagnostics, imaging, and high precision sensing, among others.

In this regard, the fabrication of the micro or nanoscale robots undergoing controlled migration is one of the very challenging fields of research. Largely, the micro or nanomotors can be classified into hard-non-deformable and soft-deformable types. The non-deformable micro or nanomotors are mechanically tough and in general composed of

metals or metal-alloy, hard polymers, piezoelectric or other smart materials with higher elastic modulus. In contrast, the soft micro or nanobots is capable of changing their shape during migration and are composed of liquid droplets or soft-viscoelastic polymers or hydrogels with relatively smaller elastic rigidity. Interestingly, the motions of the soft or hard mesoscale self-propelling objects are very often controlled by different *in situ* or remote guidance such as chemical potential, photonic excitation, electromagnetic field, acoustic waves, and thermal energy, among others.

An extensive literature survey suggested that there are many areas, which require immediate attention for a rapid progress of the design and development of commercial micro or nanobots. This include, (i) design and development biocompatible 'superbots' – micro or nanobots capable of self-propulsion through multiple external stimuli such as chemical potential, electric or magnetic fields; (ii) use of soft and hard materials to design and develop superbots undergoing chemotaxis, galvanotaxis, or magnetotaxis; (iii) study the effects of the fluid properties on the different motions of the microbots; (iv) develop theoretical and computational models to explain the various features of their movement; (v) apply the self-propelling motions of the soft and hard motors for payload transport, drug delivery, or emulsification; (vi) improve the fundamental understanding of the response of a soft or hard motor in presence of chemical, electric or magnetic stimuli.

In view of the above, the present thesis reports the design and development of a host of biocompatible soft and hard microbots composed of graphene coated on glass microbeads, metal nanoparticles coated on glass microbeads, oil or water droplets. These microbots are capable of showing controlled motion under the influence of either *in situ* chemical potential gradient or externally applied electric or magnetic field. While the hard 'superbot' composed of graphene coated glass bead have shown chemotaxis and galvanotaxis under the influence of *in situ* chemical potential gradient and externally

applied electric field, deposition of a trace of iron nanoparticles on the surface of this motor infuses the capacity to move under magnetic field to demonstrate magnetotaxis. Further, the soft 'liquibots' such as the 'waterbot' and the 'oilbot' have been prepared infusing paramagnetic and diamagnetic salts into the water or the oil droplets. The salt laden oilbots and waterbots showed curious push and pull magnetotactic motility under the remote magnetic guidance. Fascinatingly, under the sole influence of electric field, oil droplets on a continuous water bath have shown interesting galvanotactic locomotion such as oscillation, spreading or ejection while under Lorenz force the same system showed clockwise and counter clockwise rotational locomotion. In addition, a droplet breaking mechanism under a chemical stimulus has been uncovered, which is capable of generating a microemulsion from a macroscopic water droplet in a single step process. In such a scenario, the droplet shows interesting spreading and dewetting of the macroscopic droplet before forming metastable fluidic structures such as toroid, liquid sheet, or high aspect ratio liquid thread, among others.

The aforementioned prototypes and their response to the external stimulus can be employed for a number of futuristic applications. For example, (i) the graphene coated glass microbots can perform payload transport, drug delivery or as a stent for cleaning of blood vessels, (ii) the water or oilbots can be employed for drug delivery applications, (iii) the rotating or oscillating incompressible droplets can be employed for pumping applications inside the microfluidic devices, (iv) the chemical stimuli induced droplet breakup can be employed as a single step methodology to form micro or nanoemulsion, (v) the droplet breakup experiments can be employed to synthesize miniaturized droplets with very high surface-to-volume ratio. In what following, the details of the objectives of the thesis discussed has been divided into five following chapters before summarizing in

the sixth one. Thereafter, we provide a brief detail on the publications, patents, and conferences as an outcome of the thesis work.

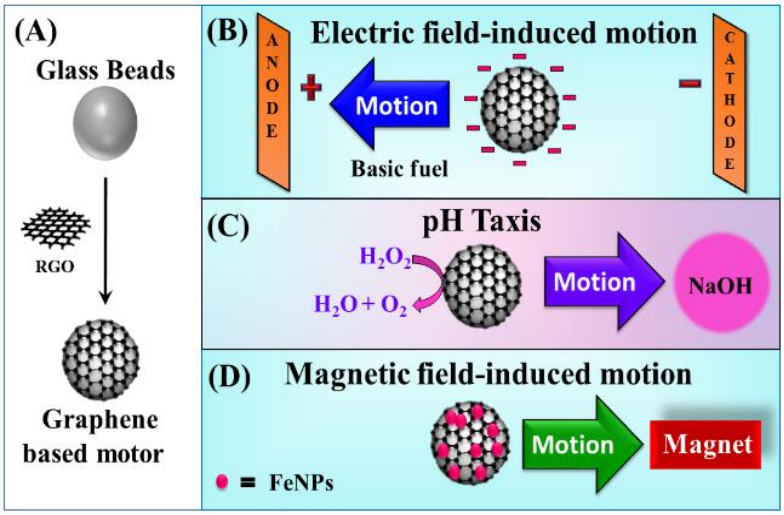

Figure 1. Motions of graphene superbots under electric field, chemical potential gradient, and magnetic field.

Graphene is a recently invented 2D material, which has exceptional properties such as high surface area and young modulus suitable for making micro or nanobots. Thus, in the **Chapter 2,** we report the synthesis of a versatile graphene coated glass microswimmer, which displayed directed motions under the influence of applied electric field, chemical potential gradient and external magnetic field, as shown in the Figure 1. The directed chemical locomotion took place from the region of lower to higher pH with speed ~13 body lengths per second due to asymmetric catalytic decomposition of dilute hydrogen peroxide across the motor surface. The negative surface potential of graphene-coated motor developed an electrical double layer in an alkaline medium, which in turn engendered electrophoretic mobility towards anode when the external electrostatic field was applied. Inclusion of sparsely populated ferromagnetic iron nanoparticles on the surface of the motor offered the magnetic remote control on the motion. The coupled *in situ* and external controls enabled the motor to develop complex motions in diverse open and confined environments. For example, the motor could approach, pick-up, tow, and

release a heavy cargo inside microchannel. Remarkably, the motor (~67 μg) could successfully drive out a ~1000 times heavier payload (~0.67 mg) displaying the ability to overcome the drag force of ~2619 pN with the help of coupled *in situ* and remote guidance.

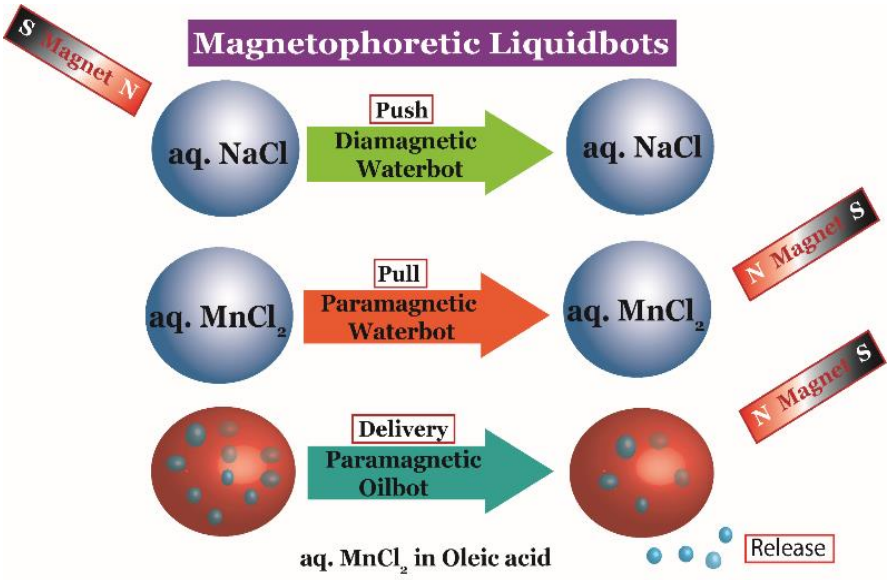

Figure 2. Schematic illustration of liquibots undergoing magnetic field induced motion.

Microdroplets of oil and water can be employed to fabricate soft micro or nanobots, which are yet to appear in the literature. In the **Chapter 3**, it is shown that the liquid droplets loaded with paramagnetic or diamagnetic salts, namely liquibots, can show controlled migration inside a fluid medium and on slippery solid surfaces under remote magnetic guidance, as shown in the Figure 2. The water or oilbots of size ranging from a millimetre to a few microns showed facile attraction, repulsion, division, and coalescence when guided by a magnetic field. The speed of the liquibots could be tuned by varying the size, salt loading, and magnetic field strength. While the paramagnetic liquibots migrated towards a magnet with a velocity as high as ~8 body lengths per second, the diamagnetic one migrated away from the field with a maximum velocity of ~1 body lengths per second. The liquibots transported and delivered commercially available drugs to targeted

locations showing their potential as drug-delivery vehicles. Remarkably, the experiments showed the utility of the liquibots in digital microfluidics because they moved easily on slippery solid surfaces. For example, a waterbot was split into many droplets on an oil coated solid surface before forming the patterns resembling polygons under magnetic guidance. Further, the liquibots based Packman™ game could also be played with the help of magnetic guidance. The extent of control demonstrated on the motions of the remotely guided liquibots could be useful in diverse futuristic applications including drug-transport, digital-microfluidics, and droplet-electronics.

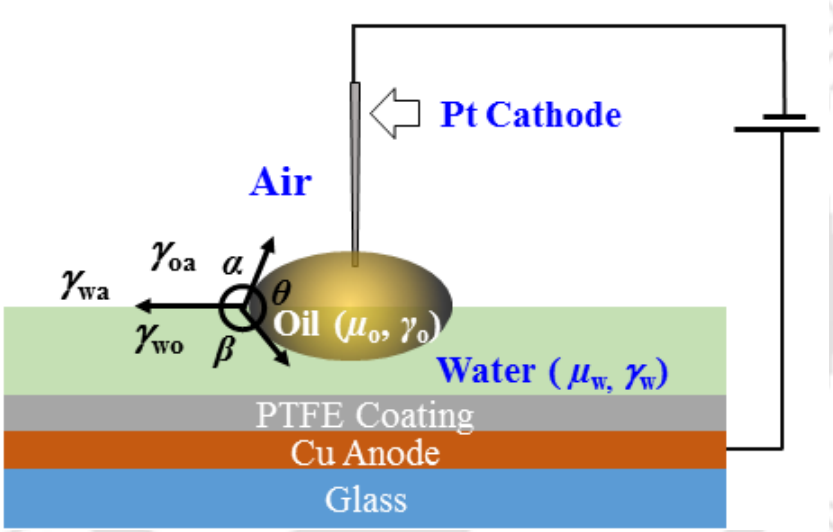

Figure 3. Schematically show the for experimental setup for the electrowetting on a liquid (EWOL) layer.

In the **Chapter 4**, it is shown that the application of an electric field on an oil droplet floated on the surface of a deionized water bath showed interesting motions such as spreading, oscillation, and ejection, as schematically shown in the Figure 3. The electric field was generated by connecting a pointed platinum cathode from the top of the oil droplet and a copper anode coated with polymer from the bottom of the water layer. The experimental setup mimicked a conventional electrowetting setup with the exception that the oil was spreading on a soft and deformable water isolator. While at relatively lower

field intensities, we observed spreading of the droplet, at the intermediate field intensities the droplet oscillated around the platinum cathode before ejecting out at a speed as high as ~ 5 body lengths per second, at even stronger field intensities. The experiments suggested that when the electric field was ramped up abruptly to a particular voltage, any of the spreading, oscillation, or ejection of the droplet could be engendered at lower, intermediate and higher field intensities, respectively. However, when the field was ramped up progressively by increasing a definite amount of voltage per unit time, all three aforementioned motions could be generated simultaneously with the increase in the field intensity. Remarkably, when the aforementioned setup was placed on a magnet the droplet showed a rotational motion under the influence of the Lorentz force, which generated because of the coupling of the weak leakage current with the externally applied magnetic field. The spreading, oscillation, ejection, and rotation of the droplet were found to be the functions of the oil-water interfacial tension, viscosity, and size of the oil droplet. We developed simple theoretical models to explain the experimental results obtained. Importantly, rotating at a higher speed broke the droplet into a number of smaller ones owing to the combined influence of the spreading due to the centripetal force and the shear at the oil-water interface. While the oscillatory and rotational motions of the incompressible droplet could be employed as stirrers or impellers inside the microfluidics devices for mixing applications, the droplet ejection could be employed for futuristic applications such as payload transport or delivery of drugs.

In the **Chapter 5**, it is shown that a simple chemical trigger can self-organize an oil droplet on a water surface into a toroidal shape in absence of any rotational influence. The abrupt reduction of interfacial tension due to the chemical trigger stimulates a rapid spreading of the oil droplet on the water surface to develop the metastable toroidal structure. The experimental setup is schematically shown in the Figure 4.

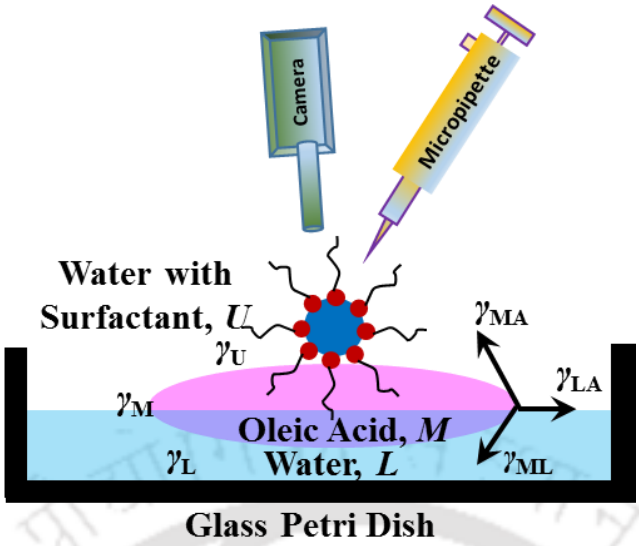

Figure 4. Schematically shows the experimental setup in which oil droplet floating on water while a water with surfactant trigger is introduced from the top of the oil droplet.

High speed imaging of the process uncovers the inclusive dynamics consisting of seven stages: (i) droplet spreading, (ii) formation of toroid connected to a thin liquid-sheet, (iii) separation of the toroid and liquid-sheet, (iv) dewetting of the liquid-sheet on the water surface to form microdroplets, (v) expansion of the toroid, (vi) breakup of the toroid into threads, and (vii) formation of microdroplets from the toroid. A parametric study with the variations in the viscosities of the fluids and the interfacial tensions at the fluid boundaries uncover two different pathways of toroid formation: laminar mode – where the symmetric toroids are observed at lower Reynolds (Re) number and turbulent mode – formation of the asymmetric toroids at a higher *Re*. Simple theoretical models have been developed based on the thin film equations of a liquid droplet resting on a fluid surface and subsequently a linear stability analysis is performed to predict, (i) the cross-sections of a toroid resting on a liquid surface under the varied experimental conditions and (ii) length scale of the disintegration of the toroids on a soft-deformable liquid surface. Interestingly, at the intermediate stages, the toroid formation phenomenon is also associated with an oil-sheet formation on the water surface. The proposed methodology to develop the

metastable fluidic objects such as toroids, sheets, or threads and their breakup can be useful for a number of applications such as emulsifiers, 3D-printing, droplet or digital microfluidics, microreactors.

In summary, this thesis uncovers a variety of techniques to synthesize soft and hard micro or nanobots capable of directional migrations towards various *in situ* and external stimuli such as chemical potential gradient, electric or magnetic field. A host of theoretical, computational, and experimental pathways have been employed to understand the origin of the motions of these mesoscale systems under various conditions. The studies also find out the applicability of these systems in the sensing, payload transport, drug-delivery, energy harvesting, emulsification, 3D-printing, miniaturization, and biomedical applications, among many others. In future, the reported works can be extended to, (i) *in vivo* experiments for targeted drug delivery, (ii) directional motions of multiple micro nanobots for a common objective; (iii) infusion of the decision making capacity inside the robots mimicking the bacterial or viral migrations; (iv) development of micropumps based on oscillating or rotating incompressible droplets; and (v) miniaturization of size of soft motors, loading of life saving drugs, and targeted *in vivo* delivery of the same for biomedical applications.

CONTENTS

LIST OF TABLES

LIST OF FIGURES

the surface tension of the respective phases. Images II(a) – II(e) show the top view of the spatiotemporal evolution of the oleic acid droplet when C_S^U was 0.05 %. Images (a) initial configuration (0 s), (b) droplet spreading (0.58 s), (c) sheet and toroid formation (1.9 s), (d) toroid formation and breaking of sheet (4.2 s), and (e) droplets from toroid-braking (10.5 s) where the scale bar is 1 cm. The images III(a) – III(c) show the variation in the maximum diameter (D_T^m) of the toroid when C_S^U was, 0.1%, 0.5%, and 1%, respectively. Plot III(d) shows the variation in D_T^m with C_S^U. The images IV(a) – IV(c) show the variation in the number of droplets (N_d) formed due to the toroid-breaking when C_S^U was, 0.1%, 0.5%, and 1%, respectively. The plot IV(d) shows the variation in N_d with C_S^U.

5.4 Images (a) – (e) in the row (I) show the steps to toroid formation of an oleic acid droplet (layer *M*) on water surface (layer *L*) with a pentanol trigger from the top (layer *U*). Images (a) – (e) show snapshots after 49 ms, 58 ms, 64 ms, 90 ms, and 110 ms, respectively, when ϕ_M = 20 µl and ϕ_U = 5 µl. The scale bar shown on the image I(e) is 1 cm. Images (a) – (e) in the row (II) show the time evolution of the magnified zone of an oil-sheet breakup under pentanol trigger after, 32 ms, 104 ms, 160 ms, 188 ms, and 46 ms, respectively, when μ_r = 27, ϕ_M = 1 µl and ϕ_U = 0.5 µl. The scale bar shown on the image II(e) is 1 mm. 109

5.5 Plot (a) shows the variation of the normalized diameter of the spreading front of the oil droplet, $\bar{d}_M = d_M / d_M^0$, with time (*t*) for the surfactant-water (SW) chemical trigger when C_S^U was 0.5 %. Here d_M and d_M^0 are the variable and initial diameters of the oil droplet. Plot (b) shows variation of the $\bar{d}_M$ with *t* for the pentanol chemical 111

trigger. Plot (c) shows the variation of the $\bar{d}_M$ with t when $\mu_r = \mu_M / \mu_L$ was varied for the chemical trigger, C_S^U = 0.5 % and pentanol. Plot (d) shows the variation in the Weber number (We, $\rho_M v_M^2 d_M / \gamma_M$) with Reynolds number (Re, $\rho_M v_M d_M / \mu_M$) at different μ_r for the chemical trigger, C_S^U = 0.5 % and pentanol. Plot (e) shows the variation in We with Re for different chemical triggers such as C_S^U = 0.05% – 1%, methanol, ethanol, propanol, and pentanol. Plot (f) shows the variation in the capillary number (Ca, $\mu_M v_M / \gamma_M$) with Re for two different middle layers, hexadecane oil and oleic acid, with the chemical trigger pentanol. In all the plots, ϕ_M = 20 µl, ϕ_U = 5 µl, and μ_M = 1 mPa s and for plot (f), μ_L = 3 mPa s.

5.6 Front view or cross-sectional view of the toroid where the lower liquid layer (*L*) film and the combined lower and middle (*M*) liquid layer film thicknesses are denoted by h_1 (r, t) and h_2 (r, t), respectively. The mean film thickness of the lower layer is h_{10}. Inner and outer radii of the middle liquid layer are denoted by r_1 and r_2 (> r_1), respectively. The contact angles of the both middle and lower liquid layers with the mean lower film thickness at the inner edge [outer edge] are specified as θ_1 and θ_3 [θ_2 and θ_4], respectively. Image (a) show the Side view of the toroid and upper part and lower part of toroid at 45°, Change Shape of the toroid in Plot (b) shows the contact ratio θ_r with the surface tension $\gamma_{R,}$ Plot (c) Thickness verses height of the toroid varying with initial volume of φ_M = 20, 50, 100, 150 µl, μ_L=0.001 pa. s, ρ_L= 1000 kg/m^3, C_S^U = 0.5 %, ϕ_U=5µl, γ_{ML}= 48 and γ_{MA} =32 mN/m^2, Plot (d) show the experimental thickness of toroid different time evolution, μ_L=0.001 pa. s, ρ_L= 1000 kg/m^3, γ_{ML}=48 and γ_{MA} =32 mN/m^2, C_S^U = 0.5 %, ϕ_M=20µl, ϕ_U=5µl, Plot (e) shows the spacing between the droplet for ratio of different thickness / toroid 114

keeping the SW trigger volume ϕ_U = 5 µl and ϕ_M = 20 µl. Images in the columns (b) – (d) show the snapshots of the time evolution of a toroidal object when μ_r was varied from 27 and 0.9 keeping the pentanol trigger volume ϕ_U = 5 µl and ϕ_M = 20 µl. The rows (I) – (III) show the introduction of the chemical trigger, the maximum diameter of the toroid formed, and breaking of the toroid into droplet, respectively. The images (e) – (g) show the variations in N_d, D_T^m, λ / w, and λ / r with μ_r for surfactant trigger (0.5% v/v C_S^U). The scale bar shown in the image I(a) corresponds to 5 mm.

5.10 The plot (a) shows the variation in the number density of holes (N_h / A) with *t* when the oil-sheet and oil-toroid separate from each other under the pentanol trigger scale, as shown in the row (I) of the figure 5.3. The plot (b) shows the typical number of droplets per unit area (N_d / A) and their average size (D_d) distribution due to the breakup of the oil-sheet, as shown in the row (I) of the figure 5.3. The plot (c) shows the variation in the number of beads per unit length of the contact line (N_b / L_c) with *t* when the oil-sheet dewet the water-sublayer, as shown in the row (II) of the figure 5.3. The plot (d) shows the variation in the hole-radius (R_h) with time *t* for three different holes when the oil-sheet dewet the water-sublayer, as shown in the row (II) of the figure 5.3. The experimental conditions for this plot was kept similar to as mentioned in the row (II) of the figure 5.3 as, μ_r = 27, ϕ_M =1 µl, and ϕ_U = 0.5 µl.

NOMENCLATURE

h_0	Height of the layer (m)
d	Distance between the electrodes (m)
D	Normalized droplet diameter
t	Time (s)
x , y , z	Direction x-axis, y-axis, z-axis
B	Magnetic field (T)
$C_{Mn,}$ C_{Na}	Concentration of $MnCl_2$ or NaCl in water (M)
Mw	Molecular weight
k_i	Effective rate constant (s^{-1})
$F_{d,}$, F_L	Drag force, Lorenz force (N)
L	Amplitude of oscillation (mm)

Greek letters

μ (μ_i)	Viscosity of the liquid (Viscosity of the i^{th} layer) (Pa s)
γ_M , γ_L , γ_U	Surface tension, M- middle layer, U- upper layer, L-lower layer (N/m)
γ_{ML}	Interfacial tension (N/m)
ε_0	Dielectric permittivity of free space (Fm^{-1})
ε_i	Dielectric constant of the i^{th} layer
ψ , ψ_0	Applied voltage between the electrodes (V)
ω	Speed of rotation (deg/s)
ϕ	Volume of droplet (ml)
χ	Magnetic susceptibility
ρ	Density of the fluid (kg/m^3)

ξ	Zeta potential (mV)
λ	Spacing between the droplet (m)
η	Magnetic susceptibility of vacuum (NA^{-2})

Acronyms

DC	Direct current
CNT	Carbon nanotubes
EWOL	Electrowetting on liquid
FESEM	Field Emission scanning electron microscopy
FeNP	Iron nanoparticles
FeNP@RGO	Iron nanoparticle impregnated reduced graphene oxide
GO	Graphene oxide
PTFE	Polytetrafluoroethylene
PDMS	Polydimethylsiloxane
RGO	Reduced graphene oxide
VSM	Vibrating sample magnetometry
XRD	X ray diffraction
W/O	Water in oil

Dimensionless

Ca	Capillary number
Re	Reynolds number
We	Weber number

Chapter 1

Introduction

1.1 OVERVIEW

A machine is an artificial engineering device performing a sequence of jobs with the help of different forms of energy such as chemical, thermal, or electrical, among others [1]. They are often designed and developed after taking inspiration from various living objects in nature such as animals, birds, insects, bacteria, viruses, and parasites [2-4]. The machines are termed as robots when they perform activities of repetitive nature mimicking the human actions or perform jobs dictated by the human while in the close proximity with them. The robots can be of diverse size ranging from a few meters [5] to the level of few nanometers. The macroscopic robots are envisioned to accomplish complex targeted jobs defined by humans, for example, a surgery with improved efficiency, safety, state-of-art stitching, force sensing, and high-precision positioning of the probes and cutters are expected to be done by humanoid robots [6,7]. In the similar lines, micro or nanoscopic particles or droplets are expected to perform important futuristic activities such as digital microfluidics, on-job-sensing and heling, targeted drug-delivery, bio-synthesis, bio-computation, energy harvesting, and biomedical operations [8].

In view of the above, of late, the fabrication of micro or nanoscale motors and their controlled motion have emerged to be a very promising field of research [9]. The micro or nanomotors are in general prepared from different metal or polymer nanoparticles, liquid metal, salts, or biomolecules [10]. In near future, these miniaturized self-propelling artificial objects are anticipated to contribute significantly in the field of targeted drug delivery, non-invasive therapeutics and imaging, and high-precision sensing, among others [11,12]. Micro and nanomotors are designed to perform selected mechanical movements, for example, rotation, rolling, shuttling, delivery, contraction, and collective behavior, in response to either *in situ* or external stimulus [13]. They are built from a few micro and nanoscale

components, functionalized biologically or chemically and operated using various energy sources such as, light, magnetic fields, surface tension or thermal gradients, electric fields, or ultrasonic acoustic waves, among others [14]. The micro or nano objects are also pertinent to various other upcoming engineering trends such as nanomotor lithography, dynamic imaging, and analytical measurements [15,16]. Largely, based on their materials of construction, the micro/nano motors can be classified into biological and artificial types in which further classification can be made based on their mechanical strength, namely, the hard and soft motors.

1.1.1 Biological and Artificial motors

The naturally abundant biological motors can be of many different types such as the DNA motors, cell cytoskeletons, enzymes, bacterial, viruses, and other microorganisms [17-19]. However, biomaterials have also been employed to develop artificial self-propelling objects in the recent years. For example, a single DNA molecule has been used as an artificial self-propelling nanomotor [20], having tetraplex or duplex conformations. The motion of such DNA nanomotor was found to function efficiently in solution as well as on nanoparticle surfaces. Apart from DNA, the enzymes [21] has also been used to develop chemiosmotic thrust for the fluid flows [21, 22]. Until now, many different enzymatic reactions (viz., catalase, lipase, urease, and glucose oxidase) generated the fluid flow in which the pumping velocity increased with increasing substrate concentration and reaction rate [23]. These rechargeable pumps might enable the design of futuristic enzyme-based devices that act both as sensor and pump. Further, the singular biomolecules have also been employed as motors [24], which led to the discovery rewarded with Nobel Prize in Chemistry [25]. In 2017, the scientific community have also witnessed the development of nano-car, which achieved 150 nm runway under scanning tunneling microscope at ~ 95 nm/hour speed [26].

1.1.2 Solid motor

In comparison to the biomotors, the mechanically non-deformable solid motors at the micro or nanoscale have been prepared by using different metals, polymers, and nano materials, which could be of different shapes and size [27, 28]. For example, the metal microparticle of Al-Pd Janus microspheres could show autonomous propulsion at high speeds (~200 μm s^{-1}) and long lifetimes (~8 min) inside peroxide fuel [29]. Lee et al. 2014 [30] synthesized ~30 nm artificial (Pt−Au) Janus nanoparticles (JNPs), which could catalyze the decomposition of hydrogen peroxide for its propulsion apart from showing the auto-electrophoresis. The polymeric motors [31] decorated with iron nanoparticles on the surface could also undergo a pH directed taxis inside a bath of peroxide fuel. The pH-directed motion of the motor was influenced by the decomposition of H_2O_2 in the bulk of the solution as well as by the nanoparticle catalyst. The motion of these catalytic motors could remotely be controlled by 'external' magnetic field induced migration in addition to the 'internal' pH driven motion. The platinum decorated graphene oxide [32] sheets could self-propel as microjet engine by ejecting O_2 bubbles while decomposing peroxide fuel. Balloon-like MnO_x–graphene crumples [33] was also synthesized by an ultrasonic spray pyrolysis method. It may be noted here although we have discussed only a few varieties of solid motors pertinent to the thesis, there are lots of other developments related to this area ably summarized in some of the recent reviews [34-36].

1.1.3 Soft motor

Apart from the solid motor, in recent times, the liquid droplets have been emerging to be another alternative as soft motors having higher degree of flexibility and functionality. Fabrication of miniaturized droplets and controlling their motion have far reaching consequence in the development of next-generation microfluidic devices, drug delivery

devices, digital microfluidic, liquid transporters, and energy harvesters [37]. In this regard, fabrication of micro or nanoscale droplets exploiting the instabilities of metastable liquid sheets, threads, toroids, or ellipsoids have also been explored since ages. For example, experiments by Plateau to develop toroidal fluidic object on liquid bath improved by the Pairam [38] has been perhaps some of the excellent examples in this direction [39,40]. The spreading, actuation, and motion of droplets as subsequently their interactions with the surrounding medium have also been some of the exciting areas of fundamental research for ages.

Of late, the movement of the soft droplet motors are found to be controlled by the electric, magnetic field, chemical reaction [41], and surface tension force [42], among others. The commonly known processes in this regard are electrowetting on dielectric [EWOD], electrohydrodynamics, magnetohydrodynamics, optoelectrowetting, light-actuated molecular conformation change, and thermal or solutal Marangoni motions [43], among others. In conventional electrowetting setup, droplets have been actuated by changing the contact angles through and externally applied electric field [44]. In comparison, the optoelectrowetting method uses light to change the impedance of a semiconductor resulting in the change of contact angle. The light-actuated molecular conformation change is based on the switch between hydrophobic and hydrophilic surfaces caused by the conformation change of the surface-immobilized molecules driven by the gradient of light intensity on substrates [45-47]. Interestingly, the ferrofluids droplets have not only shown their ability to move under remote magnetic guidance but also to actuate, split, spin, and accelerate under the influence of external magnetic field [48]. Movement of the soft and deformable droplet composed of various viscous fluids have also been studied on

the various nano-structured surfaces [49-52]. Self-motile droplets have now been employed for DNA sequencing, single-cell analysis, and advanced flow chemical reactors [53-54].

1.1.4 Driving Forces

Apart from the types of motors, the driving forces necessary for the motion of these self-propelling objects is another interesting aspect of the topics discussed in the present thesis. The response of the particles and droplets in various *in situ* and external stimuli have been one of the fascinating areas of research over the years. In particular, the advent of various fabrication and characterization techniques for the micro or nanoscale particles and droplets have made these explorations even more interesting. The micro or nanoscale particles can move under various *in situ* and external stimuli such as light, sound waves, heat effects, chemical potential gradient, electrostatic field, magnetic field, or surface tension forces, when they subdue various resistances of surrounding mediums such as the drag, friction, or the body force due to gravity [11, 14]. In this regard, the magnitude of the driving forces is such that they can move these objects only when the size and shape of the particles are expected to be below a critical limit, especially at the mesoscale.

For example, the motion of glassy carbon microsphere under electrical field is found to have its origin in the induced polarization, which may not manifest in the macroscopic carbon spheres [55]. The chemiosmotic motion of the micromotors are found to have their origin in the solute pressure imbalance across the motor surface due to the concentration gradient [56], which is again possible when the size of the motor is at the mesoscale. Further, the magnetic field induced migrations of the rod, spherical and helical shaped micromotors are possible only when the applied force on the motor is larger than the resistive forces present in the surrounding atmosphere [57-59].

1.1.5 Background Literature

Previously, many literatures have reported directional motions such as rotation, deformation, and splitting of the solid and liquid objects. Such motions are usually stimulated by diverse external or *in situ* excitations which include the electric field [60], magnetic field [61], photons [62], or chemical potential gradients [63] and useful for the applications such as targeted drug delivery [64], non-invasive penetration [65], high precision sensing [66], and biomedical devices [67]. However, most of these aforementioned self-propelling objects were non-deformable in nature. Similar to their solid counterparts, the soft and deformable liquid droplets are also found to self-propel by Marangoni effect [68], chemiosmotic force [69], electric field [70], photonic or acoustic excitations [71], and electromagnetic fields [72]. These motile droplet has shown significant potential in staging paradigm shifts in the technologies related to the biomolecule detection, drug-delivery, 3-D printing, theranostics, digital electronics [73-76] and transportation of essential bio-materials such as the vitamins, antibiotics, minerals, and anti-cancer agents [77-79].

The liquid droplets have also shown fascinating self-propulsion behaviour such as periodic deformation, rotation, and actuation on the rough-solid and soft-liquid surfaces under the influence of the externally applied electric field [80, 81]. Many review articles have summarized the scientific progresses on the self-propulsion due to the electrowetting (EW) processes involving these soft-microsystems [82, 83] useful for microscale mixing, reaction engineering, energy harvesting, droplet actuation, electronic displays, biomedical engineering, bio-MEMS devices, and droplet or digital microfluidics [84-88].

In this regard, previous studies have shown the importance of the complex shape formation involving soft materials and the subsequent management of the shape targeting various

applications [89-91]. For example, the freely falling droplets [92], the droplets bouncing on the super-repellant surfaces [93], or a solid object hitting a liquid surface [94] can also lead to fascinating shape-formation such as toroid, crown, doughnut, peanut, prolate, or oblate [95]. The different shapes of the fluidic objects and their breakup can also be used for multiphase emulsification [96], 3D-printing [97], digital microfluidics [98], and microreactors [99].

1.2 OBJECTIVES AND LAYOUT OF THE THESIS

With these brief overview on the salient features of the happenings and possibilities of bio, solid, and soft motors under various stimuli, the objectives of the present thesis have been directed to achieve precise control over motion of mesoscale particles and liquid droplets by the *in situ* and external stimuli. It may be noted here that a more detailed introduction is presented along with each chapter of the thesis to showcase the prior art related to the objectives chosen. In the Chapter 2, we present multimodal control over the chemotaxis of a catalytic motor with the application of magnetic and electric fields – namely a 'superbot'. The superbots can be used for pick and drop of payload as a cargo to the target. In the Chapter 3, we present the migration of a soft water droplet motor loaded with paramagnetic or diamagnetic salts – namely 'liquibot', capable of movement under an externally applied magnetic field. These liquibots can be employed as a drug carrier or a component of various digital microfluidic devices. In Chapter 4, we present the effect of electric field induced deformations, such as, spreading, oscillation, ejection and spinning of microdroplets. These deformations can successfully be employed in various applications, such as, in micromixing and micropump. In Chapter 5, we show a simple methodology to synthesize the micro or nanodroplets in a single step from a macroscopic one. For this purpose, we uncover the self-organized superspreading of droplets to form fluidic toroids, sheets, and threads with the

help of a simple chemical trigger and in the absence of any rotational influence. These metastable structures break to form an array of micro or nanoscale soft motors, which can be further employed for various applications related to emulsification, digital microfluidic, energy harvesting, preparation of drug delivery vehicles, among others. Finally, we summarize the thesis and outline the possibilities for future studies in Chapter 6.

REFERENCES

1. S. A. Morin, R. F. Shepherd, S. W. Kwok, A. A. Stokes, A. Nemiroski, G. M. Whitesides, *Science*, 2012, **337**, 828-832.
2. F. J. Larabee, and A. V. Suarez, *PLoS ONE*, 2015, **10**, e0124871:1-10.
3. P. P. Lele, B. G. Hosu, and H. C. Berg, *Proc. Natl. Acad. Sci.*, 2013, **110**, 11839-11844.
4. G. J. Stephens, B. J. Kerner, W. Bialek, and W. S. Ryu, *PLoS Comput. Biol.*, 2008, **4**, e1000028:1-10.
5. S. Miyashita, C. Audretsch, Z. Nagy, R. M. Füchslin, and R. Pfeifer, *J. R. Soc. Interface*, 2015, **12**, 20141271:1-8.
6. A. Shademan, R. S. Decker, J. D. Opfermann, S. Leonard, A. Krieger and P. C. W. Kim, *Sci. Transl. Med.*, 2016, **8**, 337ra64:1-8.
7. M. Rubenstein, A. Cornejo, and R. Nagpal, *Science*, 2014, **345**, 795-799.
8. L. Baraban, D. Makarov, R. Streubel, I. Mönch, D. Grimm, S. Sanchez, and O. G. Schmidt, *ACS Nano*, 2012, **6**, 3383-3389.
9. U. K. Cheang, and M. Kim, *J. Nanopart. Res.*, 2015, **17**, 1-11.
10. S. Kalepu, M. Manthina, and V. Padavala, *Acta Pharm. Sin. B*, 2013, **3**, 361-372.
11. G. Zhao, and M. Pumera, *Langmuir*, 2013, **29**, 7411-7415.
12. K. S. Khalil, S. R. Mahmoudi, N. Abu-dheir, and K. K. Varanasi, *Appl. Phys. Lett.*, 2014, **105**, 041604:1-4.
13. J. Li, B. E. F. d. Avila, W. Gao, L. Zhang, and J. Wang, *Science Robotics*, 2017, **2,** 1-9.
14. M. Guix, C. C. Mayorga-Martinez, and A. Merkoci, *Chem. Rev.*, 2014, **114**, 6285-6322.

15. J. Li, W. Gao, R. Dong, A. Pei, S. Sattayasamitsathit, and J. Wang, *Nat. Commun*., 2014, **5**, 1-7.
16. R. Dong, J. Li, I. Rozen, B. Ezhilan, T. Xu, C. Christianson, W. Gao, D. Saintillan, B. Ren and J. Wang, *Sci. Rep.*, 2015, **5,** 1-7.
17. O. J. N. Bertranda, D. K. Fygensonb, and O. A. Saleh, *Proc. Natl. Acad. Sci.*, 2012, **109**, 17342-17347.
18. S. Bonhoeffer, R. M. May, G. M. Shaw, and M. A. Nowak, *Proc. Natl. Acad. Sci.*, 1997, **94**, 6971-6976.
19. O. E. Shklyaev, H. Shum, A. Sen, and A. C. Balazs, *Science*, 2016, **2**, 1-13.
20. J. J. Li, and W. Tan, *Nano Lett.*, 2002, **2**, 315-318.
21. S. Sengupta, M. M. Spiering, K. K. Dey, W. Duan, D. Patra, P. J. Butler, R. D. Astumian, S. J. Benkovic, and A. Sen, *ACS Nano*, 2014, **8**, 2410-2418.
22. J. Simmchen, A. Baeza, D. Ruiz-Molina, M. Vallet-Regí, *Nanoscale*, 2014, **6**, 8907-8913.
23. S. Sengupta, K. K. Dey, H. S. Muddana, T. Tabouillot, M. E. Ibele, P. J. Butler and A. Sen, *J. Am. Chem. Soc.*, 2013, **135**, 1406-1414.
24. R. Ballardini, V. Balzani, A. Credi, M. T. Gandolfi and M. Venturi, *Acc. Chem. Res.*, 2001, **34**, 445-455.
25. http://www.nobelprize.org/nobel_prizes/chemistry/laureates/2016/press.html
26. G. J. Simpson, V. G. Lopez, P. Petermeier, L. Grill, and J. M. Tour, *Nat. Nanotechnol.*, 2017, **12**, 604-606.
27. A. K. Geim, *Science*, 2009, **324**, 1530-1534.
28. V. Georgakilas, M. Otyepka, A. B. Bourlinos, V. Chandra, N. Kim, K. C. Kemp, P. Hobza, R. Zboril, and K. S. Kim, *Chem. Rev.*, 2012, **112**, 6156-6214.
29. W. Gao, M. D. Agostino, V. Garcia-Gradilla, J. Orozco, and J. Wang, *Small*, 2013, **9**, 467-471.
30. T. C. Lee, M. Alarcon-Correa, C. Miksch, K. Hahn, J. G. Gibbs, and P. Fischer, *Nano Lett.*, 2014, **14**, 2407-2412.
31. A. K. Singh, K. K. Dey, A. Chattopadhyay, T. K. Mandal, and D. Bandyopadhyay, *Nanoscale*, 2014, **6**, 1398-1405.
32. K. Yao, M. Manjare, C. A. Barrett, B. Yang, T. T. Salguero, and Y. Zhao, *J. Phys. Chem. Lett.*, 2012, **3**, 2204-2208.

33. X. Chen, G. Wu, T. Lan, and W. Chen, *Chem. Commun.*, 2014, **50**, 7157-7159.
34. M. Guix, C. C. M. Martinez, and A. Merkoci, *Chem. Rev.*, 2014, **114**, 6285-6322.
35. F. Peng, Y. Tua, and D. A. Wilson, *Chem. Soc. Rev.*, 2017, **46**, 5289-5310.
36. W. Gao and J. Wang, *ACS Nano*, 2014, **8**, 3170-3180.
37. S. Y. Park, M. A. Teitell, and E. P. Y. Chiou, *Lab Chip*, 2010, **10**, 1655-1661.
38. E. Pairam, and A. Fernandez-Nieves, *Phys. Rev. Lett.*, 2009, **102**, 234501:1-4.
39. T. Cubaud, *Phys. Rev. E*, 2009, **80**, 026307:1-4.
40. V. Chokkalingam, Y. Ma, J. Thiele, W. Schalk, J. Tel, and W. T. S. Huck, *Lab Chip*, 2014, **14**, 2398-2402.
41. J. Zhang, Y. Yao, L. Sheng and J. Liu, *Adv. Mater.*, 2015, **27**, 2648-2655.
42. G. Katsikis, J. S. Cybulski, and M. Prakash, *Nature Phys.*, 2015, **11**, 588-596.
43. S. Arscott, *Sci. Rep.*, 2011, **1**, 184:1-7.
44. M. G. Lippmann, *Ann. Chim. Phys*, 1875, **5**, 494-549.
45. N. Wangner, and P. Theato, *Polymer*, 2014, **55**, 3436-3453.
46. H. S. Lim, D. Kwak, D. Y. Lee, S. G. Lee, and K. Cho, *J. Am. Chem. Soc.*, 2007, **129**, 4128- 4129.
47. R. Wang, K. Hashimoto, A. Fujishima, M Chikuni, E. Kojima, A. Kitamura, M. Shimohigoshi, and T. Watanabe, *Nature*, **388**, 431-432.
48. J. V. I. Timonen, M. Latikka, L. Leibler, R. H. A. Ras, and O. Ikkala, *Science*, 2013, **343**, 253-257.
49. R. Abdelaziz, D. Disci-Zayed, M. K. Hedayati, J. H. Pohls, A. U. Zillohu, B. Erkartal, V. S. K. Chakravadhanula, V. Duppel, L. Kienle, and M. Elbahri, *Nat. Commun.*, 2013, **4**, 2400:1-10.
50. N. J. Cira, A. Benusiglio and M. Prakash, *Nature*, 2015, **519**, 446–450.
51. E. Brouzes , T. Kruse, R. Kimmerling, and H. H. Strey, *Lab Chip*, 2015, **15**, 908-919.
52. P. Galliker, J. Schneider, H. Eghlidi, S. Kress, V. Sandoghdar, and D. Poulikakos, *Nat. Commun.*, 2012, **3**, 890:1-9.
53. P. Dubois, G. Marchand, Y. Fouillet, J. Berthier, T. Douki, F. Hassine, S. Gmouh, and M. Vaultier, *Anal. Chem.*, 2006, **78**, 4909-4917.
54. S. Y. Teh, R. Lin, L. H. Hung, and A. P. Lee, *Lab Chip*, 2008, **8**, 198-220.
55. G. Loget, and A. Kuhn, *Nat. Commun.*, 2011, **2**, 535:1-6.

56. K. K. Dey, S. Bhandari, D. Bandyopadhyay, S. Basu, and A. Chattopadhyay, *Small*, 2013, **9**, 1916-1920.
57. W. Gao, S. Sattayasamitsathit, K. M. Manesh, D. Weihs, and J. Wang, *J. Am. Chem. Soc.*, 2010, **132**, 14403-14405.
58. K. I. Morozov, and A. M. Leshansky, *Nanoscale*, 2014, **6**, 1580-1588.
59. P. Mandal, V. Chopra, and A. Ghosh, *ACS Nano*, 2015, **9**, 4717-4725.
60. G. Loget and A. Kuhn, *Nat. commun.*, **2**:535, 1-6.
61. F. Peng, Y. Tu, Y. Men, J. C. M. van Hest, and D. A. Wilson, *Adv. Mater.*, 2017, **29**, 1604996:1- 7.
62. B. Dai, J. Wang, Z. Xiong, X. Zhan, W. Dai, C. C. Li, S. P. Feng and J. Tang, *Nat. Nanotechnol.* 2016, **11**, 1087-1092.
63. F. Peng, Y. Tu, J. C. M. van Hest, D. A. Wilson, *Angew. Chem. Int. Ed.*, 2015, **54**,11662- 11665.
64. W. Gao, D. Kagan, O. S. Pak, C. Clawson, S. Campuzano, E. Chuluun-Erdene, E. Shipton, E. E. Fullerton, L. Zhang, E. Lauga, and J. Wang, *Small*, 2012, **8,** 460-467.
65. W. Xi, A. Solovev, AN. Ananth, D. Gracias, S. Sanchez, and OG. Schmidt, *Nanoscale*, 2013, **5**, 1294-1297.
66. S. Campuzano, D. Kagan, J. Orozco, and J. Wang, *Analyst*, 2011, **136**, 4621-4630.
67. L. K. E. A. Abdelmohsen, F. Peng, Y. Tu, and D. A. Wilson, *J. Mater. Chem. B*, 2014, **2**, 2395-2408.
68. M. Manjare, F. Yang, R. Qiao and Y. Zhao, *J. Phys. Chem. C*, 2015, **119**, 28361-28367.
69. J. Cejkova, M. Novák, F. Stepanek, and M. M. Hanczyc, *Langmuir*, 2014, **30**, 11937-11944.
70. N. Miljkovic, D. J. Preston, R. Enright, and E. N. Wang, *Nat. Commun.*, 2013, **4**, 1-9.
71. A. Diguet, R.-M. Guillermic, N. Magome, A. Saint-Jalmes, Y. Chen, K. Yoshikawa and D. Baigl, *Angew. Chem. Inter. Ed.*, 2009, **48**, 9281-9284.
72. R. S. M. Rikken, R. J. M. Nolte, J. C. Maan, J. C. M. van Hest, D. A. Wilson, and P. C. M. Christianen, *Soft Matter*, 2014, **10**, 1295-1308.
73. K. Pataky, T. Braschler, A. Negro, P. Renaud, M. P. Lutolf and J. Brugger, *Adv. Mater.*, 2012, **24**, 391-396.

74. S. Juul, C. J. F. Nielsen, R. Labouriau, A. Roy, C. Tesauro, P. W. Jensen, C. Harmsen, E. L. Kristoffersen, Y.-L. Chiu, R. Frøhlich, P. Fiorani, J. Cox-Singh, D. Tordrup, J. Koch, A.-L. Bienvenu, A. Desideri, S. Picot, E. Petersen, K. W. Leong, Y.-P. Ho, M. Stougaard and B. R. Knudsen, *ACS Nano*, 2012, **6**, 10676-10683.
75. L. Florea, K. Wagner, P. Wagner, G. G. Wallace, F. Benito-Lopez, D. L. Officer and D. Diamond, *Adv. Mater.*, 2014, **26**, 7339-7345.
76. K. K. Dey, X. Zhao, B. M. Tansi, W. J. Méndez-Ortiz, U. M. Cordova-Figueroa, R. Golestanian and A. Sen, *Nano Letters*, 2015, **15**, 8311-8315.
77. M. Kiristi, V. V. Singh, B. Esteban-Fernández de Ávila, M. Uygun, F. Soto, D. A. Uygun and J. Wang, *ACS Nano*, 2015, **9**, 9252-9259.
78. S. Sengupta, D. Patra, I. Ortiz-Rivera, A. Agrawal, S. Shklyaev, K. K. Dey, U. Córdova-Figueroa, T. E. Mallouk and A. Sen, *Nat. Chem.*, 2014, **6**, 415-422.
79. M.G. Lippmann, *Ann. Chim. Phys*, 1875, **5,** 494-549.
80. G. Taylor, *Proc. R. Soc. Lond. A Math. Phys. Sci.*, 1964, **280**, 383-397.
81. F. Mugele, and J. C. Baret, *J. Phys. Condens. Matter*, 2005, **17**, 705-774.
82. H. H. Girault, *Nat. Mater.*, 2006, **5**, 851-852.
83. F. Mugele, A. Staicu, R. Bakker, and D. van den Ende, *Lab Chip*, 2011, **11**, 2011-2016.
84. N. Miljkovic, D. J. Preston, R. Enright, and E. N. Wang, *Appl. Phys. Lett.*, 2014, **105**, 013111:1-5.
85. K. L. Wang, and T. B. Jones, *Langmuir* 2005, **21**, 4211-4217.
86. H. H. Shen, S. K. Fan, C. J. Kim, and D. J. Yao, *Microfluid. Nanofluid.*, 2014, **16**, 965-987.
87. D. Chatterjee, B. Hetayothin, A. R. Wheeler, D. J. King and R. L. Garrell, *Lab Chip*, 2006, **6**, 199-206.
88. S. K. Cho, H. J. Moon, and C. J. Kim, *J. Microelectromech. Syst.*, 2003, **12**, 70-80.
89. L. V. Zhang, J. Toole, K. Fezzaa, and R. D. Deegan, *J. Fluid Mech.*, 2012, **690**, 5-15.
90. D. T. Papageorgiou, *Phys. Fluids*, 1995, **7**, 1529-1544.
91. S. Yun and G. Lim, *J. Fluid Mech.*, 2014, **752**, 266-281.
92. M. K. Tripathi, K. C. Sahu, and R. Govindarajan, *Sci. Rep.*, 2014, **4**, 4771:1-9.

93. R. Clift, J. R. Grace and M. E. Weber, Bubbles, Drops and Particles (Academic, New York, 1978).

94. Y. C. Jung, and B. Bhushan, *Langmuir*, 2008, **24**, 6262-6269.

95. E. M. Terentjev, *Nat. Mater.*, 2002, **1**, 149-150.

96. J. M. P. Gutierrez, T. Hinkley, J. W. Taylor, K. Yanev, and L.Cronin, *Nat. Commoun.*, 2014, **5**, 1-8.

97. J. R. Tumbleston, D. Shirvanyants, N. Ermoshkin, R. Janusziewicz, A. R. Johnson, D. Kelly, K. Chen, R. Pinschmidt, J. P. Rolland, A. Ermoshkin, E. T. Samulski, and J. M. DeSimone, *Science*, 2015, **347**, 1349-1352.

98. L. Mazutis, J. Gilbert, W. L. Ung, D. A. Weitz, A. D. Griffiths, and J. A. Heyman, *Nat. Protocols*, 2013, **8**, 870-891.

99. P. Dubois, G. Marchand, Y. Fouillet, J. Berthier, T. Douki, F. Hassine, S. Gmouh, and M. Vaultier, *Anal. Chem.*, 2006, **78**, 4909-4917.

Chapter 2

Multifunctional Graphene Superbots for Chemo-Magneto-Galvanotaxis

2.1 INTRODUCTION

Directed migrations of the microorganisms are stimulated by diverse external or *in situ* excitations which include the electric field - galvanotaxis, magnetic field - magnetotaxis, light - phototaxis, or chemical potential gradient - chemotaxis. Emulating these events, miniaturized self-propelling artificial objects can be synthesized for the applications such as targeted drug delivery [1-3], non-invasive penetration [4, 5], high precision sensing [6, 7] and biomedical devices [8]. In particular, the chemically empowered nano-locomotives [9-17] are envisioned to perform complex *in vivo* or *ex vivo* tasks with functional efficacy similar to their biological counterparts. The recent advancements on the fabrication of self-propelling objects are directed towards this end where the nanoscale objects have shown motions under various internal and external triggers such as the gradients of magnetic field [18-20], electric field [21], temperature [22], surface tension [23-24], and electromagnetic [25] or acoustic [26] potential. The existing challenges are to infuse biocompatibility, attain multimodal *in situ* and remote control on the motion, tune the directionality at a faster response time, and add functionalities specific to the engineering processes.

Interestingly, the present decade has also experienced another important paradigm-shift in which the metal based applications have been transformed into the biocompatible carbon based processes [27]. In this direction, the artificial locomotives have also been benefitted by the specialties of the carbon nanotubes, carbon nanofibres, fullerene, and graphene surfaces which includes the higher electrical and thermal conductivities [28, 29], ease of functionalization [30], availability of the larger surface to volume ratio [31] and biocompatibility [32]. A few recent studies indicated that the inclusion of carbon nanotubes (CNT/Au/Pt), reduced graphene oxide (RGO/MnO_x), and graphene oxide (GO/Ti/Pt) along with metal or metal oxides or metal alloys could significantly improve

the catalytic and transport properties of the motors [33-36]. However, most of these studies focused on a single stimulus for the migration and barring a few studies, the motions demonstrated to be rather random and uncontrolled.

Herein, we report the fabrication of a reduced graphene oxide (RGO) based microbot, which was capable of showing all three types of directed migrations – chemotaxis in alkaline peroxide fuel, electrophoresis in alkaline fluid medium, and the external magnetic field induced motion. The RGO motor (size ~ 80 μm) was composed of a glass microbead coated with thin graphene sheets. The motor harnessed the chemical energy for migration through catalytic surface decomposition of the peroxide fuel. The difference in peroxide concentration across the motor due to the imposed pH gradient created a difference in solute concentration across the motor, which resulted in a solute pressure imbalance to drive the motor from the region of lower pH to the higher one. The negative ζ-potential of the graphene coated motor in alkaline medium helped in a directed electrophoretic migration under the externally applied electric field. The velocities obtained for the electrophoretic migration was found to be comparable with the theoretical values obtained from the Smoluchowski equation. Further, the sparsely distributed ferromagnetic iron nanoparticles (FeNPs) on the surface infused the magnetic sensitivity to the motor. The multimodal electric, chemical, and magnetic control on the migration of the RGO motor helped in the approach, capture, transport, and delivery of payloads inside the microfluidic environments. The motor could be remotely controlled for transporting cargoes of nearly 1000 times heavier and ~13 times larger than the size of the motor. Remarkably, the RGO motor could subdue a drag force of ~ 2619 pN while undergoing an *in situ* migration. The results reported can contribute to the development of the next generation superbots [37, 38] helpful for the applications related to the pharmaceutical devices [39-41], *in situ*

catalysis [42], environmental remediation [43, 44], payload transport [45-49], sensing [50, 51], diagnostics [52, 53] and micro-devices [54].

2.2. EXPERIMENTAL SECTION

2.2.1. Materials

Hydrochloric acid (HCl), 50% hydrogen peroxide (H_2O_2), sodium hydroxide (NaOH) pellets, sodium chloride (NaCl), potassium permanganate ($KMnO_4$), 98% sulfuric acid (H_2SO_4), 125 mm filter paper (grade 1), acetone (CH_3COCH_3), and 84% ortho-phosphoric acid (H_3PO_4) were obtained from Merck (India). Poly-(methyl methacrylate) (PMMA), Phenolphthalein, iron (III) chloride hexahydrate ($FeCl_3.6H_2O$), sodium borohydride ($NaBH_4$), phosphorous pentoxide (P_2O_5), 98% hydrazine monohydrate (N_2H_4), glass beads were obtained from Sigma-Aldrich (India). Graphite flakes (99.99%) and anhydrous barium chloride ($BaCl_2$) were obtained Alfa Aesar and Fisher Scientific, respectively. Platinum (Pt) wires of length 2.5 cm and diameter 150 µm were procured from Surgeon Sons, India. For microchannel fabrication poly-dimethylsiloxane (PDMS) was purchased from Dow Corning, India (SYLGARD® 184 kit). The chemicals mentioned above were of analytical grade and used for the experiments without further purification. The Milli-Q grade water was used for cleaning and to prepare the solutions.

2.2.2. Graphene Oxide (GO) synthesis method

GO solution was prepared from graphite flakes following the improved synthesis method [55]. The graphite flakes (0.5 g) and $KMnO_4$ (3.0 g) were added in a mixture of 63 mL of concentrated H_2SO_4 and 7 mL of H_3PO_4. The resulting solution was heated at 50 $^{\circ}$C and stirred for 12 h. Following this, 30% H_2O_2 (3 mL) and 50 mL of water was added into the solution. The exothermic reaction was carried out in an ice cooled environment (0 $^{\circ}$C) and

after completion 100 mL of water was added into the solution. The solution was then cooled down to room temperature and centrifuged (8000 rpm for 15 min) to discard the supernatant liquid. The precipitate was washed 3 to 4 times periodically with 10% HCl and water, until sulfate was not detected by addition of $BaCl_2$. The precipitate was washed repeatedly with water until a neutral pH was reached. The precipitate was then dried with P_2O_5 in vacuum at room temperature before dispersing in water and sonication for 2 h to obtain the GO solution for the experiments.

2.2.3. Fabrication of reduced graphene oxide coated (RGO) motors

Glass beads (1 g) were washed 2-3 times in 10% HCl and water and then dried at 65 °C. The dried glass beads were then suspended in the 3 mL of GO solution (1 mg/mL) and heated at 80 °C. This procedure was repeated thrice. Then, by using hydrazine vapors, GO coated glass beads were reduced at 120°C for 3 h and washed with water [56, 57]. Finally, the RGO motors were dried at 65°C.

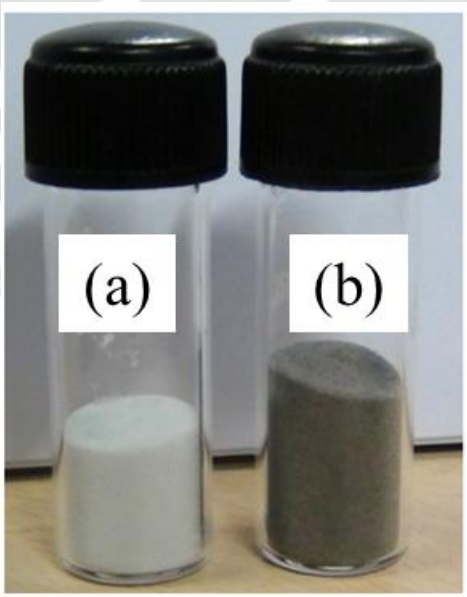

Figure 2.1. (a) Uncoated glass beads and (b) reduced graphene oxide (RGO) coated glass beads.

The uncoated glass beads were white in colour as shown in Figure 2.1 (a) However, after the deposition of the reduced graphene oxide (RGO), the coated glass beads turned black in colour, as shown in Figure 2.1 (b). The average diameter of the freshly prepared spherical motors were of ~80 µm.

2.2.4. Fabrication of magnetic RGO (FeNP@RGO) motors

Glass beads (1 g) were rinsed with 10% HCl and water, respectively, and dried at 65°C. The washed glass beads were suspended in 20 mL of 1M $FeCl_3 \cdot 6H_2O$ solution for 4 h. Then the $FeCl_3 \cdot 6H_2O$ solution was decanted off and the glass beads were dried at 110°C [58]. Following this, the dry glass beads were suspended in 30 mL of water and the $NaBH_4$ solution (20 mg/mL) was added drop-wise [59]. The suspension was then heated at 80°C for 45 min. The FeNP-coated glass beads were washed 2-3 times with water before dipping into the GO solution. After 1 h, the beads were removed from GO solution and dried at 80°C. This procedure was repeated 3 times. The GO coated glass beads were reduced by hydrazine vapors at 120°C for 3 hours. The FeNP@RGO motors were washed 2-3 times with water and dried at 65°C before using for the experiments.

2.2.5. PDMS microchannel fabrication

The PDMS and curing agent were mixed for 30 min in 1:10 ratio, avoiding the air bubble formation while mixing. Following this, the mixture was poured inside a mold having the shape of the microchannel [60]. Following this, it was put in an air oven at 60 °C for 40 min. The cast was removed carefully from the mold with the help of acetone.

2.2.6. Velocity measurements under the influence of pH gradient

A RGO motor (size ~80 µm) was placed in 7 mL of 9% (v/v) aqueous H_2O_2 inside a petridish (3 cm diameter). The 0.3 M NaOH solution was introduced at the center of the

petridish through a cotton thread connected to a reservoir. The petridish was placed over a paper having a scale bar of 0.5 mm to measure the displacement of the motor. The pattern of NaOH diffusion in H_2O_2 bath was observed by adding phenolphthalein indicator in the H_2O_2 solution. The velocity of the motor was studied at different pH values of the alkaline solution. The velocity of the motor was measured at a position away (~4 mm) from the thread in order to minimize the influence of the thread on the motor movement [12, 15]. The experiments were repeated thrice for every pH value and the average velocity (V_C) was reported.

2.2.7. Velocity measurements under the influence of magnetic field

The PDMS microchannel was placed in between the poles of an electromagnet. A FeNP@RGO motor (size ~80 µm) was placed in a microchannel filled with aqueous H_2O solution. The petridish was placed on a paper decorated with a 0.5 mm scale bar on it, which helped in measuring the displacement of the motor. The velocity of the FeNP@RGO motor was tuned by varying the magnetic field strength across the microchannel with the help of an electromagnet and the variation in the magnetic field was measured by Gaussmeter [15]. The experiments were repeated thrice for each pH value and the average velocity (V_M) was reported.

2.2.8. Velocity measurements under the influence of electric field

The microchannel was filled with pH 10.1 NaOH solution. A RGO motor (size ~80 µm) was introduced in the solution inside the microchannel between a pair of Pt electrodes, which were 10 mm apart. The microchannel was placed on a paper having a 0.5 mm scale bar to measure the displacement of the motor. The velocity of the RGO was observed by varying the voltage across electrodes with the help of a DC (direct current) power supply

unit. The experiments were repeated thrice for each pH value and the average velocity (V_E) was reported.

2.2.9. Pickup, transport, and delivery of cargoes

A FeNP@RGO motor (size ~80μm) was suspended in a 9% (v/v) aqueous H_2O_2 filled inside the microchannel. The movement of the motor was remotely controlled with the help of an external permanent magnet. For pick-up, drag, and drop of the cargoes, the FeNP@RGO motor was immersed in the petridish filled with H_2O_2. The motor was guided towards and away from the cargo by an external magnet. The velocity of the motor during cargo delivery was measured from the recorded video. Further, in order to introduce chemotactic migration coupled with the magnetic field driven motion, the pH gradient was introduced in the chamber by dripping 0.3 M NaOH solution at the center of the petridish through a cotton thread connected to a reservoir.

2.2.10. Rate constant measurement for H_2O_2 decomposition

The rate of decomposition of H_2O_2 solution on the surface of RGO motor was analyzed by the volumetric analysis with $KMnO_4$ [12, 15]. The strength of the $KMnO_4$ was standardized by 0.2 N oxalic acid. Firstly, a 5 mL of 9% (v/v) H_2O_2 was pH adjusted by adding 0.3 M NaOH solution. Then, the RGO motors (0.3 g) were immersed in the peroxide solution. A series of such solutions were prepared to estimate the depletion rate of H_2O_2 at various time intervals. For a given time-interval, a 300 μL aliquot was withdrawn and added to 10 mL 0.2 N H_2SO_4 solution. Following this, the sample was titrated against standard 0.2 N $KMnO_4$ solutions in which a permanent pink coloration indicated the end point. The rate constant (k) for the H_2O_2 decomposition was estimated from the change in H_2O_2 concentration with time. The straight line of the plot confirmed

that H_2O_2 decomposition followed first-order kinetics. This process was repeated for all the pH values in the presence of the catalytic (RGO coated beads) and non-catalytic beads (uncoated beads). The catalytic rate constant (k_{cat}) was measured alongside the non-catalytic rate constant ($k_{non\text{-}cat}$) for the H_2O_2 decomposition in the presence of the same amount of beads. The net rate constant (k_{net}) was calculated from the difference between k_{cat} and $k_{non\text{-}cat}$. The effective rate constant (k_{eff}) of a single RGO motor was estimated by dividing k_{net} with the number of microbeads employed for the peroxide decomposition.

2.2.11. Characterization

Field emission scanning electron microscopy (FESEM, Sigma, Zeiss, Germany) and scanning electron microscopy (SEM, LEO, 1430vp, US) were used to examine the surface morphology of the motors. The magnetization curve was determined by vibrating sample magnetometer (VSM, Lakeshore GMW magnetic systems 3474-140). The pH of the solutions was measured by pH meter (CyberScan pH 510, Eutech Instruments). The ζ-potential was measured by Malvern, Zeta-Size-Analyser, NanoZS. The motion of the motor was recorded with a Sony Cybershot DSC-HX100V digital camera (Sony Corp., Japan). The diameter of motors was measured under Leica DM 2500 upright microscope. The electromagnet Model EMU-50V with a constant current power supply unit (DPS – 50) was used to apply the magnetic field in the experiments and the applied magnetic field was measured by Digital Gaussmeter (Model DGM-102, SES instruments, India). The regulated DC power supply unit (Model 1252, Aplab, India) was used for the electric field experiments. The Raman characterization was done by micro-Raman spectrometer (Jovin Horiba, LabRam HR800) at 532 nm laser excitations.

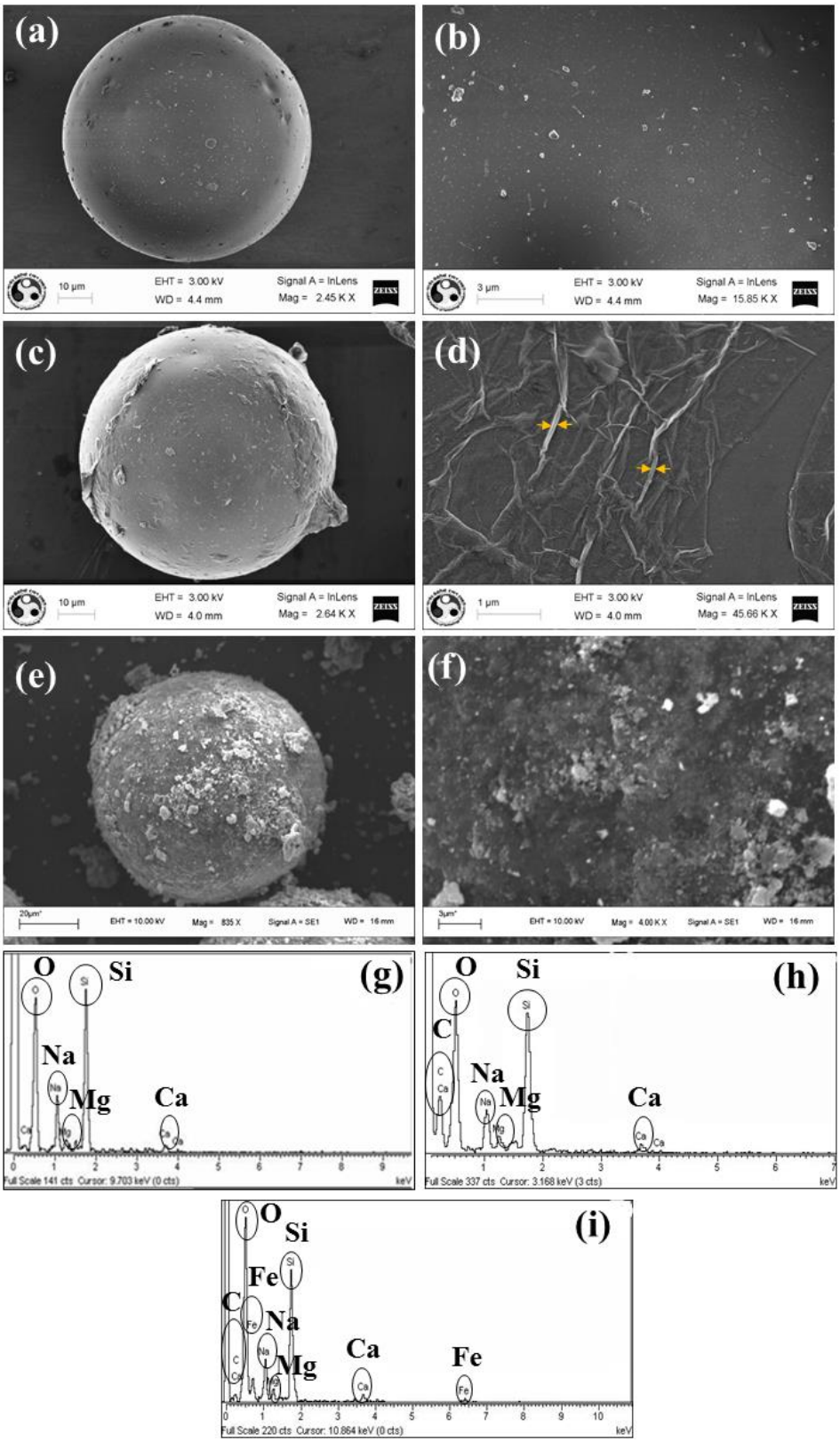

Figure 2.2. (a) FESEM image of an uncoated glass bead. The scale bar at the bottom is of 10 µm, (b) Magnified FESEM image of the uncoated glass bead surface. The scale bar at

the bottom is of 3 µm, (c) Magnified FESEM image of a reduced graphene oxide (RGO) coated glass beads. The scale bar at the bottom is of 10 µm, (d) FESEM image of a RGO glass bead surface. The yellow arrows show the thickness of the wrinkled RGO sheets. The scale bar at the bottom is of 1 µm, (e) SEM image of freshly prepared iron nanoparticle (FeNP) impregnated RGO glass beads. The scale bar at the bottom is of 20 µm, (f) SEM image of surface of iron nanoparticle (FeNP) impregnated RGO glass beads. The scale bar at the bottom is of 3 µm, (g) Spot EDX of uncoated glass beads. (h) Spot EDX of RGO coated glass beads, (i) Spot EDX of iron nanoparticle (FeNP) deposited on the RGO (FeNP@RGO) coated glass beads, which shows the elemental Fe peak.

The uncoated glass beads and the freshly prepared RGO micromotors were characterized using the FESEM and SEM. Figure 2.2 (a**)** and (b) shows the surface of uncoated glass beads. The spot EDX of uncoated beads (Figure 2.2 (g)) shows the presence of elemental Sodium (Na), Silicon (Si), Calcium (Ca) and Magnesium (Mg) as the constituents of uncoated glass bead. Figure 2.2 (d**)** shows the wrinkles of multi-layered RGO on the glass bead. The typical lateral widths of the multilayer RGO wrinkles estimated to be ~ 66 nm, as shown by the arrows. The presence of the elemental carbon (C) and oxygen (O) peaks of the spot EDX spectra on these RGO sheets confirmed the presence of the RGO multilayers (Figure 2.2 (h)). The SEM image of a single FeNP@RGO motor surface showed the agglomerates of FeNPs of varying size (Figure 2.2 (f)). The spot EDX on the agglomerates confirmed the presence of the FeNP clusters (Figure 2.2 (i))**.** The glass bead contributed for the elemental Ca, Na, Si, and Mg peaks in the Figure 2.2 (h) and (i).

Figure 2.3 (a) shows the 2D and G band peaks at 2734 cm^{-1} and 1582 cm^{-1} Raman shift for graphite [61, 62]. Figure 2.3 (a) also shows the appearance of the 2D band at 2734 cm^{-1} for bulk graphite. This peak originated from the stacking of graphitic sp^2 materials [63]. In

case of graphene oxide (GO), the D and G bands peaks appeared at 1349 cm^{-1} and 1594 cm^{-1}, respectively, as shown in Figure 2.3 (b**)** [61, 62].

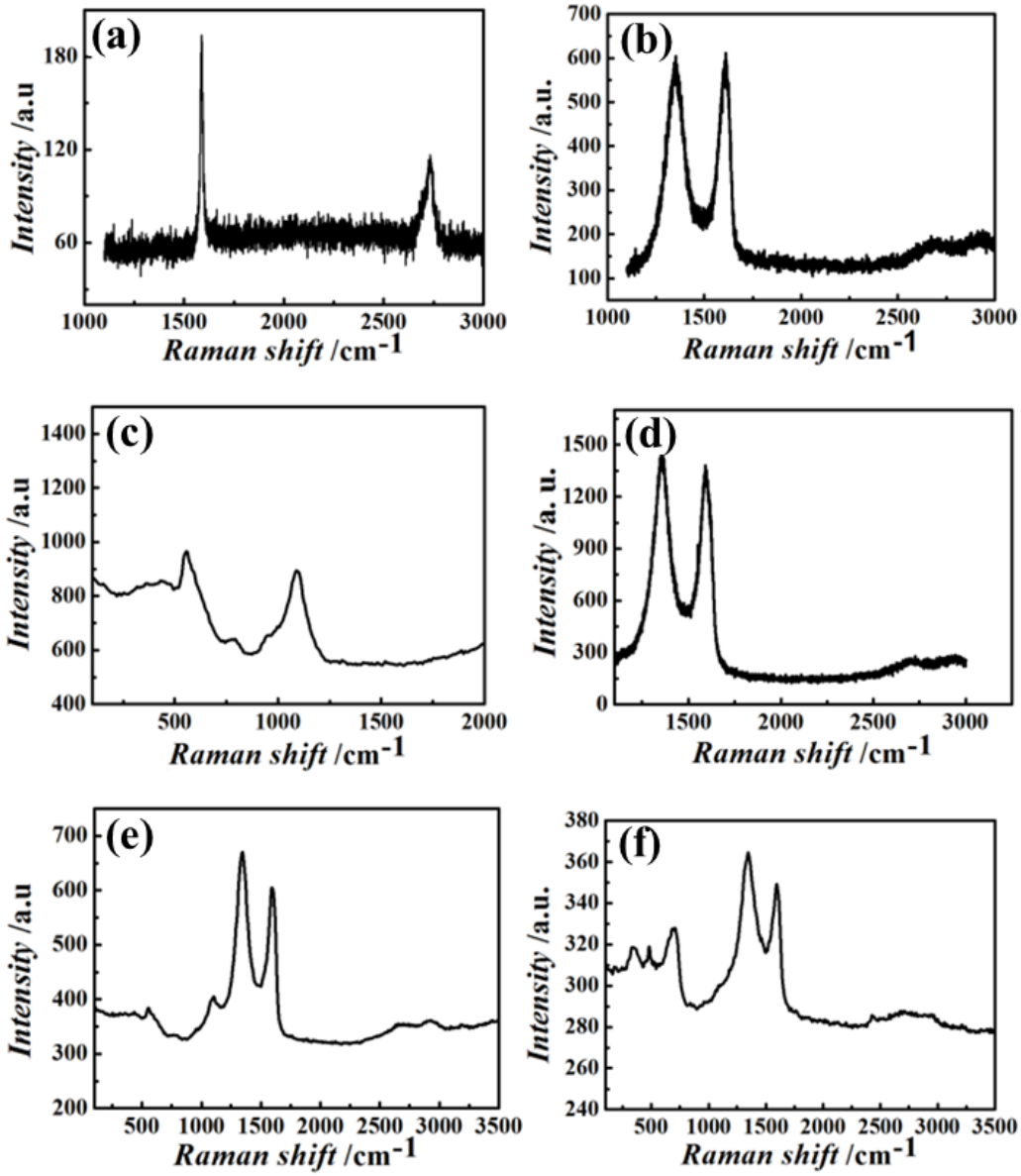

Figure 2.3. Raman spectra at 514 nm laser excitation for (a) graphite, (b) graphene oxide, (c) uncoated glass beads, (d) RGO flakes, (e) RGO motors, and (f) FeNP@RGO motors.

Figure 2.3 (c) shows the Raman spectra of the glass beads in the 10 - 1500 cm^{-1} range [64, 65]. In the case of RGO (Figure 2.3 (d)), the G band appeared at 1584 cm^{-1}, which indicated the hexagonal network recovery of defects in carbon atoms. The D band peak of

RGO was higher compared to the G band peak [61]. The formation of GO and RGO layers resulted in decrement of the symmetrical and sharp 2D-band Raman peak. According to the literature [66], it had been observed that with increase in the number of graphene layers, the amplitude of 2D-band peak decreases and the width broadens. The oxidation of graphite into GO/RGO disordered the stacking of graphitic sp^2 resulting in broadening of 2D peak within range of 2695-2927 cm^{-1}, as was observed in Figure 2.3 (b**)** and (d). Further, the hydrazine-mediated reduction of GO into RGO also led to noise and additional broadening of peaks due to presence of nitrogen impurities [1]. Figure 2.3 (e) shows the Raman spectra of the RGO motors in which the 250 - 1300 cm^{-1} peak range confirmed the presence of the glass and 1342/1584 cm^{-1} peaks for D and G bands indicated the presence of the RGO. The Raman spectra for magnetic FeNP@RGO motors (Figure 2.3 (f)) showed the peaks for RGO, the D, G, and 2D + G band peaks were observed at 1341 cm^{-1}, 1584 cm^{-1}, and 2695-2927 cm^{-1}, respectively [67]. The peak around 700 cm^{-1} accounted for partial surface oxidation of FeNPs due to air exposure. The FeNPs did not exhibit any dominant peak in Figure 2.3 (f).

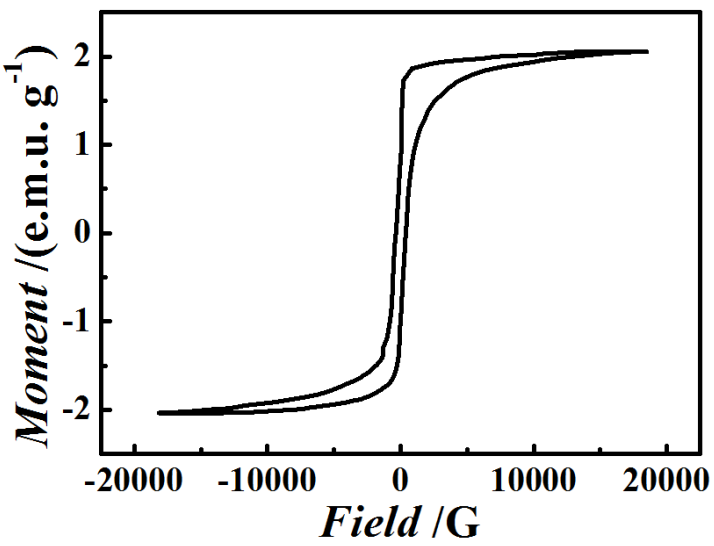

Figure 2.4. Vibrating sample magnetometry (VSM) hysteresis loop for RGO motors.

The magnetization curve of FeNP@RGO micromotor was obtained from the VSM at room temperature by varying the magnetic field from −20 to 20 kOe as shown in Plot 2.4. The S-shaped magnetization hysteresis curve suggests that the magnetic motors were ferromagnetic in nature.

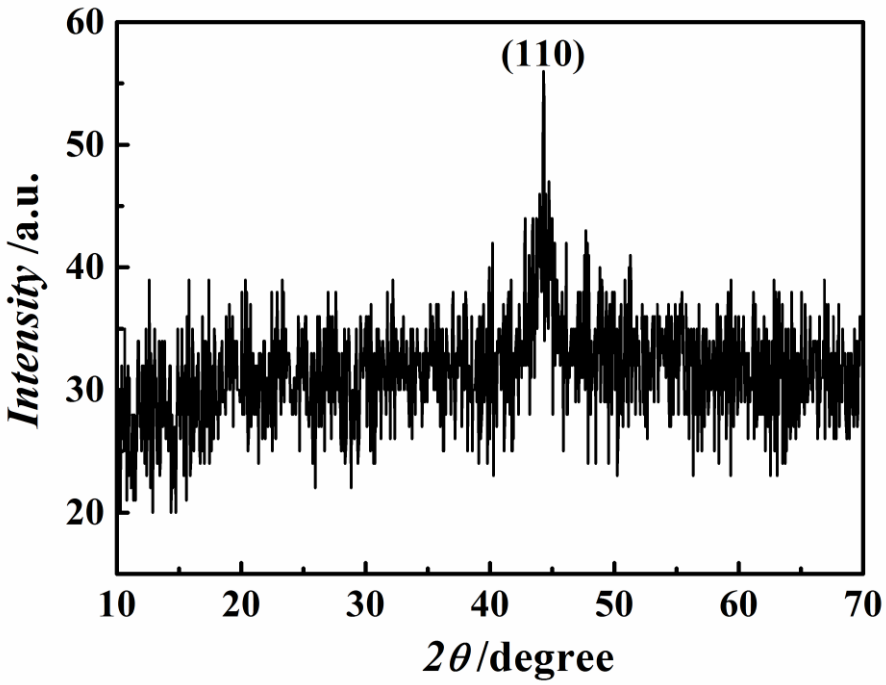

Figure 2.5. X-Ray diffraction of iron nanoparticle (FeNP) impregnated RGO (FeNP@RGO) micromotor.

The XRD of the iron nanoparticle (FeNP) impregnated RGO (FeNP@RGO) micromotor showed in Plot 2.5 a broad peak at 2θ = 44.5. The value was close to the body centred cubic α-Fe for principal plane (110) at 2θ = 44.671 (JCPDS 06-0696) [67]. The multi-layered coating of RGO on the glass beads masked the characteristic diffusive peak of amorphous silica dioxide (SiO_2) and thus no peak was observed for glass beads.

2.3. RESULT AND DISCUSSION

Figure 2.6 (a) schematically shows the synthesis of the RGO motor (dia. ~80 µm) where RGO layers were coated on the spherical glass beads. Images 2.6 (b)-(d) represent the

directional motion of the micromotor under the influence of electric field, pH taxis and magnetic field.

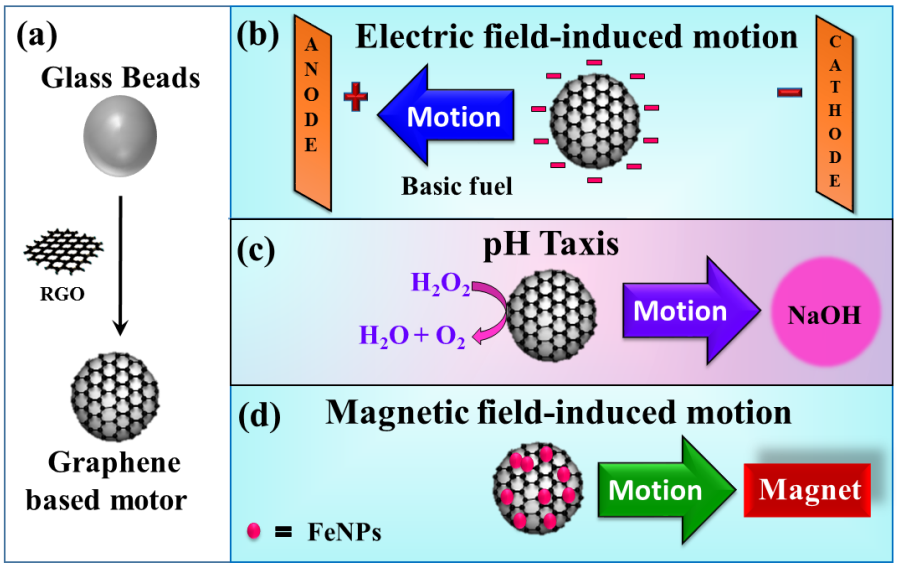

Figure 2.6. (a) Preparation of reduced graphene oxide-coated (RGO) motor. The RGO layers were coated over spherical glass beads, (b) Electrophoresis of a RGO motor in the alkaline medium. The negative ζ-potential on the motor surface helped the migration towards the anode in alkaline medium when subjected to an electric field, (c) Chemotaxis of RGO motor in alkaline peroxide bath, (d) Magnetic field induced motion of RGO motor.

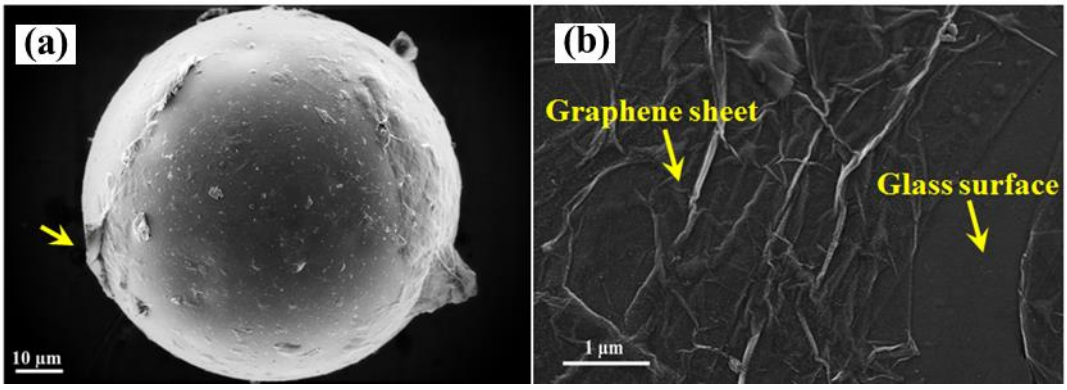

Figure 2.7. (a) Field emission scanning electron microscopy (FESEM) image of a ~ 80 µm spherical RGO motor. The length of the scale bar at the bottom is 10 µm, (b) Magnified FESEM image of the surface of RGO motor. The image shows the folds of the RGO layers on the glass bead. The scale bar at the bottom is of 1 µm.

Presence of multilayer RGO sheets on the motor helped in retaining the catalytic activity inside peroxide fuel for a longer timespan [68]. The FESEM images in the Figure 2.7 clearly show that the glass bead was coated with multi-layered RGO sheets (Figure 2.7(a)). The wrinkled sheets of the RGO were visible through the magnified FESEM image in the Figure 2.7 (b). The RGO coating on the motor resulted in a negatively charged motor surface which in turn imparted the electric field sensitivity to the motor, as schematically shown in the Figure 2.6 (b). The ζ-potential of the RGO motor in alkaline water solution (pH 10.1) was measured to be – 41.6 mV [69-71].

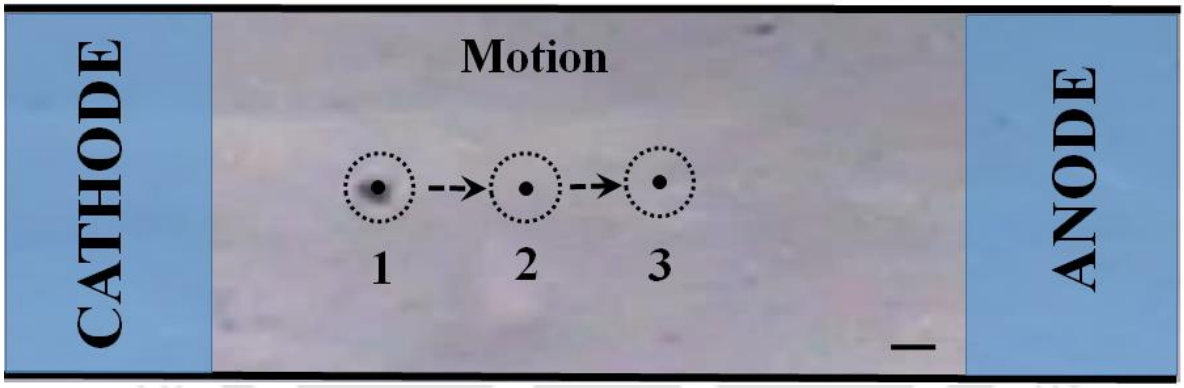

Figure 2.8. Electric field induced migration of the negatively charged RGO motor towards anode in aqueous NaOH solution (pH 10.1) inside a PDMS microchannel of ~800 µm width. The numbers 1, 2, and 3 on the image represent the position of the motor after 0 s, 30 s, and 60 s. The scale bar shown is of 100 µm.

Figure 2.8 show that when the RGO motor was put in an aqueous NaOH solution of pH 10.1, it migrated towards the anode, inside a PDMS microchannel. The applied electric field intensity was 0.5 kVm^{-1}. The electrically inert ~85 µm PMMA polymer beads under similar conditions was found to be stationary. This observation confirmed that the RGO motor indeed showed an electrophoretic migration. The experiment shown in the Figure 2.8 was an example where the transport of the RGO motor could be remotely regulated by the external electric field.

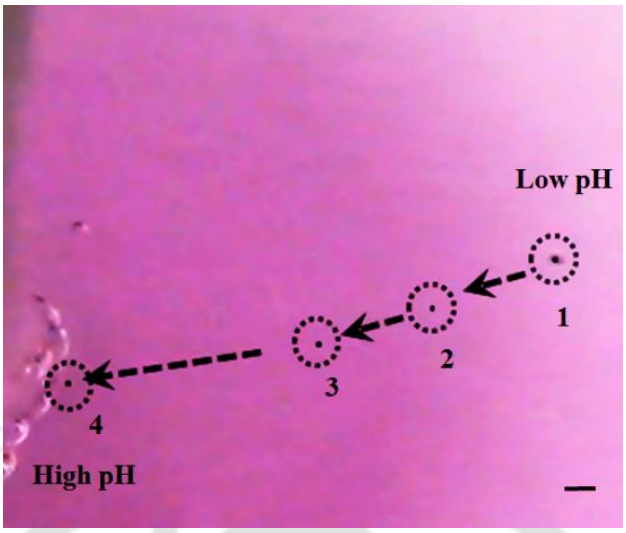

Figure 2.9. The chemotactic motion of the motor (dia. ~ 80 μm) towards a thread under a pH gradient. The numbers 1 – 4 represent the position of the motor after 0 s, 2 s, 4 s, and 6s, respectively. The scale bar at the bottom is of 0.5 mm.

Apart from the sensitivity towards the electric field in the alkaline medium, the RGO motor could also display chemotactic migration inside peroxide fuel. The chemical potential induced migrations were similar to the previously reported pH directed chemotaxis of the metal-nanoparticle coated polymeric microbeads [12, 15]. However, in the present motor for the catalytic activity the metal nanoparticles on the surface were replaced by the graphene sheets and the polymeric core was replaced by a glass bead. The RGO motors exhibited a directed motion when immersed in a bath of aqueous H_2O_2 solution (9% v/v) and then an alkali source (0.3M NaOH drip) was introduced near the motor to create a gradient of H_2O_2 concentration across the path of the motor. The RGO motor sensed the pH gradient and migrated towards the higher pH region as shown in the Figure 2.9. The RGO layers on the motor provided the catalytic activity originating from the heterogeneous surface decomposition of peroxide fuel to H_2O and O_2 [36]. The migration of RGO motor towards the imposed pH gradient took place due to the coupling effect between the two different types of H_2O_2 depletion, (a) heterogeneous catalytic

surface decomposition of H_2O_2 on the RGO layer, and (b) homogeneous catalytic decomposition of H_2O_2 due to the imposed pH gradient. The random decomposition of peroxide fuel on the RGO surface created a local imbalance of peroxide concentration surrounding the motor. This local imbalance of solute concentration was magnified by imposed the pH gradient. The differential pH gradient inside the peroxide bath was established by dripping alkali at the center of the petridish, which provided the necessary thrust for the migration of the motor towards the higher pH domain. The *local* heterogeneous decomposition of H_2O_2 across the motor surface was indicated by the issuance of O_2 bubbles while the motor migrated towards the target. The color gradient originating from the phenolphthalein indicator showed the spread of *global* pH gradient. Interestingly, Figure 2.9 shows that sometimes the O_2 bubbles nucleated on the motor-surface and grew in size to temporarily halt the motion.

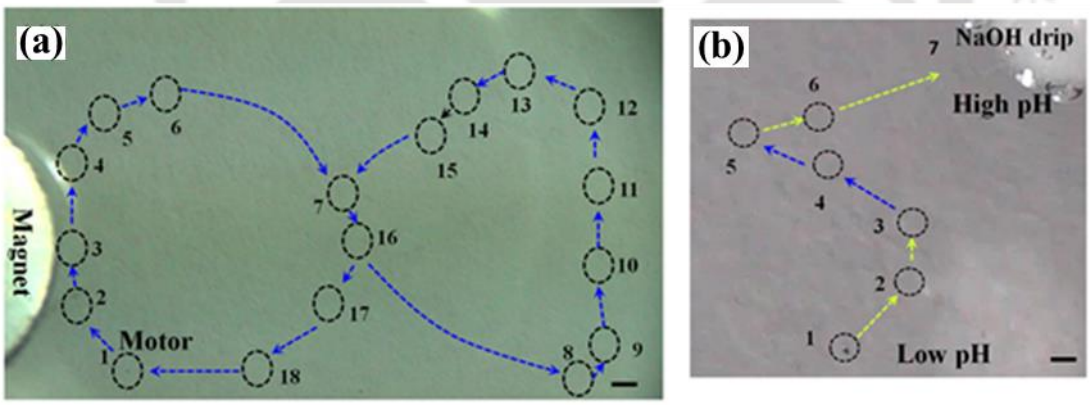

Figure 2.10. Controlled migration of the RGO motor through magnetic guidance and pH gradient. The precise magnetic-field induced navigation was used to move the motor in (a) English numeric '8' inside water medium and (b) English word 'S' inside H_2O_2 medium. The blue (darker) arrows depicted the magnetic controlled trajectory and the green (lighter) arrows show the trajectory under the influence of internal pH gradient. The numbers depict the instantaneous position of the microbot at different time intervals. The scale bar shown is of 0.5 mm length.

In such situations, the motor also exhibited migrations due to the bubble recoil when the O_2 bubble ejected out of the surface. The control experiments show that the uncoated glass beads did not move under similar condition. The experiments corroborated that the RGO motors could act as a carbon-based analogue of the previously designed metal-nanoparticle based motors. Embedding a small amount of the iron nanoparticles (FeNP) underneath the RGO layers of the motor not only increased the catalytic activity, but also allowed the FeNP@RGO motor to be sensitive towards the magnetic field, as schematically shown in the Figure 2.5 (c). Figure 2.9 show the guided motion of a FeNP@RGO motor, which was controlled solely by external magnet to migrate with the trajectory design of the number '8'.

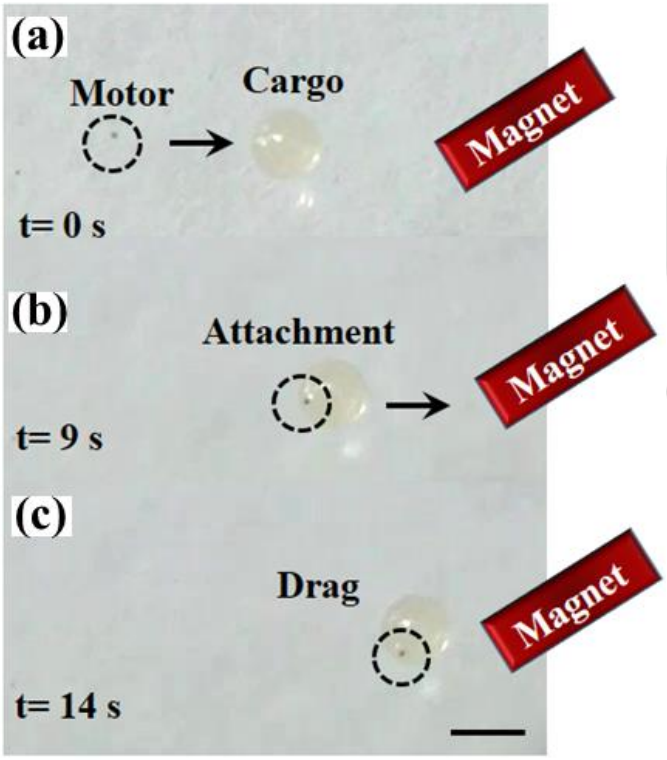

Figure 2.11. The image shows (a) 'seek', (b) 'upload', and (c) 'drag' operations of magnetically-guided polymeric cargo (1 mm diameter) inside a water medium. The scale bar at the bottom is of 1 mm. The arrow represents the trajectory of the motor.

The motor also navigated in predetermined trajectory of letter 'S' in aqueous medium under the coupled influence of pH gradient and magnetic field, as shown in the Figure 2.9 (b). These figures suggest that while in motion, the motor responded swiftly to the incessant change in spatial position of the external magnet. The ability of FeNP@RGO motors to migrate in a preselected route made it suitable for various biological and microfluidic applications.

One such example is the control of the movement of the motor for transportation and delivery a cargo inside confined environment. Figure 2.11 show that when exposed to an external magnetic field, the ~80 µm motor (~ 67 µg) was able to linearly drag a non-magnetic Amberlite polymer bead of ~ 1000 times heavier and ~13 times larger in size inside a petridish filled with water. The figure together show that the polymer bead was stationary before the motor got attached to the surface. However, after the attachment, the polymeric bead moved with a significantly higher speed inside the channel. The experiment suggested that the RGO motors could act as a cleansing agent, which can easily drag out non-useful items from the work area such as a blood vessel through remote control. The motor could also perform magnetically directed 'pick-up' and 'drop-off' operations inside a microchannel. Images (a) – (c) in the Figure 2.12 show that the motor could push a heavier/larger polymeric bead (~0.449 µg and ~350 µm in diameter) following a magnetically guided path to a target with the help of an external magnet. Following this, the image (d) shows that the motor was detached from the payload before could be taken back to the initial position, with the help of the magnetic guidance. We also performed experiments to show the coupled effects of chemical and magnetic control on the payload transport of RGO motor. As stated earlier, the motor autonomously migrated

towards the higher pH region in the presence of an imposed pH gradient. At this pH-induced motion, the remote magnetic control played a crucial role in tuning the course of motion.

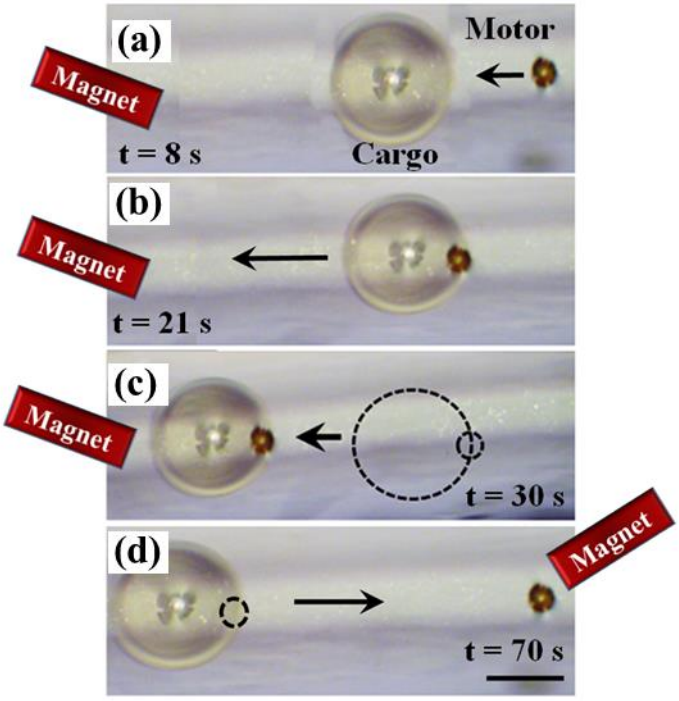

Figure 2.12. (a) Shows magnetically guided migration of motor towards spherical polymeric cargo (350 µm diameter), (b) 'pick-up', (c) 'transport', and (d) 'release' inside a water medium. The arrows represent the direction of the motion. The scale bar at the bottom is of 160 µm.

Figure 2.13 show the non-magnetic ~400 µm polymer bead (~0.67 µg) was loaded on the motor with the help of the magnetic guidance. Following this, the motor-polymer couple migrated towards the higher pH region in which the catalytic activity of the motor dragged the loaded cargo under the influence of the pH gradient. Concisely, the Figure 2.9 – 2.12 show some interesting applications through the multimodal controlled migrations of the RGO motor. The ability of the RGO motors to carry larger objects made it a potential candidate for dynamic payload transporter. At low Reynolds number, it can be assumed

that the force for propulsion (F_p) was balanced by the drag force (F_d) as, $F_p = F_d = 6\pi\eta RU$. Here η is the dynamic viscosity of the solution, R is the radius of the cargo with payload, and U is the linear velocity of the motor-polymer couple inside the solution.

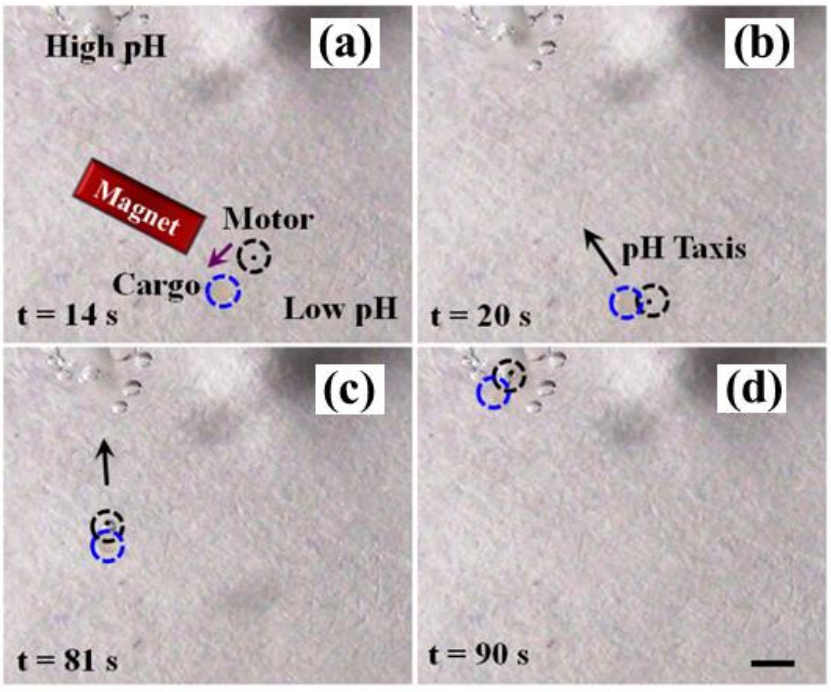

Figure 2.13. The image shows "Drag and Drop" cargo transportation under the coupled control of pH imposed gradient and external magnetic field, (a) The motor is migrated towards the cargo with the aid of external magnet, (b) The motor was attached to the cargo (c) the motor dragged the "heavy" cargo towards the higher pH zone under the influence of imposed pH gradient, (d) The motor migrated and collided to the alkali source. The scale bar at the bottom is of 1 mm.

For the polymeric bead of 1 mm diameter the experimental estimate of the maximum velocity was ~278 μms^{-1}, which suggests that the motor motion could generate force up to ~ 2619 pN under the magnetic guidance (Table 2.2). Similarly, for the pH triggered cargo transportation, the 350 µm polymer bead and 80 µm motor pair could overcome a drag force of ~754 pN. The analysis provides a decent estimate of the competence of the motor as a payload transporter inside microchannel network and drug delivery modules.

In order to study the velocity of the motor inside the tunable electric field, a series of experiments were performed by introducing the motor in alkaline pH 10.1 NaOH solution inside the PDMS microchannel. The cathode and anode (platinum electrodes) were separated by a distance of ~10 mm and the motor was introduced in a position in the alkaline solution, which was equidistance away from the electrodes.

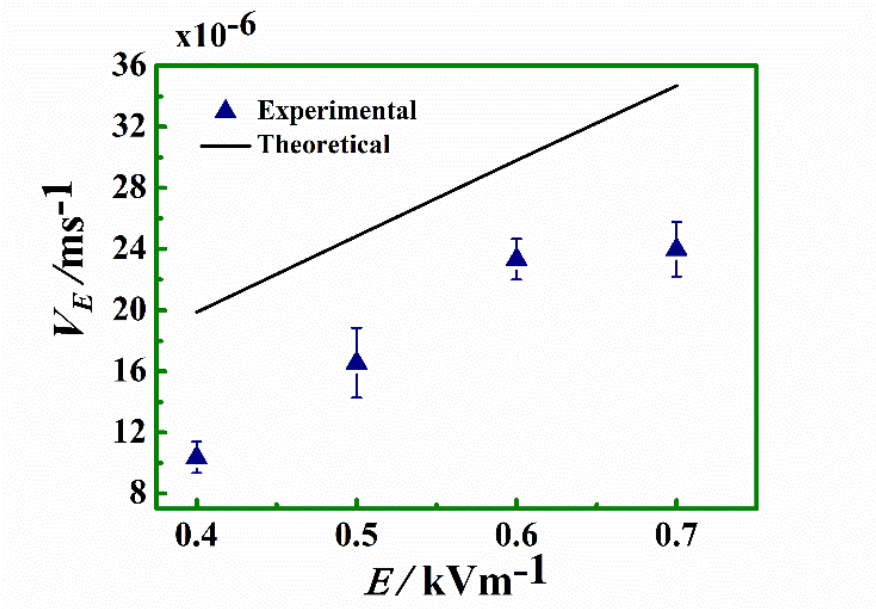

Figure 2.14. Variation in average velocity (V_E) of the RGO motor inside alkaline water solution (pH 10.1) with the variation in the electric field intensity (E).

The electric field intensity was varied from 0.4 to 0.7 kVm^{-1} and the motor migrated towards the cathode. The average velocity (V_E) was obtained from the time taken for a travelled distance of 1 mm from the origin. Figure 2.14 shows that at 0.4 kVm^{-1} the motor attained the speed of ~ 10 × 10^{-6} ms^{-1} and with an increase in the electric field intensity (E), the motor attained a maximum speed of ~ 24 × 10^{-6} ms^{-1} at 0.7 kVm^{-1}, which was equivalent to ~ 0.3 body lengths per second. The field intensity was not increased beyond a threshold value to avoid electro-splitting of the alkaline water solution. Further, Smoluchowski's equation [72] for the electrophoretic mobility of the particle and

electroosmotic mobility of the fluid inside the channel were employed to theoretically evaluate the speed of the RGO motor. We assumed that the electrophoretic motion of the motor was solely due to development of ζ-potential on the motor surface in the alkali solution of pH 10.1 while the ζ-potential on the surface of the PDMS channel stimulated the electroosmotic flow. The detailed procedure for the theoretical calculations parameter is provided in the Table 2.1 Figure 2.14 shows that the experimentally determined velocity of the RGO motor was the same order of magnitude as was predicted theoretically. The plot also shows that V_E increased with E in both experiments (symbols) and theoretical predictions (solid line). The difference in the magnitudes of the values in the experiments and the theoretical predictions could be attributed to the non-rigorous nature of the Smoluchowski's equation while theoretically evaluating the electrophoretic mobility.

2.3.1 Calculations for theoretical velocity of the RGO motor

The RGO motor was suspended in aqueous NaOH solution of pH 10.1 and subjected to an external DC electric field. The motor assumed to have negligible influence due to the buoyancy and Brownian motion. Under this condition, the ζ-potential of the RGO (ζ_{RGO}) was found to be of - 41.6 mV [70], which was employed to calculate the theoretical electrophoretic velocity (V_{EP}) from Smoluchowski's equation, $V_{EP} = \frac{\varepsilon\varepsilon_o\zeta_{RGO}}{\eta}E$ [74, 75].

The ζ-potential of PDMS (ζ_{PDMS}) surface was found to be -30 mV [73], which was employed to calculate the theoretical electroosmotic velocity from Smoluchowski's equation, $V_{EO} = \frac{\varepsilon\varepsilon_o\zeta_{PDMS}}{\eta}E$ [75]. We assumed that electroosmotic flow profile to be uniform inside the microchannel, which had dimensions much larger than the Debye length and uniform surface charge density. The V_{EP} and V_{EO} were in the same direction towards the anode and the theoretical velocity of the motor (V_E) at any instant was

considered to be summation of the electroosmotic and electrophoretic mobility, $V_E = V_{EP} + V_{EO}$ [74, 75]. The necessary parameters to evaluate the theoretical velocity of the RGO motor are tabulated in Table 2.1.

Table 2.1. Parameters for calculation of theoretical velocity (V_E) for the RGO motor under electric field

ζ_{RGO}	ζ_{PDMS}	**Viscosity of water (η)**	**Dielectric constant of water (ε)**	**Permittivity of free space (ε_0)**
- 0.0416 V	- 0.030 V	0.001 Pa s	78.5	8.854×10^{-12} F m^{-1}

The experiments were also performed to investigate the characteristics of the sole pH induced motion employing a RGO motor inside a bath of 9.0% (v/v) aqueous H_2O_2 solution while the pH of the reservoir was varied from 10.1 to 12.5 in absence of electric and/or magnetic field.

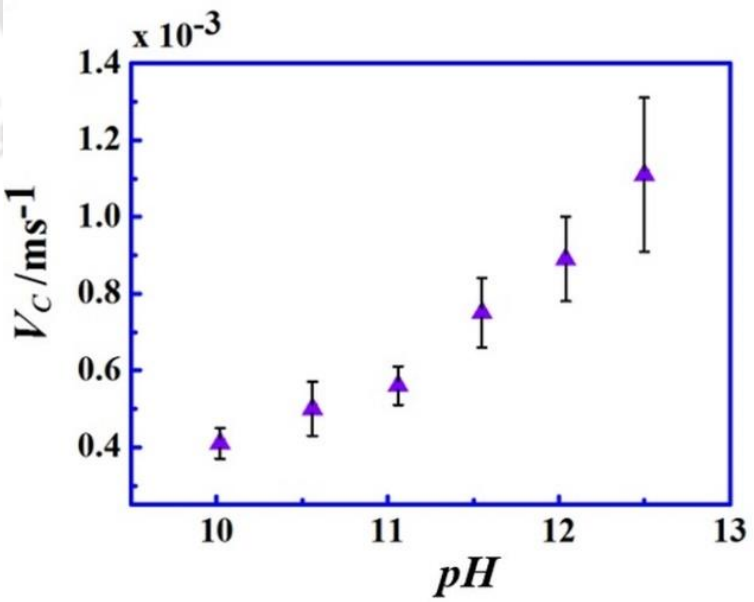

Figure 2.15. Variation in the average velocity (V_C) of the RGO motor inside 9% (v/v) H_2O_2 bath when the pH was varied.

Figure 2.15 shows that at lower pH the average speed (V_C) attained by the motor was around 4.1 × 10^{-4} ms^{-1}. However, with an increase in the pH value, the V_C increased significantly. The motor speed was as high as ~10^{-3} ms^{-1}, which was ~13 body lengths per second, at the pH value of ~12.5.

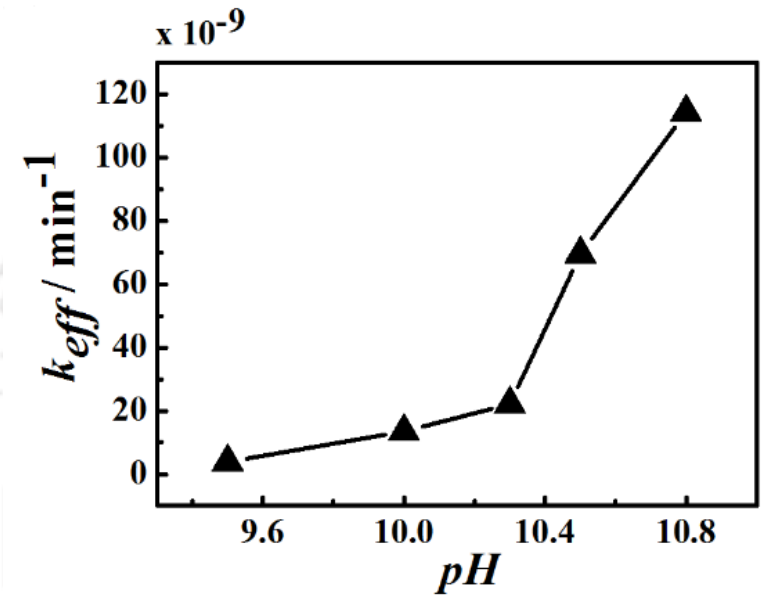

Figure 2.16. Variation in effective rate constant (k_{eff}) of hydrogen peroxide (H_2O_2) decomposition with change in pH for a catalytic motor.

The plot 2.15 shows the variation in the effective rate constant (k_{eff}) for the 9% (v/v) hydrogen peroxide (H_2O_2) decomposition by a single catalytic motor at different pH. In presence of RGO motor, the rate of decomposition of 9% (v/v) H_2O_2 on the motor surface grew linearly with increase in the pH of H_2O_2 bath. The effect of magnetic field on average velocity (V_M) of the FeNP@RGO motor was also obtained by varying the magnetic field from 40 mT to 110 mT. Figure 2.17 shows that the velocity increased with increasing magnetic strength (F_{mag}) exerted on the motor. The average speed (V_M) attained by the motor was around 1.8 × 10^{-4} ms^{-1} at ~43 mT. However, with increase in magnetic field strength, the V_M increased to as high as 10^{-3} ms^{-1} at ~103 mT.

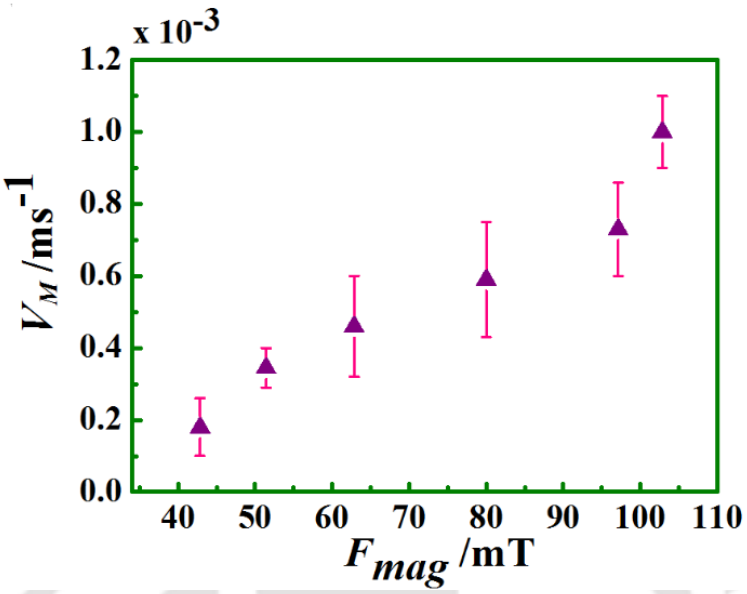

Figure 2.17. Variation in average velocity (V_M) of the spherical RGO motor inside aqueous medium under the influence of magnetic field (F_{mag}).

The plot confirmed that the motors could be easily guided magnetically in an aqueous environment. Figures 2.14 – 2.17 together suggest that by coupling the chemical, magnetic, and electric field induced motions the motor can further be accelerated or decelerated inside open and confined surroundings, as previously shown in the Figures 2.8 and 2.13.

2.3.2 Calculations for the maximum drag force exerted by RGO motor

Dynamic viscosity (η) of diluted aqueous 9% (v/v) H_2O_2 solution in water at room temperature was considered to be 10^{-3} Pa s. The gravitational effect was neglected as the polystyrene beads were neutrally buoyant in the solution. The linear velocity of the cargo was estimated from the experimental videos for magnetic and pH gradient guidance while in transit with the motor. The experiments were repeated thrice in order to determine the average linear speed (U) of the cargo and to calculate the drag force (F_d). The expression

for Stokes drag force ($F_d = 6\pi\eta RU$) for a spherical particle was employed for the calculations.

Table 2.2. Calculation of the drag force (F_d) experienced by motor for transportation of the cargo

Type of controlled motion	Radius of the Cargo R (μm)	Average Velocity U (μm/s)	Drag Force F_d (pN)
Magnetic (inside petridish)	500	278	2618.76
Magnetic (inside microchannel)	175	88.3	291.12
pH gradient & magnetic field (inside petridish)	200	200	753.6

Table 2.3. Calculation of the mass-ratio and size-ratio

	Radius (m)	Density (kgm^{-3})	Mass (kg)	Mass-ratio	Size-ratio
Amberlite bead	5.00×10^{-4}	1280	6.70×10^{-7}	1000	12.5
Amberlite bead	1.75×10^{-4}	1280	2.87×10^{-8}	42.88	4.38
Amberlite bead	2.00×10^{-4}	1280	4.29×10^{-8}	64	5
RGO motor	4.00×10^{-5}	2500	6.70×10^{-10}	-	-

$$\text{Mass ratio} = \frac{\text{Mass of Amberlite bead}}{\text{Mass of Graphene coated glass bead}} . \qquad (2.3.1)$$

$$\text{Size ratio} = \frac{\text{Size of Amberlite bead}}{\text{Size of Graphene coated glass bead}} . \qquad (2.3.2)$$

The calculations suggest that the RGO motor (~67 μg) successfully drove out a ~1000 times heavier and ~13 larger Amberlite payload (~0.67 mg) to display the ability to overcome a drag force of ~2619 pN (Table 2.2) with the magnetic guidance.

2.4. SUMMARY

We demonstrate the synthesis and applications of versatile RGO superbot, which is responsive towards the electrical, magnetic, and chemical triggers. While the chemical locomotion recorded a speed as high as ~13 body lengths per second, the external magnetic field could move the motor at a speed many fold larger than the chemical trigger. Importantly, the multimodal control on the motor could engender complex coupled motions useful for many futuristic applications. For example, the microbot exhibited interesting actions such as 'approach', 'attach', 'drag', and 'drop' of polymeric inert payloads of ~1000 times heavier and ~13 times bigger in size. The motor could overpower a drag force as high as ~2619 pN with the guidance from magnetic field and the pH gradient. The *in situ* and external triggers showed precise galvanotactic, magnetotactic, and chemotactic migrations in a targeted direction inside the liquid medium. This is in stark contrast to the recently reported random migrations of graphene – metal oxide based motors [35]. The reported RGO motors could find important applications in clinical restoration of stenotic blood vessels, cleaning of blockages in blood vessels, drug delivery, and diverse bio-carriers. The pH sensitivity of the motors could also enable them to selectively trace out the diseased cells out of a cell population by sensing the variation in the pH across the healthy and infected cells.

REFERENCES

1. W. Gao, D. Kagan, O. S. Pak, C. Clawson, S. Campuzano, E. Chuluun-Erdene, E. Shipton, E. E. Fullerton, L. Zhang, E. Lauga, and J. Wang, *Small*, 2012, **8,** 460-467.

2. D. Kagan, R. Laocharoensuk, M. Zimmerman, C. Clawson, S. Balasubramanian, D. Kang, D. Bishop, S. Sattayasamitsathit, L. Zhang, and J. Wang, *Small*, 2010, **6**, 2741-2747.

3. A. Sen, D. Patra, S. Sengupta, W. Duan, H. Zhang, and R. Pavlick, *Nanoscale*, 2013, **5**, 1273-1283.

4. W. Xi, A. Solovev, AN. Ananth, D. Gracias, S. Sanchez, and OG. Schmidt, *Nanoscale*, 2013, **5**, 1294-1297.

5. F. Ullrich, C. Bergeles, J. Pokki, O. Ergeneman, S. Erni, G. Chatzipirpiridis, S. Pane, C. Framme, and B. J. Nelson, *Investig. Ophthalmol. Vis. Sci.*, 2013, **54**, 2853-2863.

6. S. Campuzano, D. Kagan, J. Orozco, and J. Wang, *Analyst*, 2011, **136**, 4621-4630.

7. M. García, J. Orozco, M. Guix, W. Gao, S. Sattayasamitsathit, A. Escarpa, A. Merkoci, and J. Wang, *Nanoscale*, 2013, **5**, 1325-1331.

8. L. K. E. A. Abdelmohsen, F. Peng, Y. Tu, and D. A. Wilson, *J. Mater. Chem. B*, 2014, **2**, 2395-2408.

9. K. K. Dey, P. B. Ranjan, A. Paul, S. Basu, and A. Chattopadhyay, *J. Colloid Interface Sci.*, 2010, **348**, 335-341.

10. W. F. Paxton, K. C Kistler, C. C. Olmeda, A. Sen, S. K. Angelo, Y. Cao, T. E. Mallouk, P. E. Lammert, and V. H. Crespi, *J. Am. Chem. Soc.*, 2004, **126**, 13424-13431.

11. U. K. Demirok, R. Laocharoensuk, K. M. Manesh, and J. Wang, *Angew. Chem. Int. Ed.*, 2008, **47**, 9349-9351.

12. K. K. Dey, S. Bhandari, D. Bandyopadhyay, S. Basu, and A. Chattopadhyay, *Small*, 2013, **9**, 1916-1920.

13. S. K. Sailapu, and A. Chattopadhyay, *Angew. Chem. Int. Ed.*, 2014, **53**, 1521-1524.

14. L. Soler, V. Magdanz, V. M. Fomin, S. Sanchez, and O. G. Schmidt, *ACS Nano*, 2013, **7**, 9611-9620.

15. A. K. Singh, K. K. Dey, A. Chattopadhyay, T. K. Mandal, and D. Bandyopadhyay, *Nanoscale*, 2014, **6**, 1398-1405.

16. M. Xuan, J. Shao, X. Lin, L. Dai, and Q. He, *Chem. Phys. Chem.*, 2014, **15**, 2255-2260.

17. L. Baraban, S. M. Harazim, S. Sanchez, and O. G. Schmidt, *Angew. Chem. Int. Ed.*, 2013, **52**, 5552-5556.

18. T. R. Kline, W. F Paxton, T. E Mallouk, and A. Sen, *Angew. Chem.*, 2005, **117**, 754-756.

19. P. Fischer, and A. Ghosh, *Nanoscale*, 2011, **3**, 557-563.

20. G. Zhao, and M. Pumera, *Langmuir,* 2013, **29**, 7411-7415.

21. G. Loget, and A. Kuhn *Nat. Commun.*, 2011, **2**, 1-6.

22. S. Balasubramanian, D. Kagan, K. M. Manesh, P. Calvo-Marzal, G. U. Flechsig, and J. Wang, *Small,* 2009, **5**, 1569-1574.

23. H. Zhang, W. Duan, L. Liu, and A. Sen, *J. Am. Chem. Soc.*, 2013, **135**, 15734-15737.

24. G. Zhao, and M. Pumera, *J. Phys. Chem. B*, 2012, **116**, 10960-10963.

25. A. A. Solovev, E. J. Smith, C. C. Bof' Bufon, S. Sanchez, and O. G. Schmidt, *Angew. Chem. Int. Ed.* 2011, **50**, 10875-10878.

26. W. Wang, S. Li, L. Mair, S. Ahmed, T. J. Huang, and T. E. Mallouk, *Angew. Chem. Int. Ed*., 2014, **53**, 3201-3204.

27. V. C. Sanchez, A. Jachak, R. H. Hurt,and A. B. Kane, *Chem. Res. Toxicol*., 2012, **25**, 15-34.

28. A. K. Geim, and K. S.Novoselov, *Nat. Mater.,* 2007, **6**, 183-191.

29. A. A. Balandin, *Nat. Mater*., 2011, **10**, 569-581.

30. Y. Wang, Z. Li, J. Wang, J. Li, and Y. Lin, *Trends Biotechnol*., 2011, **29**, 205-212.

31. Y. Zhu, S. Murali, W. Cai, X. Li, J. W. Suk, J. R. Potts, and R. S. Ruoff, *Adv. Mater.*, 2010, **22**, 3906-3924.

32. A. M. Pinto, I. C. Gonçalves, and F. D. Magalhães, *Colloids Surf. B,* 2013, **111**C:188-202.

33. R. Laocharoensuk, J. Burdick, and J. Wang, *ACS Nano,* 2008, **2**, 1069-1075

34. K. Yao, M. Manjare, C. A. Barrett, B. Yang, T. T. Salguero, and Y. Zhao, *J. Phys. Chem. Lett.*, 2012, **3**, 2204-2208.

35. X. Chen, G. Wu, T. Lan, W. Chen, *Chem. Commun.*, 2014, **50**, 7157-7159.

36. K. V. Voitko, R. L. D. Whitby, V. M. Gun'ko, O. M. Bakalinska, M. T. Kartel, K. Laszlo, J. S. Zięba, R. Leboda, E. Tombacz, I. Y. Toth, K. Kovacs, and S. V. Mikhalovsky, *J. Colloid Interface Sci.*, 2011, **361**, 129-136.

37. B. Dong, T. Zhou, and H. Zhang, C. Y. Li, *ACS Nano* 2013, **7**, 5192-5198.

38. M. Liu, L. Liu, W. Gao, M. Su, Y. Ge, L. Shi, H. Zhang, B. Dong, and C. Y. Li, *Nanoscale,* 2014, **6**, 8601-8605.

39. J. Chen, H. Peng, X. Wang, F. Shao, Z. Yuan, and H. Han, *Nanoscale*, 2014, **6**, 1879-1889.

40. S. Liu, T. H. Zeng, M. Hofmann, E. Burcombe, J. Wei, R. Jiang, J. Kong, and Y. Chen, *ACS Nano*, 2011, **5**, 6971-6980.

41. A. R. Maity, A. Chakraborty, A. Mondal, and N. R. Jana, *Nanoscale*, 2014, **6**, 2752-2758.

42. B. F. Machado, P. Serp, *Catal. Sci. Technol.*, 2012, **2**, 54-75.

43. W. Gao, and J. Wang *ACS Nano* 2014, **8**, 3170-3180.

44. L. A. Al-Khateeb, S. Almotiry, and M. A. Salam. *Chem. Eng. J.*, 2014, **248**, 191-199.

45. J. Burdick, R. Laocharoensuk, P. M. Wheat, J. D. Posner, J. Wang, *J. Am. Chem. Soc.* 2008, **130**, 8164-8165.

46. J. Wang, *Lab Chip*, 2012, **12**, 1944-1950.

47. S. Sundararajan, P. E. Lammert, A. W. Zudans, V. H. Crespi, A. Sen, *Nano Lett.*, 2008, **8**, 1271-1276.

48. J. Simmchen, A. Baeza, D. Ruiz, M. J. Esplandiu, M. Vallet-Regí, *Small*, 2012, **8**, 2053-2059.

49. L. Baraban, D. Makarov, R. Streubel, I. Mönch, D. Grimm, S. Sanchez, and O. G. Schmidt, *ACS Nano*, 2012, **6**, 3383-3389.

50. S. Roy, N. Soin, R. Bajpai, D. S. Misra, J. A. McLaughlin, and S. S. Roy, *J. Mater. Chem.*, 2011, **21**, 14725-14731.

51. S. Wu, Q. He, C. Tan, Y. Wang, and H. Zhang, *Small*, 2013, **9**, 1160-1172.

52. Z. Yue, P. Lv, H. Yue, Y. Gao, D. Ma, W. Wei, and G. Ma, *Chem. Commun.*, 2013, **49**, 3902-3904.

53. L. Feng, L. Wu, and X. Qu, *Adv. Mater.*, 2013, **25**, 168-186.

54. M. Tian, W. Feng, J. Ye, and Q. Jia, *Anal. Methods*, 2013, **5**, 3984-3991.

55. D. C. Marcano, D. V. Kosynkin, J. M. Berlin, A. Sinitskii, Z. Sun, A. Slesarev, L. B. Alemany, W. Lu, and J. M. Tour, *ACS Nano*, 2010, **4**, 4806-4814.

56. G. Eda, G. Fanchini, and M. Chhowalla, *Nat. Nanotechnol.*, 2008, **3**, 270-274.

57. W. Gao, M. Majumder, L. B. Alemany, T. N. Narayanan, M. A. Ibarra, B. K. Pradhan, and P. M. Ajayan, *ACS Appl. Mater. Interfaces*, 2011, **3**, 1821-1826.

58. M. M. Benjamin, R. S. Sletten, R. P. Bailey, and T. Bennett, *Water Res.*, 1996, **30**, 2609-2620.

59. K. C. Huang, and S. H. Ehrman, *Langmuir*, 2007, **23**, 1419-1426.

60. M. K. S. Verma, A. Majumder, and A. Ghatak, *Langmuir*, 2006, **22**, 10291-10295.

61. I. K. Moon, J. Lee, R. S. Ruoff, and H. Lee, *Nat. Commun.*, 2010, **1,** 73:1-6.

62. K. Yao, M. Manjare, C. A. Barrett, B. Yang, T. T. Salguero, and Y. Zhao, *J. Phys. Chem. Lett.*, 2012, **3**, 2204-2208.

63. Z. Ni, Y. Wang, T. Yu, and Z. Shen, *Nano Res.*, 2008, **1**, 273-291.

64. M. Wang, J. Cheng, M. Li, and F. He, *Physica B*, 2011, **406**, 3865-3869.

65. A. Kassir-Bodon, T. Deschamps, C. Martinet, B. Champagnon, J. Teisseire, and G. Kermouche, *Int. J. Appl. Glas. Sci*., 2012, **3**, 29-35.

66. Y. H. Lin, Y-C. Chi, and G. R. Lin, *Laser Phys. Lett.*, 2013, **10**, 055105:1-10.

67. H. Jabeen, V. Chandra, S. Jung, J. W. Lee, K. S. Kim, and S. B. Kim, *Nanoscale*, 2011, **3**, 3583-3585.

68. W. Xing, G. Lalwani, I. Rusakova, and B. Sitharaman, *Part. Part. Syst. Charact.*, 2014, **31**, 745-750.

69. T. Szabó, O. Berkesi, P. Forgó, K. Josepovits, Y. Sanakis, D. Petridis, and I. Dekany, *Chem. Mater.*, 2006, **18**, 2740-2749.

70. D. Li, M. B. Müller, S. Gilje, R. B. Kaner, and G. G. Wallace, *Nat. Nanotechnol*, 2008, **3**, 101-105.

71. B. Konkena, and S. Vasudevan, *J. Phys. Chem. Lett.*, 2012, **3**, 867-872.

72. A. Sze, D. Erickson, L. Ren, and D. Li, *J. Colloid Interface Sci.*, 2003, **261**, 402-410.

73. B. J. Kirby, and E. F. Hasselbrink, *Electrophoresis*, 2004, **25**, 203-213.

74. M. H. Oddy, and J. G. Santiago, *J. Colloid Interface Sci*., 2004, **269**, 192-204.

75. V. Tandon, S. K. Bhagavatula, W. C. Nelson, and B. J. Kirby, *Electrophoresis*, 2008, **29**, 1092–1101.

Chapter 3

Magnetically Guided Push-Pull Motility of Liquibots for Drug-Delivery

3.1 INTRODUCTION

Over the past few decades, droplet microfluidics has shown significant potential in staging paradigm shifts in the technologies related to the biomolecule detection, drug-delivery, 3-D printing, therapeutics, diagnostics, and digital electronics [1-5]. In particular, the self-motile microscale digitized objects guided by various in-situ or external stimulants have shown their remarkable potential as the next generation transporters of essential vitamins, antibiotics, minerals, anti-cancer agents, or enzymes [6-8]. A number of pioneering works have shown that these futuristic devices can be propelled by Marangoni effect [9-10], chemiosmotic force [11], electric field [12], photonic [13] or acoustic [14] excitations, and electromagnetic fields [15-16]. These studies also unveiled the pathways to include the specialties of nanoscale particles, rods, tubes, or fibres on the solid or soft-solid objects targeting various cutting-edge applications [17-19]. In comparison, the liquid micro-propellers having efficacies very similar to or better than their nano-enabled solid or soft-solid counterparts have started making appearance in the academic arena only in the recent years [11,20]. However, integrating the specialties of these nanoscale materials into the liquid droplets has largely been limited by the conditional agglomeration of solids from the bulk, which has somewhat clipped the flight of the applications associated with the droplet based locomotion [21,22].

In this direction, one of the major challenges has been to infuse magnetic properties to the micro or nanoscopic liquid droplets [23]. A droplet suspended with the magnetic micro or nanoscale particles or fibres often encounter the problem of phase-separation of the nanoparticles or nanofibres due to nucleation followed by settling [24]. The problem becomes more severe in presence of an external

magnetic field where the nanoscopic objects are preferentially attracted towards the magnet causing a faster solid-liquid separation from a suspension [25]. Previous studies suggest that the use of surfactant coated nanoparticles can be one of the temporary solutions to stabilize solid-liquid suspensions at the microscale [26] and delay the phase separation [27]. Alternatively, use of paramagnetic ionic liquids and ferrofluids has also been suggested to resolve this problem [28-31]. However, most of these solutions are either temporary or costly or toxic. Further, infusing different types of magnetic properties to the microdroplets composed of commonly available materials has been an open challenge so far.

3.2 EXPERIMENTAL SECTION

3.2.1 Materials

The chemicals, chloroform ($CHCl_3$), silicone oil ($C_6H_{18}OSi_2$), oleic acid ($C_{18}H_{34}O_2$), manganese(II) chloride teterahydrate ($MnCl_2{\cdot}4H_2O$) and sodium chloride (NaCl) was purchased from Merck (India) ltd. Fluorescein sodium salt dye was purchased from Sisco Research Laboratories Pvt. Ltd. Ferrous chloride ($FeCl_3$) was purchased from the Sigma-Aldrich chemicals. The milli-Q grade deionized water was used for cleaning and to prepare the solutions. The drug Paracetamol (P-500, Apex India) was purchased from local medical store.

3.2.2 Methods

Synthesis and motions of waterbots and oilbots: The waterbots were prepared by mixing a known amount of paramagnetic manganese ($MnCl_2{\cdot}4H_2O$) or iron ($FeCl_3$) salts in DI water. The manganese salt in water dissolved fully (limiting solubility 4.5 M) to give a transparent waterbot and the iron salt dissolved in water led to a

greenish yellow waterbot. The oilbots were prepared by emulsifying water loaded salt into the oil, which were rather opaque. A 40 mm petri dish filled with 7 mL of either chloroform (for a waterbot) or water (for an oilbot) was the *in vitro* system to perform the experiments on the motion of the liquibots. The petri dish was cleaned after every experiment and the external vibrations and disturbances were avoided during the experiments. In order to show the motion of a paramagnetic waterbot, a droplet of aqueous manganese chloride (volume 1 – 10 µL) or ferrous chloride (volume 1 – 50 µL) was put on the surface of chloroform bath and then pulled by either an electromagnet or a permanent magnet. The motion of the diamagnetic waterbot was shown by putting a droplet of aqueous sodium chloride on the surface of chloroform bath and then pushed by a permanent magnet. The 1 ml oilbot was prepared from an emulsion using 1:1 W/O ratio of aqueous $MnCl_2$ solution and oleic acid with 5 mg paracetamol drug. The emulsion was found to be stable after 5 min vigorous shaking. The oilbot could also be made paramagnetic based on the choice of the salt for emulsification and was moved on a water surface with the help the permanent magnet. Paracetamol and fluorescent particles could be mixed with all types of reported liquibots and was transported and delivered to the targeted locations. The motions were recorded with a camcorder for further analysis.

3.2.3 Velocity measurements

In order to measure the velocities of the paramagnetic waterbots, the petri dish filled with chloroform was placed in between two poles of an electromagnet. The waterbot was placed carefully on the chloroform bath with the help of suitable micropipette, near one of the poles of the magnet. A constant magnetic field was

applied with the help of electromagnet or permanent magnet while the liquibot migrated. In order to measure the velocities of the diamagnetic waterbots, the permanent magnet was placed underneath a petri dish filled with chloroform before the waterbot was dispensed at the air-chloroform interface of the bath. A graph paper with 1 mm scale bar was placed underneath to measure the distance travelled by the liquibots. The migration towards (away) the poles of the paramagnetic (diamagnetic) liquibots was recorded with a camcorder to measure the time for displacements. Instantaneous velocity (V_i) was calculated for every 1 mm displacement per unit time and then the average velocity (V_m) was calculated for 1 cm displacement per unit time. The experiments were repeated thrice in order to confirm the repeatability of the reported velocities. Droplet splitting experiments were performed by initially attaching a transparent sheet on a paper surface, then coating the open surface of the transparent sheet with a very thin layer of oleic acid, and thereafter placing a $FeCl_3$ loaded waterbot on the surface coated with oleic acid. A permanent magnet was employed to stretch the waterbots for splitting into parts and then join them.

3.2.4 Characterizations

The magnetization was determined by vibrating sample magnetometer (VSM, Lakeshore GMW magnetic systems 3474-140). The motion of the droplet was recorded with a Sony HD Camcorder (model: HDR-XR160E). The electromagnet model EMU-50V with a constant current power supply unit (DPS-50) was employed to apply magnetic field and the field strength was measured by a Digital Gaussmeter Model DGM-102 (SES Instruments, India). The migrations of the microscopic and fluorescent liquibots were observed under the Leica DM2500

upright microscope. The motions of the microemulsion oilbot image were recorder by the Leica DM2500 upright microscope.

The magnetization curve for the paramagnetic and diamagnetic liquibots were obtained from the VSM data at 25°C by varying the magnetic field from −15 to 15 kG. The magnetization curves in Supporting Figure S1a show that the liquibot loaded with manganese (II) chloride was highly paramagnetic. The magnetization curves in Figure 3.9 (b) show that liquibot loaded with sodium chloride was diamagnetic in nature. The other paramagnetic salt $FeCl_3$ also showed paramagnetic behaviour when loaded inside the liquibot as shown by Figure 3.9 (c).

3.3 RESULT AND DISCUSSION

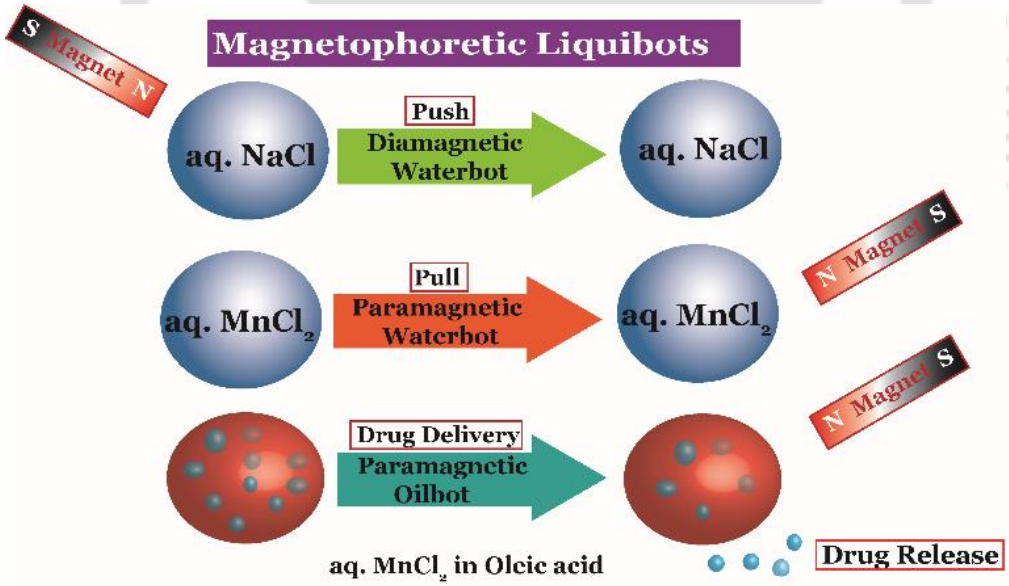

Figure 3.1. Schematic illustration of liquibots undergoing magnetic field induced motion. A diamagnetic waterbot (aq. NaCl soln.) showing a push motion, a paramagnetic waterbot (aq. $MnCl_2$ soln.) showing a pull motion, and a paramagnetic oilbot (droplets of aq. $MnCl_2$ soln. suspended in oleic acid) showing pull and delivery motions.

Figure 3.1 schematically shows that liquid droplets composed of aqueous solutions of the paramagnetic or diamagnetic salts could engender interesting magnetic field

induced motions. The transparent to translucent to opaque salt-laden droplets, namely, the 'liquibots' could show facile pull, push, veer, halt, or reverse motions under the remote guidance of an external magnet. For example, a 'waterbot' loaded with paramagnetic salt could be pulled while the same loaded with diamagnetic salt could be pushed with the help of a magnetic guidance. The speed of the liquibots could be modulated by altering the size, magnetic field strength, and salt-loading. In addition, the proposed liquibots could be split into parts or joined or arranged in an ordered manner on a slippery solid surface, which was previously possible only through ferrofluids[31]. The magnetic field guided actuation and migration shown by the liquibots indicated that they might be suitable for a number of recently proposed droplet microfluidic applications based on electric field [32-33].

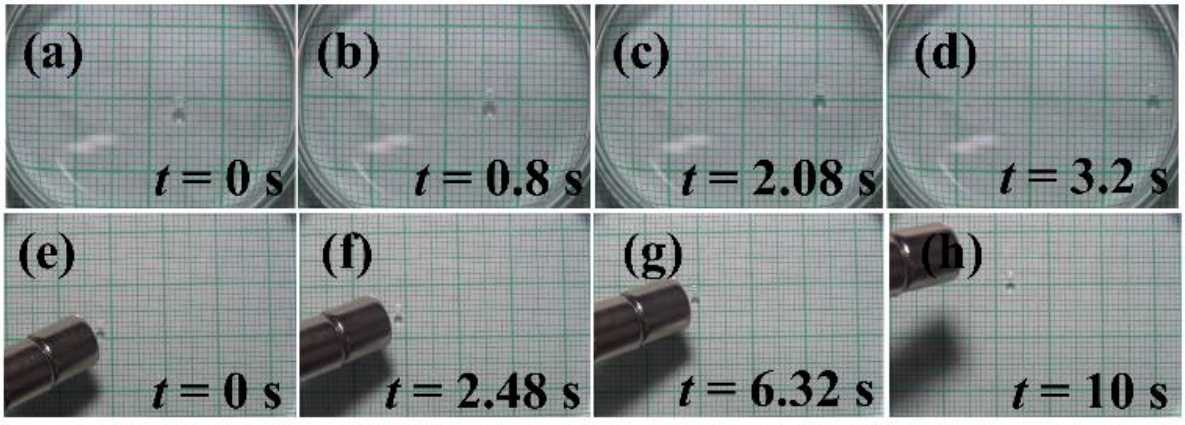

Figure 3.2. Images (a-d) show the magnetic field induced 'pull' motion of a 5 µL paramagnetic waterbot loaded with 0.5M $MnCl_2$ at 0 s, 0.8 s, 2.08 s, and 3.2 s, respectively, on a petri dish filled with chloroform and under the influence of a electromagnet of strength 148 mT. Images (e-h) show the magnetic field induced 'push' motion of 3 µL diamagnetic waterbot loaded with 1M NaCl at 0 s, 2.48 s, 6.32 s, and 10 s, respectively, on chloroform filled petri dish and under the influence of a permanent magnet of strength 120 mT. The minimum box dimension of graph was 1 mm × 1 mm.

Importantly, we have also shown a recipe to synthesize water-in-oil liquibots, which could fluoresce, transport as well as release drugs to the targeted locations through remote magnetic guidance. The reported prototype is expected to improve the efficiency of many recently reported droplets based sensors [34,35], drug transporters [36-38], environmental remediates [39], and microreactors [40-43].

Figure 3.2 (a-d) show that a transparent paramagnetic waterbot composed of 0.5M aqueous $MnCl_2$ was 'pulled' by an electromagnet having field strength of 148 mT on a chloroform bath at a maximum speed of 3.44 mm/s. In comparison, Figure 3.2 (e-h) show that a transparent diamagnetic waterbot composed of aqueous solution of 1M NaCl could be 'pushed' by a permanent magnet of strength 120 mT at a maximum speed of ~1.4 mm/s on the same bath.

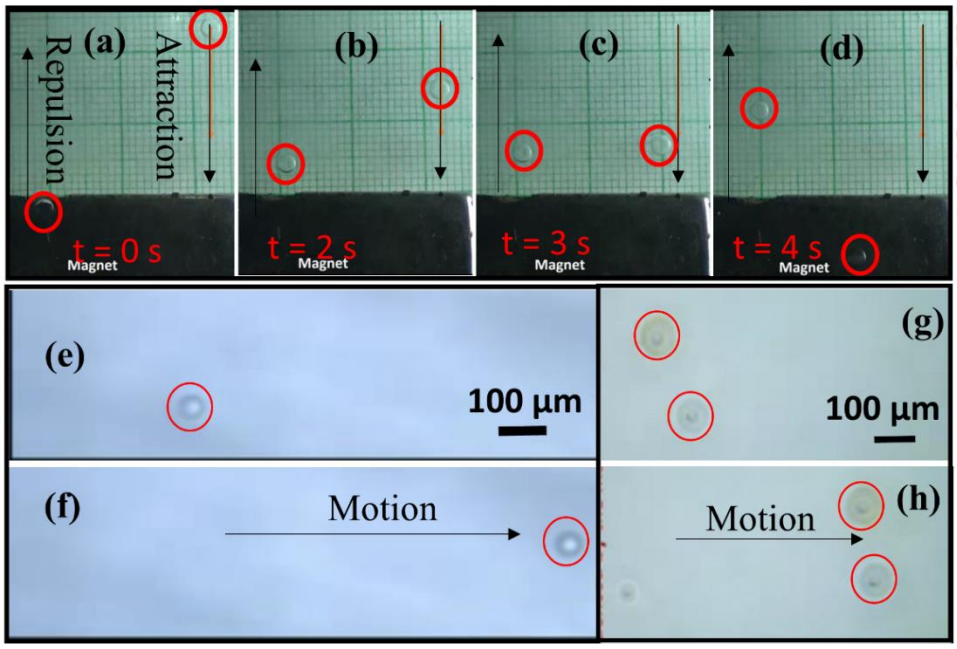

Figure 3.3. Images (a-d) show the magnetic field induced motion attraction and repulsion motion of diamagnetic and paramagnetic droplet The minimum box dimension of graph was 1 mm × 1 mm, Images (e-f) show the 40 µm paramagnetic droplet motion under magnetic field, Images (g-h) show the multiple droplet motion This experiment has the scale bar 100 µm.

Control experiments suggested that a de-ionized (DI) waterbot was unable to show such motions on the same chloroform bath.

Both the diamagnetic and paramagnetic waterbots moved at the air-chloroform interface because of the higher density of chloroform than the waterbots. Figure 3.3 (a-d) show a contrasting pull and push (attractive and repulsive) reciprocating motion of the 10 μl transparent paramagnetic (right side) and diamagnetic (left side) waterbots when placed near a permanent magnet of strength 240 mT. In the Figure 3.3 (e-h), we have shown the motion of a miniaturized version of the single and multiple paramagnetic waterbot of diameter of 40 μm moving at a speed of ~2 body lengths per second when placed near a permanent magnet of strength 80 mT.

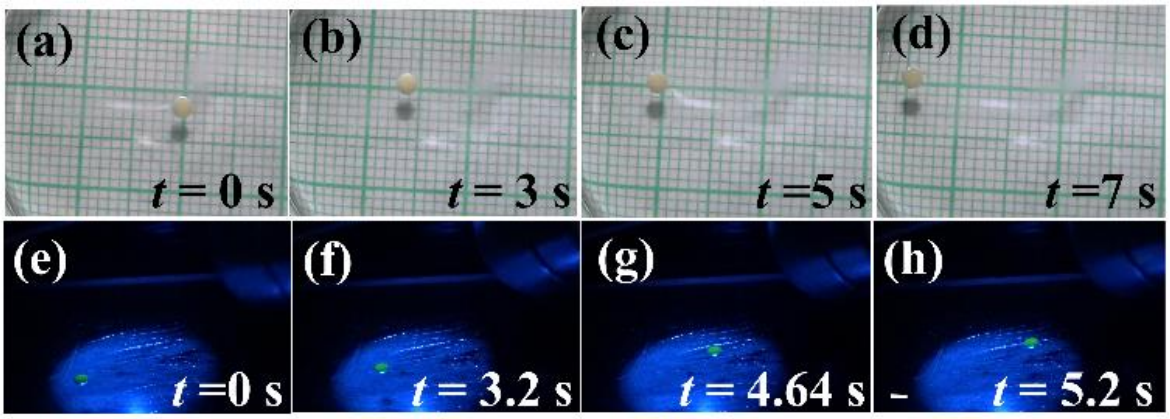

Figure 3.4. Images (a-d) show the magnetic field induced motion of a drug loaded paramagnetic waterbot at 0 s, 3 s, 5 s, and 7s, respectively, petri dish filled with chloroform and under the influence of an electromagnet of strength 148 mT. The minimum box dimension of graph was 1 mm × 1 mm. Images (e-h) show the motion of a paramagnetic waterbot tagged with a fluorescent probe under the influence of a permanent magnet of strength 80 mT. The scale bar in these images represents 1 mm.

Figure 3.4 (a-d) show that an opaque paramagnetic waterbot loaded with paracetamol drug (0.5M) was pulled by a magnet on a chloroform bath at a maximum speed of 2 mm/s. In such a situation, the fluorescent tracer provided an optical indication of the local position of the motile droplet, as shown in the Figure

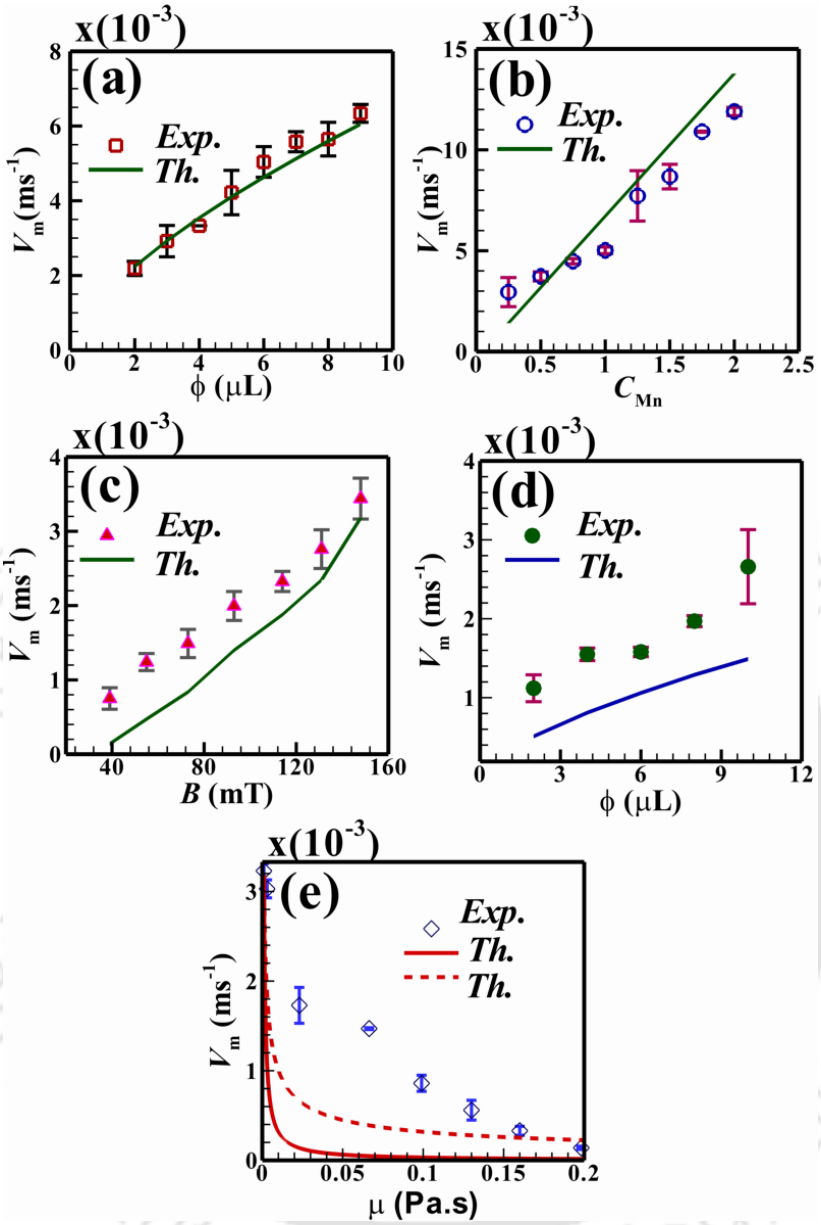

Figure 3.5. Plot (a) shows the variation in the average velocity (V_m) of paramagnetic waterbot with its volume (ϕ) when the concentration of $MnCl_2$ was C_{Mn} = 0.5M, magnetic field strength was B = 148 mT, and viscosity of the waterbot and medium was, μ = 0.001 Pa.s and μ_m respectively. Plot (b) shows the variation of V_m with C_{Mn} when B = 148 mT, μ = 0.001 Pa.s, and ϕ = 5 μL. Plot (c) shows the variation in V_m with B when C_{Mn} = 0.5M, ϕ = 5 μL, and μ = 0.001 Pa.s. Plot (d) shows the variation in V_m of diamagnetic waterbot with ϕ when C_{Na} = 1 M, B = 240 mT, and μ = 0.001 Pa. Plot (e) shows the variation in V_m of paramagnetic waterbot with μ_m when C_{Mn} = 0.5 M, B = 148 mT, and ϕ = 5 μL. The symbols (solid lines) represent experiments (theoretical prediction).

3.4 (e-h). Figures 3.1–3.3 together showed diverse pull-push migrations of the waterbots, which can be of importance for in-vivo applications of the proposed liquibots.

The magnetic force exerted on the waterbot could be evaluated from the expression, $F_m = V(\Delta\chi/\eta)\mathbf{B}\cdot\nabla\mathbf{B}$, [44-45] in which ∇ was the gradient operator, **B** was the magnetic field vector, V was the volume of the droplet, $\Delta\chi = \chi_p^M C + \chi_w^V$ was the difference in the magnetic susceptibility where χ_p^M and χ_w^V are the molar and volume susceptibilities of salt and water, C was the concentration of the salt, and η was the magnetic susceptibility of vacuum ($4\pi \times 10^{-7}$).

The theoretical average velocity of the droplet could be obtained by applying the Newton's second law of motion ($F_m + F_d = ma$) in which the drag force on the droplet was evaluated by the Stokes formula, $F_d = 6\pi\mu r v$ [46]. Where m and a were the mass and acceleration of the droplet, μ was the viscosity of the bounding medium, r was the radius of the droplet, and v was the average velocity of the droplet.

We measured the time to traverse 1 cm in order to obtain the experimental average velocity of the liquibots. Further, to evaluate the theoretical average velocity we enforced Newton's 2nd law in the Stokes flow limit, $F_m + F_d = 0$, which provided the expression for theoretical velocity of the droplet as, $v = \left[\left(2r^2\Delta\chi\right)/\left(9\mu\right)\eta\right]\mathbf{B}\cdot\nabla\mathbf{B}$. For a unidirectional magnetic field the expression could further simplify into the form, $v = \left[\left(2r^2\Delta\chi\right)/\left(9\eta\mu\right)\right]B_x\left(\partial B_x/\partial x\right)$, where x is the direction of the movement of the liquibot. Plots (a) – (d) in the Figure 3.5 show a comparison between the average

velocities (V_m) obtained from the theoretical calculations (solid line) and the experiments (symbols) with the variations in the volume of the paramagnetic droplet (ϕ), paramagnetic salt concentration (C_{Mn}), magnetic field strength (B), and volume of the diamagnetic droplet (ϕ). Table 3.1 shows the typical properties employed for the calculations in the present manuscript:

Table 3.1. Physical properties of fluid in the experiments [47-50]

μ (Pa s)	ρ (kg/m^3)	Mw ($MnCl_2.4H_2O$)	χ^M_{Mn} (m^3.mol^{-1})	χ^M_{Na} (m^3.mol^{-1})	χ^V_W
0.001	1000	198	1.8×10^{-4}	30×10^{-6}	9×10^{-6}

The plots (a) – (c) suggest that V_m monotonically increased with the increase in ϕ, C_{Mn}, and B. Interestingly, the proposed theoretical model could not only predict the trend of the variations in V_m with ϕ, C_{Mn}, and B but also quantitatively corroborated the experimentally measured values. The V_m attained by a 2 µl paramagnetic waterbot was ~2.19 × 10^{-3} ms^{-1}, which increased to ~ 6.34 × 10^{-3} ms^{-1} for a ~9 µl waterbot. Further, a waterbot containing 2M $MnCl_2$ showed a speed as high as 11.9 × 10^{-3} ms^{-1} when the applied field strength was 148 mT. Increase in volume, salt loading, and magnetic field strength led to the manifestation of larger amount of magnetic body force on the waterbot. Plot (d) shows that even for a diamagnetic waterbot V_m monotonically increased with ϕ. We also observed (not reported here) that V_m increased with the NaCl loading (C_{Na}) inside the droplet. The V_m attained by the liquid motor was ~1.36 × 10^{-3} ms^{-1} when C_{Na} ~1 M and B was 240 mT. However, with the increase in C_{Na} to ~5 M, V_m increased ~1.95 × 10^{-3} ms^{-1}. Further, with increase in ϕ, V_m increased to ~2.66 × 10^{-3} ms^{-1} for a ~10 µl waterbot. The plot (d) showed that diamagnetic waterbots could also be pushed strongly with the help of remote magnetic guidance inside a fluidic environment, which was also in

well accordance with the theoretically predicted average velocity. Plot (e) showed the for influence of droplet motion for different viscosity of the medium. When we increase the viscosity of the system, velocity of the droplet decrease and droplet does not show the motion at viscosity (> 0.2 Pa.s) for given magnetic field. This is happening that viscous force dominate to stop the waterbot. The difference in the magnitude of the values in the experiments and the theoretical predictions could be bridged through a more rigorous analysis of the force balance equations, which was kept as a future scope of research work.

Apart from the waterbots, we also prepared emulsion based oilbots where a 1 M aqueous $MnCl_2$ solution was mixed with commercially available paracetamol before shaken vigorously with oleic acid at different volumetric proportions. The drug and the paramagnetic salt were initially loaded in the water phase and then the drug loaded waterbots were dispersed through shaking inside oleic acid to prepare the oilbots. Figure 3.6 (a) schematically shows the transport and release of the drug loaded waterbots from the oilbots under magnetic guidance. The optical image shows the dispersion of waterbots in the oil matrix. Images 3.6 (b–e) show motion of the drug-loaded oilbot with the help of permanent magnet (80 mT) in a water bath. The images and video show the transport of the oilbot loaded with the drug embedded waterbots under the remote magnetic guidance before the release of the drug ~16.9 s in the bath. The plot (f) shows that the average velocity (V_m) of these oilbots could be modulated by tuning the salt loading in the waterbots. The plot (g) suggests that the time for drug release (t_r) could also be controlled by tuning the water to oil loading in the oilbot. In particular, dispersing lower amount of water into the oil-phase showed a larger time of release under these conditions. Concisely,

Figure 3.6 suggest that an emulsion of paramagnetic waterbots in oil can be employed for drug transport and delivery under magnetic guidance. The drug loaded paramagnetic waterbots having dimensions of few microns to few hundred microns dispersed inside the oilbots could act as in-vivo transporters of drugs in diverse body fluids [51-52] such as blood stream, cerebrospinal fluid, mucus, lymph, bile, saliva, tear, or extracellular fluids.

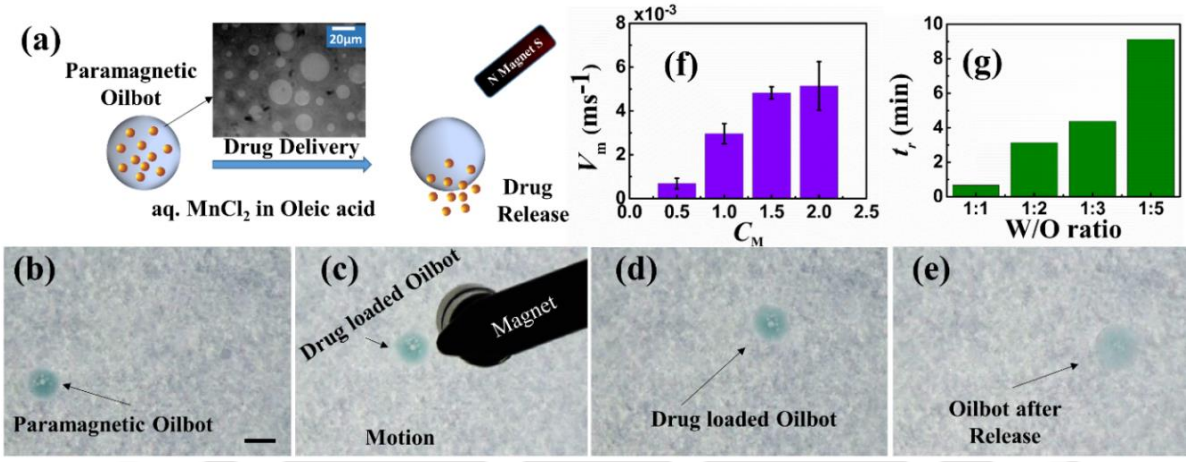

Figure 3.6. Image (a) shows the schematic representation of transport, delivery, and release of an oilbot having dispersed paramagnetic waterbots trapped in a continuous oil phase. The grayscale optical micrograph shows the typical dispersion of microscale waterbots in the oil matrix. Images (b–e) show the magnetic field induced motion of an oilbot loaded with paracetamol drug at 0 s, 3 s, 5.8 s, and 16.9 s, respectively, and subsequent release of the drug when ϕ = 10 μL and B = 80 mT. The scale bar in the image represents 2.5 mm. Plot (f) shows the variation in V_m of the oilbot with the salt loading in the water phase (C_M) when ϕ = 5 μL and B = 240 mT. Plot (g) shows the time of release of the waterbots (t_r) for different water to oil ratios, respectively.

A typical phase separation experiment of oleic acid and water shown in the Figure 3.7 supported the observations of the release in the Figure 3.6. In the beginning of this experiment, different water-in-oil emulsions were prepared by mixing 1M aqueous $MnCl_2$ with oleic acid through adequate shaking at proportions (v/v), 1:1,

1:2, 1:3 and 1:5, as shown in the rows (a) and (b). The images (c) show that the 1:1, 1:2, 1:3 and 1:5 emulsions phase separated at different time intervals 0.67, 3.12, 4.37, and 9.12 min, respectively.

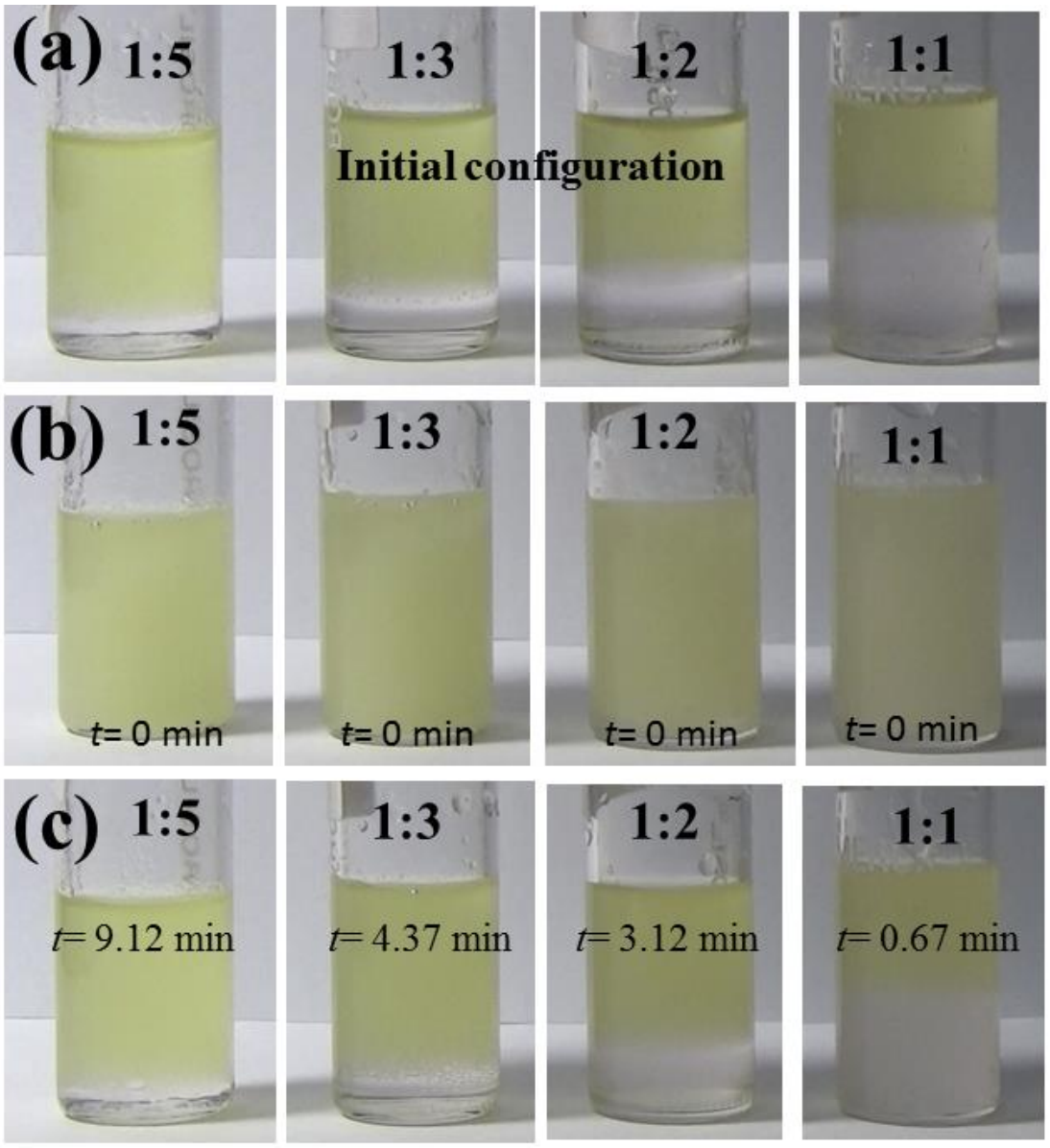

Figure 3.7. Preparation of water-in-oil (W/O) emulsions (v/v) of water (transparent) and oleic acid (pale yellow). Row (a) showing the images of different initial volumes in the vials having W/O ratios of, 1:1, 1:2, 1:3, and 1:5, respectively. Row (b) shows the situation of the same vials after vigorously shaking for 5 min. Row **(c)** shows the vials after, 0.67, 3.12, 4.37, and 9.12 min when complete phase separation took place.

It may be noted here that the use of surfactants or surface active agents in these experiments could further help in modulating the time for mixing and phase separation. The experiment indicated that the release mechanisms of the oilbots could efficiently be designed by tuning the t_r of these emulsions to ensure targeted release at stipulated time.

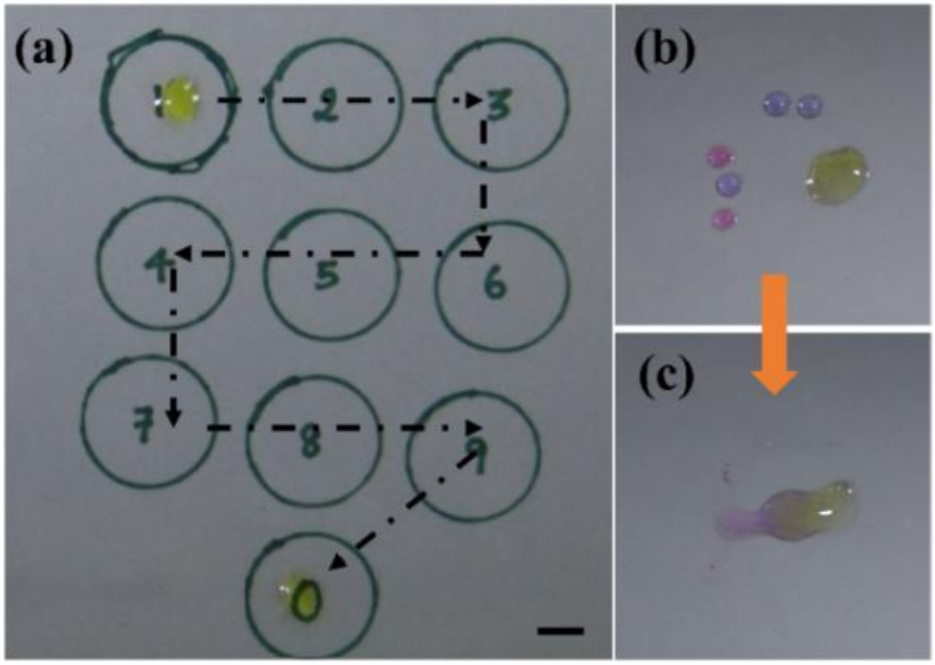

Figure 3.8. Controlled migration of $FeCl_3$ loaded paramagnetic waterbots. Image **(a)** shows the intricate movement represented by the broken line representing telephone dialling when, ϕ = 5 µl, C_{Fe} = 2M, B = 80 mT, and μ = 0.001 Pa s. The scale bar in the image represents 5 mm. Images **(b)** and **(c)** show magnetic field induced merging of waterbots emulating the 'Packman'TM game, when, C_{Fe} = 2M, B = 80 mT, and μ = 0.001 Pa s.

Remarkably, apart from the facile movement inside the liquid mediums, the waterbots could also show controlled migration on the solid surfaces coated with thin oil layer, as shown in the Figure 3.8 (a). In this case, initially dialling patterns were drawn on a white paper with the help of a pen and then covered by a

transparent plastic sheet. Following this, the transparent sheet was coated with a thin layer of oleic acid to reduce the surface friction before dispensing $FeCl_3$ loaded paramagnetic waterbots. The camera recorded the motion from the top while the magnetic control was offered from the bottom of the paper surface. The magnet was not visible in the figures or video because it was masked by the opaque paper surface. The broken line on the image shows the migration path of the waterbot with the remote magnetic guidance on the solid surface. Using a similar setup, we performed the experiments shown in the Figure 3.8 (b-c), which show that the smaller waterbots from different corners could be merged and coalesced into a bigger one emulating the popular 'Packman'^{TM} game on a solid surface.

Figure 3.9 show that a paramagnetic waterbot (C_{Fe}, 2M aqueous $FeCl_3$) could be split into multiple droplets with the remote guidance of the magnet. Again, in this experiment, a paper was initially coated with a transparent sheet before a thin layer of oleic acid was coated on it to reduce the friction of the waterbot dispensed on it. The magnet was placed underneath the surface while the camera recorded the motion from the top. The movement of the magnet pulled the paramagnetic waterbot towards it against the surface friction on the slippery surface, which caused the splitting of the waterbot into parts.

Image (b–g) show the splitting of a parent waterbot into 2 – 7 daughters and then ordering them in the shape of a line, triangle, pentagon, hexagon, and heptagon, respectively. A very recent work had shown similar happenings with a droplet composed of ferrofluid [31]. Here we could achieve analogous findings employing a much simpler, non-toxic, and transparent system in place.

In the present case, the paramagnetic waterbots behaved like a magnet under the influence of magnetic field, which underwent cohesive failure due to viscous stress at the droplet-oil interface [53] to cause splitting while moving under the magnetic guidance on a slippery solid surface coated with a thin oil layer.

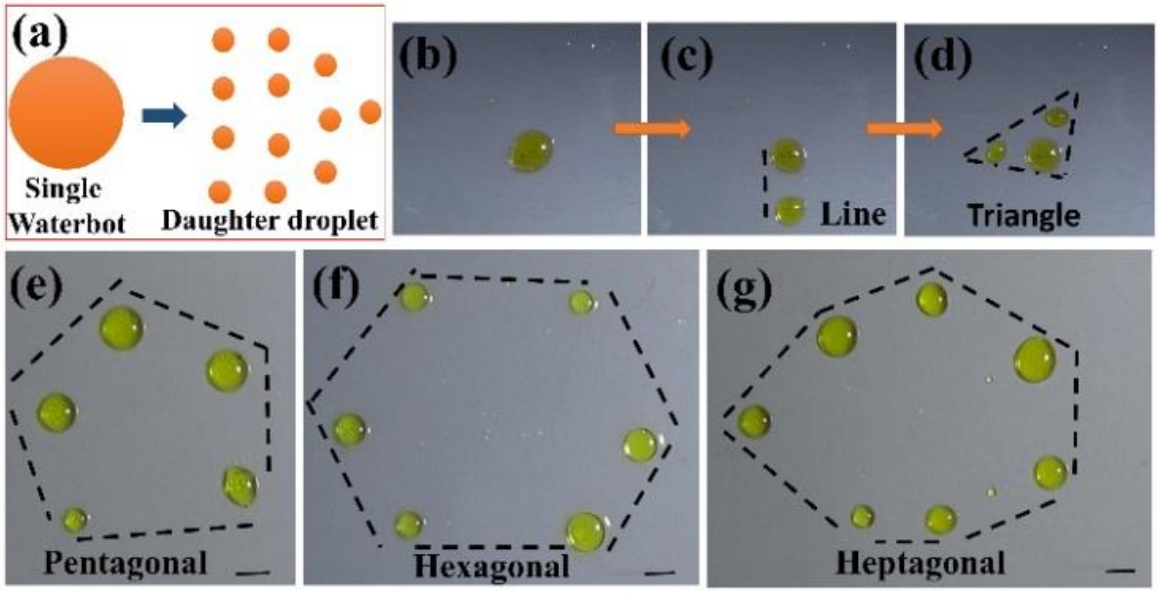

Figure 3.9. Droplet splitting phenomena. Image (a) shows a schematic diagram of breaking a single waterbot into many and simultaneously ordering them. Images (b-g) show the stage wise splitting of a single $FeCl_3$ waterbot into 2 – 7 droplets and then ordering them in the shape of a line, triangle, pentagon, hexagon, and heptagon, respectively. Here C_{Fe} = 2M, B = 80 mT, and μ = 0.001 Pa s. The scale bar shown here is 5 mm.

The magnetically guided droplet actuation shown in the Figure 3.7 and 3.8 had various advantages in the domain of droplet microfluidics over the previously reported methodologies, which employ the electric field as the driving force [32,33]. For example, (a) the electrically modulated migrations required high intensity AC or DC fields while the proposed methodology suggested the use of magnets for similar operations; (b) the embedded electrical circuits for electrically

actuated drop migration were labile to intense heat generation, which could be avoided employing the proposed methodology; (c) the embedded electrical circuit for the electric field induced motions required complex surface patterning of electrodes employing costly fabrications methodologies. In comparison, the proposed methodology was simple to operate, devoid of the problems associated with heat generation, independent of any circuitry, and did not demand any costly fabrication technique for preparation.

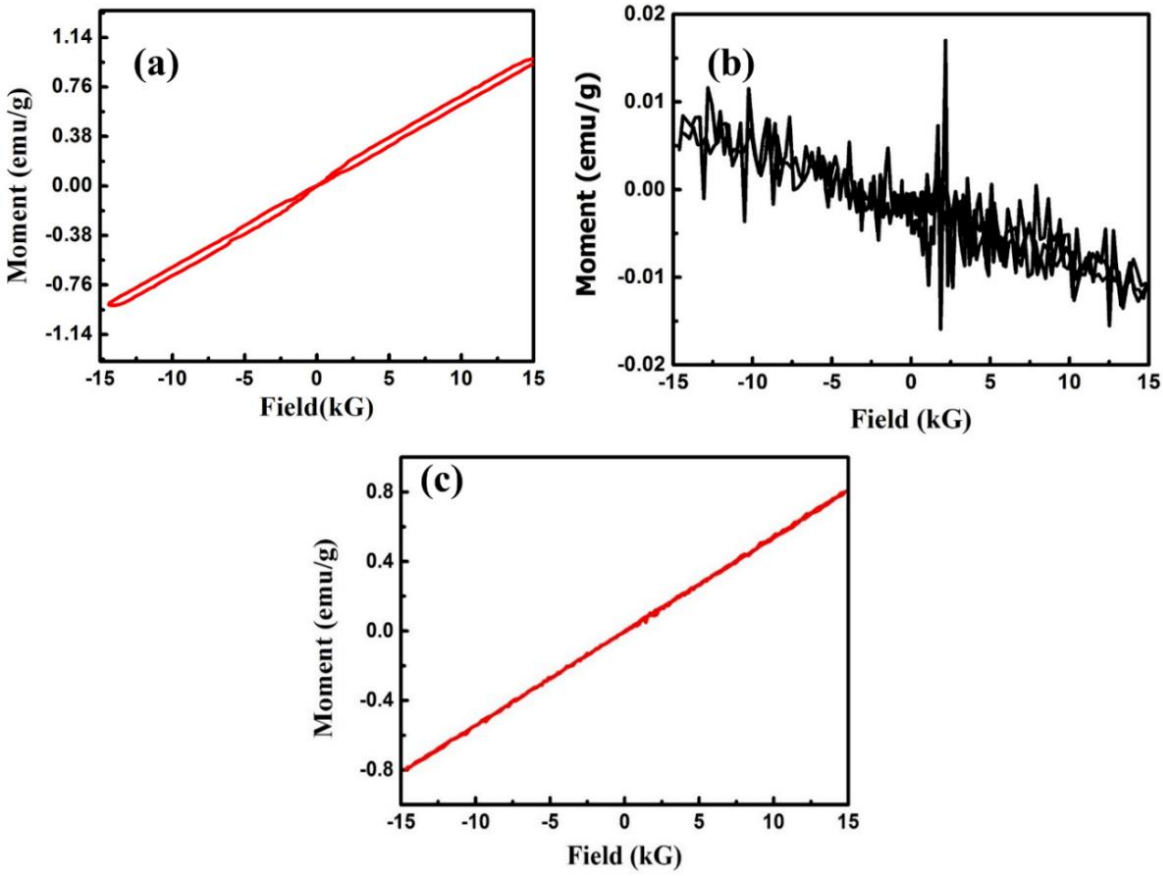

Figure 3.10. Vibrating sample magnetometry (VSM) hysteresis loop for the aqueous solutions of (a) $MnCl_2$, (b) NaCl, and (c) $FeCl_3$.

The magnetization curve for the paramagnetic and diamagnetic liquidbots were obtained from the VSM data at 25°C by varying the magnetic field from −15 to 15 kG. The magnetization curves in Figure 3.10 (a) show that the liquidbot loaded with

manganese (II) chloride was highly paramagnetic. The magnetization curves in Figure 3.10 (b) show that liquidbot loaded with sodium chloride was diamagnetic in nature. The other paramagnetic salt $FeCl_3$ also showed paramagnetic behavior when loaded inside the liquidbot, Figures 3.10 (c).

3.4 SUMMARY

In summary, we demonstrated attractive (repulsive) motions of paramagnetic (diamagnetic) salt laden liquibots under remote magnetic guidance. The non-toxic oilbots or waterbots were prepared employing simple methodologies in which either the salt was dissolved in water or the salt laden water medium was emulsified in oil. This is in stark contrast to the preparation of the previously reported nano-enabled solid or soft-solid self-propellers, which required the involvement of costly and complex fabrication mythologies [54]. The proposed waterbot was devoid of any phase-separation during its migration whereas the oilbots showed a tuneable phase-separation suitable for delivery of commercial drugs like Doxorubicin, Lopressor drug, Efavirenz for cancer treatment, multiple cardiovascular drug for heart related problem and HIV antiviral [55-57]. The paramagnetic (diamagnetic) waterbot could migrate, ~8 body length/s (~ 1 body length/s) under remote magnetic guidance, which could further be increased by enhancing the strength of the external magnetic field. Facile controls on the direction and speed of the motions were shown by varying the size and salt loading. The drug loaded water or oilbots could be envisioned as future *in vivo* transporters of drugs inside diverse body fluids such as blood stream, cerebrospinal fluid, mucus, lymph, bile, tear, mucus, or extracellular fluids [51-52]. In addition, the waterbot was split into many smaller parts on an oil

coated solid surface and then arranged in the shapes of polygons. A liquibot based 'Packman'™ game was also demonstrated where the bots moved on the slippery solid surfaces under the magnetic guidance. The experiments pointed the suitability of the proposed liquibots in diverse droplet microfluidic applications.

REFERENCES

1. V. Taly, D. Pekin, A. E. Abed and P. Laurent-Puig, *Trends Mole. Med.*, 2012, **18**, 405-416.
2. K. Pataky, T. Braschler, A. Negro, P. Renaud, M. P. Lutolf and J. Brugger, *Adv. Mater.*, 2012, **24**, 391-396.
3. S. Juul, C. J. F. Nielsen, R. Labouriau, A. Roy, C. Tesauro, P. W. Jensen, C. Harmsen, E. L. Kristoffersen, Y.-L. Chiu, R. Frøhlich, P. Fiorani, J. Cox-Singh, D. Tordrup, J. Koch, A.-L. Bienvenu, A. Desideri, S. Picot, E. Petersen, K. W. Leong, Y.-P. Ho, M. Stougaard and B. R. Knudsen, *ACS Nano*, 2012, **6**, 10676-10683.
4. R. Dong, J. Li, I. Rozen, B. Ezhilan, T. Xu, C. Christianson, W. Gao, D. Saintillan, B. Ren and J. Wang, *Sci. Rep.*, 2015, **5**, 13226, 1-7.
5. L. Florea, K. Wagner, P. Wagner, G. G. Wallace, F. Benito-Lopez, D. L. Officer and D. Diamond, *Adv. Mater.*, 2014, **26**, 7339-7345.
6. K. K. Dey, X. Zhao, B. M. Tansi, W. J. Méndez-Ortiz, U. M. Cordova-Figueroa, R. Golestanian and A. Sen, *Nano Letters*, 2015, **15**, 8311-8315.
7. M. Kiristi, V. V. Singh, B. Esteban-Fernández de Ávila, M. Uygun, F. Soto, D. A. Uygun and J. Wang, *ACS Nano*, 2015, **9**, 9252-9259.
8. S. Sengupta, D. Patra, I. Ortiz-Rivera, A. Agrawal, S. Shklyaev, K. K. Dey, U. Córdova-Figueroa, T. E. Mallouk and A. Sen, *Nat. Chem.*, 2014, **6**, 415-422.
9. M. Manjare, F. Yang, R. Qiao and Y. Zhao, *J. Phys. Chem. C*, 2015, **119**, 28361-28367.
10. M. K. Chaudhury and G. M. Whitesides, *Science*, 1992, **256**, 1539-1541.
11. J. Cejkova, M. Novák, F. Stepanek, and M. M. Hanczyc, *Langmuir*, 2014, **30**, 11937-11944.
12. N. Miljkovic, D. J. Preston, R. Enright, and E. N. Wang, *Nat. Commun.*, 2013, **4**, 1-9.

13. A. Diguet, R.-M. Guillermic, N. Magome, A. Saint-Jalmes, Y. Chen, K. Yoshikawa and D. Baigl, *Angew. Chem. Inter. Ed.*, 2009, **48**, 9281-9284.
14. Y. N. Cheung, N. T. Nguyen and T. N. Wong, *Soft Matter*, 2014, **10**, 8122-8132.
15. R. S. M. Rikken, R. J. M. Nolte, J. C. Maan, J. C. M. van Hest, D. A. Wilson, and P. C. M. Christianen, *Soft Matter*, 2014, **10**, 1295-1308.
16. A. K. Singh, K. K. Dey, A. Chattopadhyay, T. K. Mandal, and D. Bandyopadhyay, *Nanoscale*, 2014, **6**, 1398-1405.
17. H. Wang and M. Pumera, *Chem. Rev.*, 2015, **115**, 8704-8735.
18. R. Laocharoensuk, J. Burdick and J. Wang, *ACS Nano*, 2008, **2**, 1069-1075.
19. S. Palagi, A. G. Mark, S. Y. Reigh, K. Melde, T. Qiu, H. Zeng, C. Parmeggiani, D. Martella, A. Sanchez-Castillo, N. Kapernaum, F. Giesselmann, D. S. Wiersma, E. Lauga, and P. Fischer, *Nat. Mater.*, 2016, **15**, 647-654.
20. O. D. Velev, B. G. Prevo, and K. H. Bhatt, *Nature*, 2003, **426**, 515-516.
21. J. Yin, X. Li, J. Yu, Z. Zhang, J. Zhou, and W. Guo, *Nat. Nano*, 2014, **9**, 378-383.
22. G. Katsikis, J. S. Cybulski, and M. Prakash, *Nat. Phys.*, 2015, **11**, 588-596.
23. C. T. Yavuz, J. T. Mayo, W. W. Yu, A. Prakash, J. C. Falkner, S. Yean, L. Cong, H. J. Shipley, A. Kan, M. Tomson, D. Natelson, and V. L. Colvin, *Science*, 2006, **314**, 964-967.
24. D. Heinrich, A. R. Goni, T. M. Osan, L. M. C. Cerioni, A. Smessaert, S. H. L. Klapp, J. Faraudo, D. J. Pusiol, and C. Thomsen, *Soft Matter*, 2015, **11**, 7606-7616.
25. Y. Zhang, D. J. Shin, and T. H. Wang, *Lab Chip*, 2013, **13**, 4827-4831.
26. S. Laurent, D. Forge, M. Port, A. Roch, C. Robic, L. Vander Elst, and R. N. Muller, *Chem. Rev.*, 2008, **108**, 2064-2110.
27. J. Jeong, E. Um, J.-K. Park, and M. W. Kim, *RSC Adv.*, 2013, **3**, 11801-11806.
28. K. A. Mirica, S. T. Phillips, C. R. Mace, and G. M. Whitesides, *J. Agric. Food Chemi.*, 2010, **58**, 6565-6569.
29. K. S. Khalil, S. R. Mahmoudi, N. Abu-dheir, and K. K. Varanasi, *Appl. Phys. Lett.*, 2014, **105**, 041604:1-4.
30. D. K. Bwambok, M. M. Thuo, M. B. J. Atkinson, K. A. Mirica, N. D. Shapiro, and G. M. Whitesides, *Anal. Chem.*, 2013, **85**, 8442-8447.
31. J. V. I. Timonen, M. Latikka, L. Leibler, R. H. A. Ras, and O. Ikkala, *Science*, 2013, **341**, 253-257.

32. R. Dey, U. U. Ghosh, S. Chakraborty, and S. DasGupta, *Langmuir*, 2015, **31**, 11269-11278.

33. A. R. Wheeler, *Science*, 2008, **322**, 539-540.

34. B. Nie, S. Xing, J. D. Brandt, and T. Pan, *Lab Chip*, 2012, **12**, 1110-1118.

35. M. Bhattacharjee, V. Pasumarthi, J. Chaudhuri, A. K. Singh, H. Nemade, and D. Bandyopadhyay, *Nanoscale*, 2016, **8**, 6118-6128.

36. S. Sattayasamitsathit, H. Kou, W. Gao, W. Thavarajah, K. Kaufmann, L. Zhang, and J. Wang, *Small*, 2014, **10**, 2830-2833.

37. Y. Wu, X. Lin, Z. Wu, H. Mohwald, and Q. He, *ACS Appl. Mater. Interfaces*, 2014, **6**, 10476-10481.

38. S. S. Banerjee, A. Jalota-Badhwar, K. R. Zope, K. J. Todkar, R. R. Mascarenhas, G. P. Chate, G. V. Khutale, A. Bharde, M. Calderon, and J. J. Khandare, *Nanoscale*, 2015, **7**, 8684-8688.

39. T. H. Seah, G. Zhao, and M. Pumera, *ChemPlusChem*, 2013, **78**, 395-397.

40. P. Dubois, G. Marchand, Y. Fouillet, J. Berthier, T. Douki, F. Hassine, S. Gmouh and M. Vaultier, *Anal. Chem.*, 2006, **78**, 4909-4917.

41. L.-H. Hung, K. M. Choi, W.-Y. Tseng, Y.-C. Tan, K. J. Shea and A. P. Lee, *Lab Chip*, 2006, **6**, 174-178.

42. Y. Sheng, G. Sun, J. Wu, G. Ma and T. Ngai, *Angew. Chem.*, 2015, **127**, 7118-7123.

43. S. C. C. Shih, N. S. Mufti, M. D. Chamberlain, J. Kim, and A. R. Wheeler, *Energ. Environ. Sci.*, 2014, **7**, 2366-2375.

44. S. S. Shevkoplyas, A. C. Siegel, R. M. Westervelt, M. G. Prentiss, and G. M. Whitesides, *Lab Chip*, 2007, **7**, 1294-1302.

45. N. Pamme, *Lab Chip*, 2006, **6**, 24-38.

46. S. Kumar, A. K. Singh, A. K. Dasmahapatra, T. K. Mandal, and D. Bandyopadhyay, *Carbon*, 2015, **89**, 31-40.

47. Landolt-Börnstein, Numerical Data and Functional Relationships in Science and Technology, New Series, II/16, Diamagnetic Susceptibility, Springer-Verlag, Heidelberg, 1986.

48. Landolt-Börnstein, Numerical Data and Functional Relationships in Science and Technology, New Series, III/19, Subvolumes a to i2, Magnetic Properties of Metals, Springer-Verlag, Heidelberg, 1986-1992.

49. Landolt-Börnstein, Numerical Data and Functional Relationships in Science and Technology, New Series, II/2, II/8, II/10, II/11, and II/12a, Coordination and Organometallic Transition Metal Compounds, Springer-Verlag, Heidelberg, 1966-1984.
50. Tables de Constantes et Données Numérique, Volume 7, Relaxation Paramagnetique, Masson, Paris, 1957
51. J. R. Baylis, J. H. Yeon, M. H. Thomson, A. Kazerooni, X. Wang, A. E. St. John, E. B. Lim, D. Chien, A. Lee, J. Q. Zhang, J. M. Piret, L. S. Machan, T. F. Burke, N. J. White, and C. J. Kastrup, *Sci. Adv.*, 2015, **1**,1-8.
52. G. Zhao, M. Viehrig, and M. Pumera, *Lab Chip*, 2013, **13**, 1930-1936.
53. Z. Li, A. M. Leshansky, L. M. Pismen, and P. Tabeling, *Lab Chip*, 2015, **15**, 1023-1031.
54. Y. Xia, and G.M. Whitesides, *Angew. Chem. Int. Ed*., 1998, **37,** 550–575.
55. S. Kalepu, M. Manthina and V. Padavala, *Acta Pharm. Sin. B*, 2013, **3**, 361-372.
56. W. L. Lee, P. Wee, C. Nugraha and S. C. J. Loo, *J. Mater. Chem. B*, 2013, **1**, 1090-1095.
57. C. W. Pouton, *Eur. J. Pharm. Sci.*, 2006, **29**, 278-287.

Chapter 4

Electric Field Induced Spreading, Oscillation, Ejection, and Spinning of Oilbots

4.1. INTRODUCTION

Electrowetting of a liquid droplet on a homogeneous solid surface under the influence of an externally applied electric field has fascinated the researchers for ages [1-3]. Lippmann was among the pioneers to identify the physics behind this process through his seminal contribution on the theory of electrocapillarity [1]. The formulation uncovered the reasons behind the capillary depression of mercury when in contact with electrolyte solutions in presence of an external electric field4. Later, interesting behaviours of the electrically conducting liquid droplets on different types of surfaces under the influence of alternating (AC) or direct (DC) current electric fields were explored [5-7]. Much later, Taylor [3] unveiled the role of electro-hydrodynamic (EHD) stresses originating from the accumulation of the induced charges at the droplet-substrate interface as the major reason behind the change in the equilibrium contact angle of the liquid droplet during electrowetting (EW). The term 'electrowetting' was coined much later by Beni and Hackwood while they employed this phenomenon to design display devices8. A number of review articles have been written over the years to summarize the scientific and technological progresses of diverse EW processes [9-12].

In recent times, the EW process has been employed as a model prototype to study the field induced deformation or actuation of soft and deformable microsystems [13-16]. However, after the invention, for a long period the applicability of the EW processes were rather limited because the droplets composed of electrolytes were placed on one of the electrodes, which caused electrolysis [17]. The utility of the EW processes escalated only after the introduction of the concept of electrowetting on dielectric (EWOD) materials [18]. The EWOD setup proposed the placement of the droplet on a hydrophobic insulating isolator which in turn was placed on the electrode substrate19. In a typical EWOD setup

the electric field was applied through an external circuit in which the bottom substrate acted as one of the electrodes while an electrically conducting wire touching the droplet from the top acted as the other electrode. The placement of the thin hydrophobic isolator between the droplet and the substrate electrode at the bottom in the EWOD setup helped in, (i) arresting the electrolysis, (ii) making the process reversible, (iii) developing enough EHD stresses [20-23] for rapid EW, and (v) tuning the electrical, thermal, and surface properties of the isolator to develop a wide range of applications.

In the recent past, the EW processes have been employed for microscale mixing24, reaction engineering [25], energy harvesting [26-27], droplet actuation [28-29], electronic displays [30], biomedical engineering [31,32], bio-MEMS devices [33], and droplet or digital microfluidics [34-36], among others. In particular, the hydrodynamic, elastic, and interfacial properties of the isolator was found to markedly influence the electro-capillarity of the droplet. For example, while the superhydrophobic isolators composed nanowires or nanorods showed a reversible EW [37-42], an inverse EW process of a large number of microdroplets could harvest high density power [43] by converting mechanical energy into the electrical one [44]. Interestingly, a number of recent works have shown that the energy storage and dissipation at the three-phase contact line of the advancing front of a microdroplet undergoing EW could provide additional control over the EW behavior [45-47]. Requirement of ultra-low voltages have shown the pathways to develop energy efficient EW processes [47]. In particular, the elasto-capillary effects at the soft and deformable isolators or viscous dissipation on the liquid isolators could develop EW processes having reversible to transient responses important for various optoelectronic applications [48,49]. In this direction, the EW of a microdroplet on strongly slipping

surface can be one interesting system where the contact-line may show interesting motions, which is yet to be explored in detail.

4.2. EXPERIMENTAL SECTION

4.2.1. Materials

We purchased Cu and double sided tapes from local venders. The oil hexadecane ($C_{16}H_{34}$) was purchased from the Sigma Aldrich, India, oleic acid ($C_{18}H_{34}O_2$) was purchased from the Merck, India, iodine was purchased from the SRL India, and silicon oil was purchased from the Loba Chemie Pvt. Ltd., India. Platinum (Pt) wires of length 2.5 cm and diameter 150 µm were procured from Surgeon Sons, India. Polydimethylsiloxane (PDMS) was purchased from Dow Corning, India (SYLGARD® 184 kit), and polytetrafluoroethylene (PTFE) was purchased from Nastro Professionale Tenuta Filetti. Deionized water (DI, Merck Millipore, grade I) was used for all the experiments. Rectangular rare earth Neodymium magnets (N52) of known strength and dimension 40 mm × 25 mm × 10 mm were purchased online.

4.2.2. Methods

The EWOL setup was fabricated on a plain glass plate. A reservoir of dimension (1.5 cm × 6 cm × 0.2 cm) was made with double sided tapes and in the middle of the reservoir a copper tape having thickness of ~ 160 µm was pasted on the glass plate to prepare the anode. The bottom of the reservoir along with the copper tape was covered with a PTFE isolator layer of thickness ~160 µm to avoid electrolysis. Then the reservoir was filled with water, as schematically shown in the Figure 1 (a). The oil droplets (silicon oil, hexadecane, or oleic acid) of size varying from 0.5 - 5 µl were dispensed on the water bath before a Pt cathode of 150 µm diameter was connected to the oil droplet from the top. The

electrodes were connected to a DC Power source (SES Instruments Pvt. Ltd., range: 0 – 1500 V) to supply electric field. For the magnetic field experiments, the EWOL setup on the Neodymium magnets in a such a manner that a Lorentz force could rotate the oil droplet, as schematically shown in the Figure 1 (d).

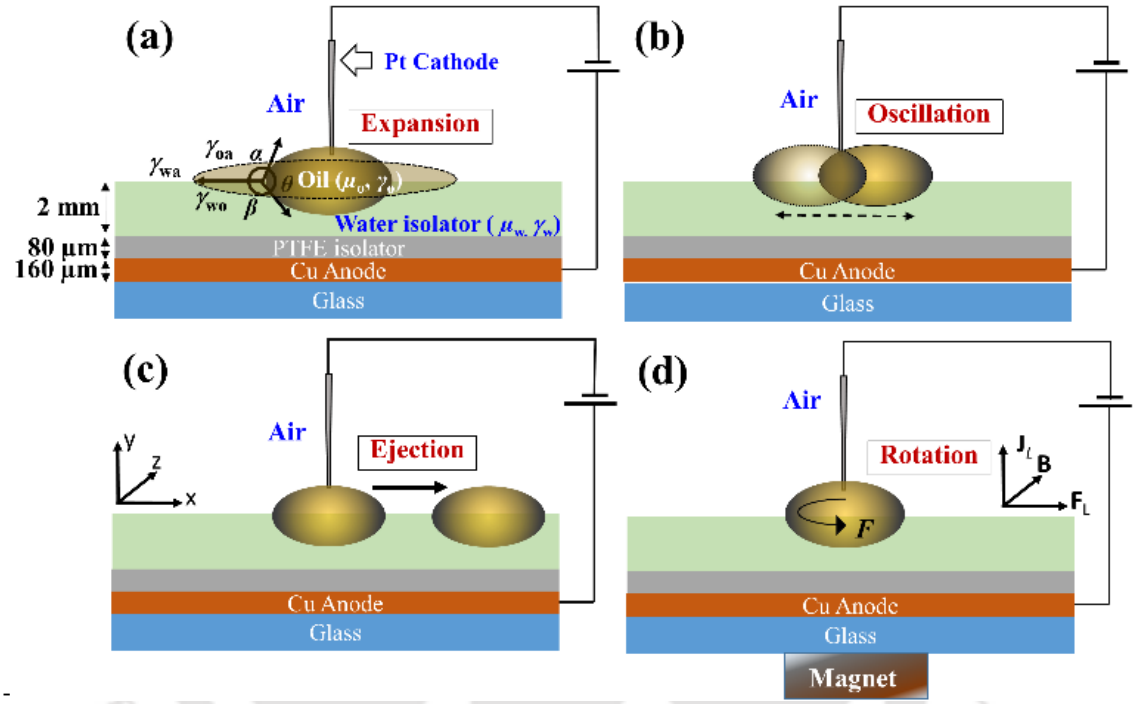

Figure 4.1. Images (a) – (d) schematically show the EWOL experimental setup employed for the droplet expansion, oscillation, ejection, and rotation, respectively. Image (a) shows a glass substrate covered with a Cu anode which in turn was coated with a dielectric polytetrafluoroethylene (PTFE) layer. A thick water (*w*) reservoir was created on PTFE before dispensing hexadecane oil (*o*) droplet on the water layer. A pointed Pt cathode was connected from the top of the oil droplet. Application of an external electric field through the electrodes led to the (a) expansion, (b) oscillation, and (c) ejection of the droplet with increasing field intensity. Image (d) shows that placing a magnet in the perpendicular to the plane of the paper led to the rotational motion of the droplet. The notations γ_{ow}, γ_{oa}, and γ_{wa} represent interfacial tensions at the oil-water, oil-air, and water-air interfaces, respectively. The notations μ_o, and μ_w denote the viscosity of the oil and water and α, β, and θ represent contact angles.

The resistance or the flow of current across the EWOL system was measured with the help of a digital multimeter (Mastech India, range: 0 – 2 MΩ ± 1.0%). The droplet motion was recorded with a digital camera (Cybershot DSC-HX100v, SONY Corp. Japan). The open source imageJ software was used for the image analysis of droplet movements, oscillation, rotation, and breaking. We have measured the angle traversed by the droplet with colored glass particles for calculating the rotational speed.

Herein we show a collage of interesting motions of an oil droplet when placed on a bath of deionized (DI) water which in turn was placed on a polytetrafluoroethylene (PTFE) isolator coated on a copper (Cu) electrode. Figure 1 (a) shows the schematic diagram of the experimental setup in which the layer of DI water and the PTFE coating together formed the isolator while the electric field was applied from the top of the droplet with the help of a Platinum (Pt) cathode while the Cu substrate was made anode. In comparison to the widely employed EWOD setup [18], in the present study, we used a water column on which the oil droplet was expected to undergo EW. We termed the setup as electrowetting on liquid (EWOL) in the entire manuscript. In the EWOL setup, at lower field intensities, we observed no deformation of the droplet. However, beyond a critical field intensity, when the applied electric field could overcome the restoring surface tension and frictional forces, we observed spreading of the droplet similar to the EW processes, as shown in the Figure 1 (a). At intermediate field intensities the droplet started oscillating around the Pt electrode showing a transient phenomenon (Figure 1 (b)), and at even higher field intensities the droplet ejected to show a field induced locomotion (Figure 1(c)). The observed reversible droplet expansion and contraction of the oil droplet under the sole influence of electric field at lower field intensities and the oscillatory motion at moderately higher field intensities in the EWOL setup could be employed for micromixing of

multicomponent systems inside the microfluidic devices. The droplet ejection under the influence of a high intensity electric field was an example of an galvanotaxis and could be employed as transport and delivery of payloads inside the small scale devices.

Importantly, when the EWOL setup was placed on a permanent magnet, the droplet showed rotational motions for which the rotations could be made clockwise or anticlockwise by changing either the direction of the magnet or the electric field. It is well known that when the electric ($\mathbf{J}_L$) and the magnetic field ($\mathbf{B}$) are placed perpendicular to each other, the Lorentz force ($\mathbf{F}_L = \mathbf{J}_L \times \mathbf{B}$) [50] can be generated in the direction normal to both the fields, as shown on the Figure 4.1 (d). A number of previous studies have shown that the Lorentz force can be employed to move conducting fluids inside the microdevices [51-53], to develop micropumps [54-59] or mixers [60-63], and rotate solid particles [64]. In the present study, we showed that a viscous and incompressible oil droplet could easily be rotated with the help of Lorentz force, which could be employed as a rotor to develop an electro-magneto-hydrodynamic (EMHD) pump for microdevices. Further, simple theoretical formulations were proposed to explain the EHD and Lorentz force induced motions of the oil droplet in the EWOL setup.

Table 4.1: Physical properties of the experimental materials and fluid [65-71]

Properties		**Water**	**Teflon**	**Silicon oil**	**Oleic acid**	**Hexadecane**
Dielectric constant	ε	80	2	2.5	2.5	2.1
Surface tension (mN/m)	γ	72	-	21	42	27
Interfacial tension (mN/m)		-	-	24	64	52
Density (kg/m^3)	ρ	1000	-	971	895	770
Viscosity (Pa s)	μ	0.001	-	0.33	0.027	0.003
Conductivity (μS/m)	σ	5.6	-	0.8×10^{-6}	10^{-6}	10^{-6}

4.3. RESULT AND DISCUSSION

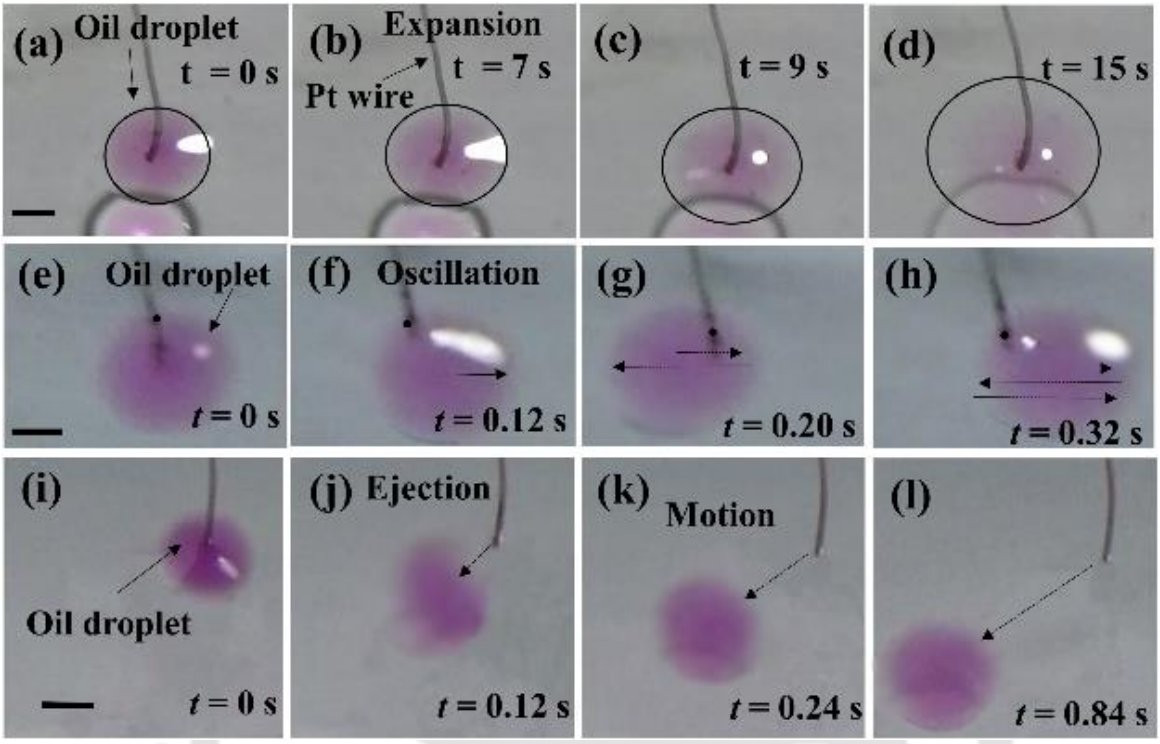

Figure 4.2. Different motions of the oil droplet under the influence of an externally applied electric field. Images (a) – (d) show the expansion of the oil droplet at different time intervals when applied potential (ψ) was 500 V. Images (e) – (h) show the oscillation of the oil droplet when ψ was 550 V and images (i) – (l) show the ejection of the oil droplet when ψ was 800 V. In these experiments the volume of the droplet (ϕ_0) was 1 µl. The scale bar shown on the images is of 2 mm. Other necessary properties are shown in the Table 4.1.

In the proposed EWOL setup the water layer was kept thicker in order to avoid electrolysis and also to nullify the increase in temperature of isolator due to Joule heating. In this situation, when the electric field was turned on, the isolator layer allowed accumulation of large amount of induced charges at the oil-water interface, which in turn generated EHD stress for the droplet motions. It may be noted here that the physics near the contact line for the proposed EWOL setup was very different from the same proposed by Lippmann-

Young for the EWOD setup, where the isolator was considered to be a solid non-deformable surface [9].

Figure 4.1 (a) shows the behaviour of the three-phase contact line of an oil droplet resting on a deformable water surface and bounded by air. The equilibrium state of the three-phase contact line in the EWOL setup could be described by the Neumann's triangle in which α, β, and θ are the angles as shown with the constrain, $\alpha + \beta + \theta = 2\pi$. When the electric field was turned on, the oil droplet was expected to expand radially to release the EHD stress developed at the oil-water and oil-air interfaces by reducing the angle, θ and increasing the circumference of the contact line.

The Figures 4.2 (a-d) show that the hexadecane oil droplet started spreading on water surface when 500 V electric field was abruptly generated. The phenomenon was found to be similar to be EWOD process where the droplet spread under the influence of the electric field. In this situation, the spreading of the droplet under electric field was a measure of EHD stress relaxation. In the proposed EWOL setup the droplet did not show spreading when the applied electric field was below 300 V because a critical field was required to overcome the surface tension force of the droplet. Figure 4.3 (a) shows the progressive increase in the diameter of the spreading droplet (D) with time (t) when the voltage was abruptly ramped up to different values ranging from 200 V to 600 V. In all these experiments the droplet was initially stationary in absence of the electric field and the videos are recorded only after abruptly ramping up the voltage to the values reported. Figures 4.2 (e-h) show that, beyond 550 V, the droplet started oscillating around the Pt electrode after the initial spreading. Figure 4.3 (b) shows the typical amplitude (L) of the

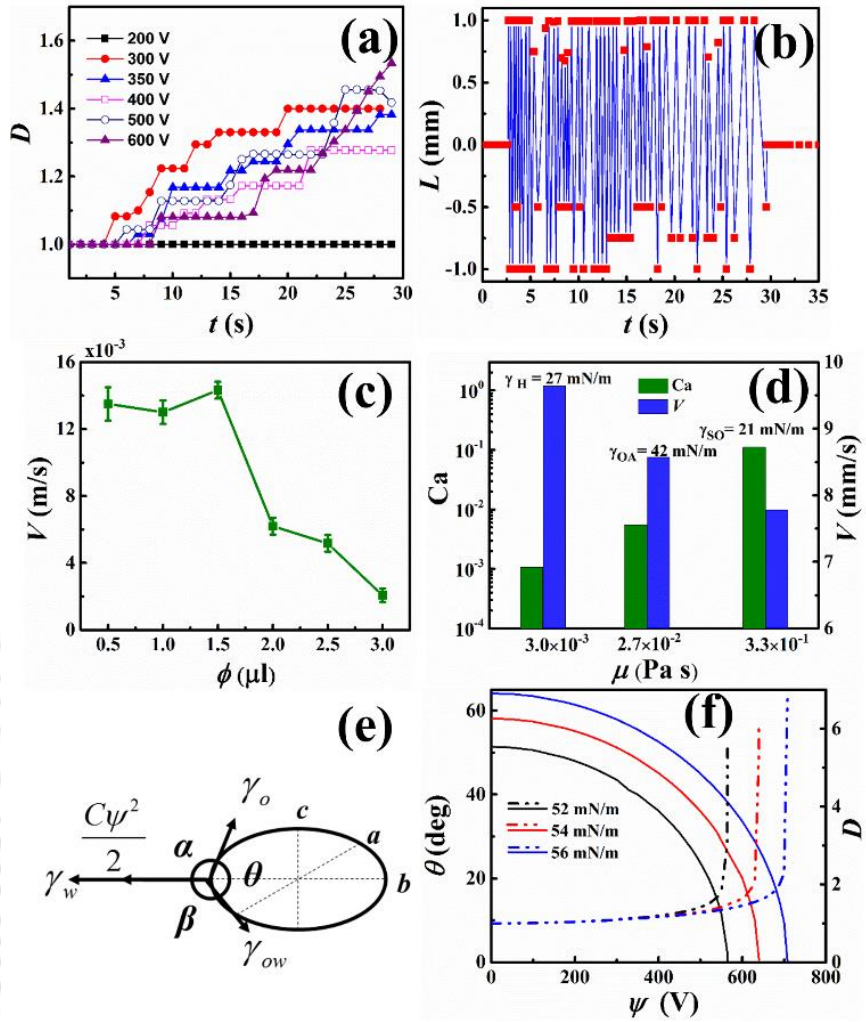

Figure 4.3. Plot (a) shows the variation in the normalized diameter of the droplet, $D = d/D_i$, with time (t) for a series of applied voltage (ψ) where d is the variable diameter and D_i is the initial diameter of an oil droplet of volume ϕ_o = 1 µl. Plot (b) shows the variation in the amplitude of oscillation (L) with time (t) at 550 V for an oil droplet of ϕ_o = 1 µl. Plot (c) shows the variation in the average ejection velocity (V) with the volume of oil droplet (ϕ_o) at 800 V. Plot (d) shows the variation in Capillary number (Ca) and the ejection velocity (V) of the oil droplets composed of oils of different viscosity when ϕ_o = 1 µl and ψ = 800 V. Image (e) shows the directions of the interfacial tensions at the three-phase contact line when electric field was applied to an oil droplet resting on a water surface. Plot (f) shows that the progressive change in the contact angle and diameter of a hexadecane oil droplet (ϕ_o =1 µl) with ψ, for different oil-water interfacial tension. Other necessary properties are tabulated in the Table 4.1.

oscillation of droplet around the Pt electrode. Here the position of the stationary Pt electrode was set as the zero to evaluate the amplitude of the oscillation.

It may be noted here that the electrode was never placed exactly at the centre of the oil droplet, which ensured the asymmetric distribution of induced dipoles across oil-air and oil-water interfaces. Thus, when an electric field of moderately high intensity was abruptly generated across the electrodes, the oil-water-air contact line near the electrode underwent rapid change in contact angle as compared to the other part of the droplet. As a measure of relaxation of the EHD stress and also to achieve an equilibrium contact angle in presence of the electric field, the droplet oscillated around the electrode. The water layer under the droplet facilitated the oscillation allowing strong slippage at the oil-water interface.

Figures 4.2 (i-l) show that when the strength of the electric field was increased to 800 V, the droplet ejected out of the Pt electrode to relax the EHD stresses. The figures and the video suggest that the droplet ejected out at a very high speed from the Pt electrode before slowing down on the water surface at a distance, owing to the friction at the water-oil interface. Figure 4.3 (c) and 4.3 (d) show that the magnitude of the ejection velocity was as high as ~ 5 body length/s and with increase in the viscosity and size of the droplet the ejection velocity reduced. Here we reported the average velocities of the droplets, which were measured as the time taken to travel 1 cm distance after ejection. The plots suggest that increase in viscosity of the droplet enhanced the frictional resistance against the motion while increase in the size led to the enhanced drag force and the body force due to gravity, which led to the reduction in velocity. The magnitudes of Capillary number, $Ca = \mu_o V/\gamma_o$, in the Figure 4.3 (d) show the roles of viscosity and surface tension on the speed of the ejected droplet. The plot suggests that the velocity of the oil droplet increased with reduction in the magnitude of *Ca*.

Figure 4.3 (e) shows a typical Neumann's triangle for an oil droplet resting on a water layer where, $\alpha+\beta+\theta=2\pi$ and α, β, and θ are the angles as shown. We assumed that the electric field ($\Delta G_E=0.5C\psi^2$) was effective in the direction of γ_w to spread the oil droplet, which led to the following set of energy balances for the proposed EWOL setup,

$$\left(\gamma_w+0.5C\psi^2\right)+\gamma_{ow}\cos\beta+\gamma_o\cos\alpha=0, \quad (4.3.1)$$

$$\gamma_o+\left(\gamma_w+0.5C\psi^2\right)\cos\alpha+\gamma_{ow}\cos\theta=0, \quad (4.3.2)$$

$$\gamma_{ow}+\gamma_o\cos\theta+\left(\gamma_w+0.5C\psi^2\right)\cos\beta=0. \quad (4.3.3)$$

Here γ_w, γ_{ow} and γ_o were the interfacial tensions of water-air, oil-water, and oil-air interfaces, respectively. The capacitance (C) for the oil, water, and PTFE was obtained assuming a parallel plate capacitor as, $C^{-1}=\sum C_i^{-1}$ where $C_i=\varepsilon_0\varepsilon_i/h_i$. Here C_i, ε_i, and h_i denoted the capacitance, dielectric constant, and thickness of the i^{th} layer (where 'o' is oil, 'w' is water, and 'T' is PTFE) and ε_0 was the dielectric permittivity of the free space. We solved the three energy equations to obtain the angles α, β, and θ for a known ψ. The typical values for the aforementioned parameters in the EWOL setup is shown in the Table 5.1 [65-71]. The solid lines in the Figure 4.3 (f) shows the theoretical reduction in θ as the droplet expanded when the electric field potential was increased, as observed in the experiments. Under these circumstances, considering the droplet to be an ellipsoid of volume, $(4/3)\pi abc$, where the length of the major (a), minor (b), and vertical (c) axes as denoted, we evaluated the variation in the diameter of the droplet as per the expression, $a=\sqrt[3]{3/4\pi\tan\theta}$, plotted as broken lines in the Figure 4.3 (f). The theoretical calculations suggested that, under the given parametric space, the droplet expansion was significant

only beyond an electric field potential of ~400 V, which was very similar to the experimental observations.

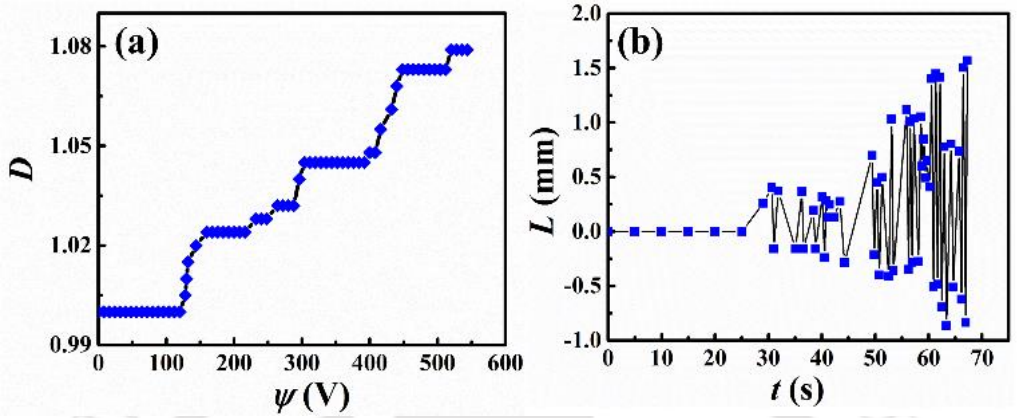

Figure 4.4. Plot (a) shows the typical variation in the normalized droplet diameter (D) with ψ when the voltage was changed at a rate of 8 V/s for ϕ_0 = 1 µl. Plot (b) shows the variation in the amplitude of oscillation (L) with time (t) during the oscillation and the voltage was increased at a rate of 8 V/s. Other necessary properties are tabulated in Table 4.1.

Figure 4.4 show another interesting situation where the applied potential was progressively increased at a rate of 8 V/s. Interestingly, the video shows all the three motions such as expansion, oscillation, and ejection with progressive increase in the voltage. Plot (a) shows the typical rate of expansion when the rate of increase in the voltage was 8 V/s. Following this, the droplets started showing an oscillatory behavior before ejecting out of the electrode. The plot (b) shows the amplitude of oscillation (L) progressively increased with time before the droplet ejected out of the zone of electric field exposure. Concisely, the Figures 4.2 – 4.4 together show interesting droplet motions such as spreading, oscillation, and ejection when electric field was applied in an EWOL setup.

Figure 4.1 (d) schematically showed that the addition of a permanent magnet of field strength, **B**, to the EWOL setup could develop Lorentz force ($\mathbf{F}_L = \mathbf{J}_L \times \mathbf{B}$). The electric field component of the Lorentz force was expected to arise from the form the leakage current density (J_L) through the DI water and PTFE isolators in the EWOL setup when a relatively high intensity electric field was generated across the electrodes.

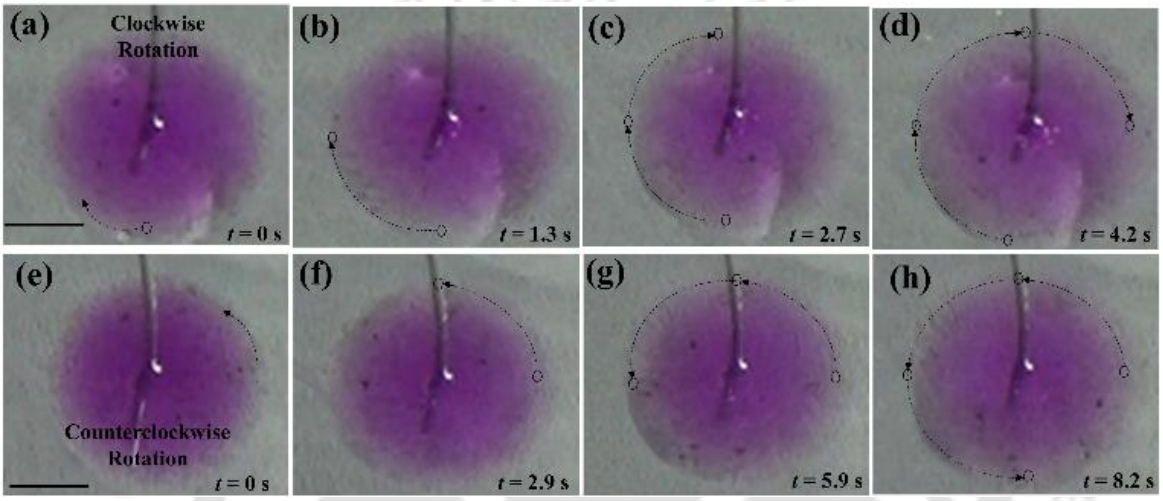

Figure 4.5. Rotational motion of oil droplet on water surface under the Lorentz force. Images (a-d) show the clockwise spinning and the images (e-f) show the anticlockwise spinning of the droplet. The experimental parameter in the EWOL setup were, ϕ_0 = 1 µl, ψ = 300 V, and magnetic field, B = 240 mT. The scale bar is 1 mm as shown in the image (a). Other necessary properties are tabulated in the Table 4.1.

Figure 4.5 show the rotational motions were observed in the EWOL setup when placed on a permanent magnet. The clockwise [images (a) – (d)] and anticlockwise [images (e) - (h)] rotations of the droplets took place due to the change in the direction of the Lorentz force when the direction of the poles of the magnet changed. We could achieve rotational speed as high as 300 degrees per second when the magnetic field strength was 240 mT and when the applied potential was about 300 V.

Figure 4.6 shows the parametric variations of the spinning droplet under the influence of the Lorentz force. The plot (a) shows the magnitude of the leakage current (I_L) with the variation in ψ in presence and absence of the oil droplet.

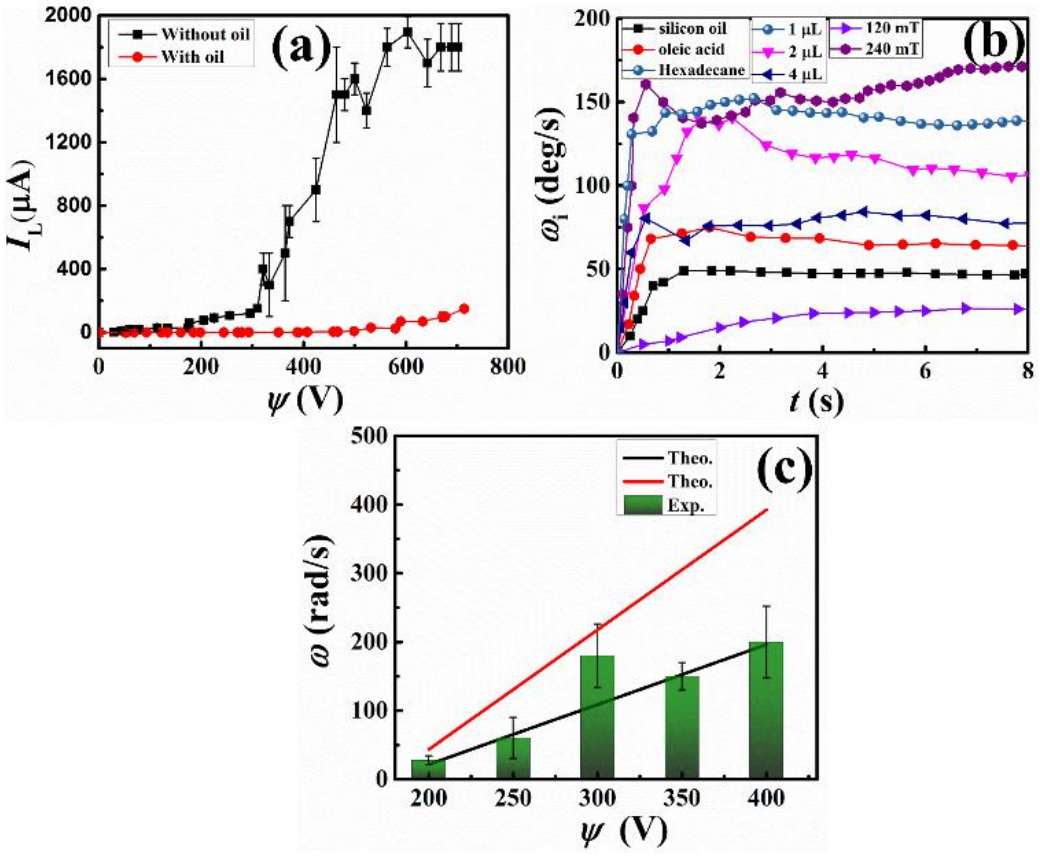

Figure 4.6. Image (a) shows the magnitude of leakage current (J_L) at different ψ with oil and without oil droplet. Image (b) shows the speed of rotation (ω) with time (t) for the droplets composed of silicon oil, oleic acid and hexadecane on water bath at ψ = 300 V, B = 120 mT, and ϕ_0 = 1 µl. The plot also shows the effects of hexadecane droplet size (ϕ_0, 1 – 4 µL) at ψ = 300 V, B = 120 mT, and magnetic field (B, 120 mT and 240 mT) at ψ = 200 V, ϕ_0 = 1 µl. Plot **(c)** shows the experimental rotation speed (bar diagrams) when applied potential ψ = 200 to 400 V, B = 120 mT, and ϕ_0 = 1 µl and solid lines represents the theoretical prediction for B= 120 mT (darker shade in black) and B = 240 mT (lighter shade in red) when ψ = 200 to 400 V. Other necessary properties are tabulated Table 4.1.

The plot suggests that the typical range of I_L was about a few µA – mA. Importantly, the leakage current ensured accumulation of the electrons or holes near the oil-water interface,

which in coupling with the magnetic field could generate enough Lorentz force to rotate the droplet on the water bath. Plot (b) shows the typical variations in the speed of rotation (ω) with time (t) when the size of the droplet, electric field potential, strength of the magnetic field, and the viscosity of the droplets were varied. The plots show that at the initial stages the droplets started rotating at a smaller speed, which settled to a constant value after a definite time period. Understandably, the speed of rotation of the droplet was found to be higher with reduction in the size of the droplet, increase in the electric or magnetic field strength, and reduction in the viscosity of the droplet.

The speed of rotation for the droplet obtained from the experiments (bar diagrams) were compared and contrasted with a simple theoretical (solid line) model, as shown in the plot (c). We applied the Newton's second law of motion ($F_L + F_d = 0$) in the limit of Stokes flow where the torque ($\tau = 8\pi\mu_w \omega r^3$) on a steady rotating body led to a drag force of, $F_d = 8\pi\mu_w \omega r^2$,[72] against the Lorentz force, $F_L = J_L B\phi_0$,[73] for a droplet of radius r. The expression for the theoretical rotational speed from these expressions was obtained as, $\omega = J_L B\phi_0 / 8\pi\mu_w r^2$, which was plotted against the experimental values obtained in the plot (c). The predictions from the theory matched fairly well with the measured experimental values. The theoretical expression corroborated that indeed the rotational speed would be higher for the cases where the applied field intensity or the magnetic field strength were higher and the size of the droplet and the frictional influences were lower.

Figure 4.7 show another interesting case when the droplet was rotated at a higher speed for a longer duration under the influence the stronger Lorentz force. Images (a) – (f)

schematically show the mechanism of the breaking of the droplet during rotation while images (g) – (l) show the real time images of the same phenomenon.

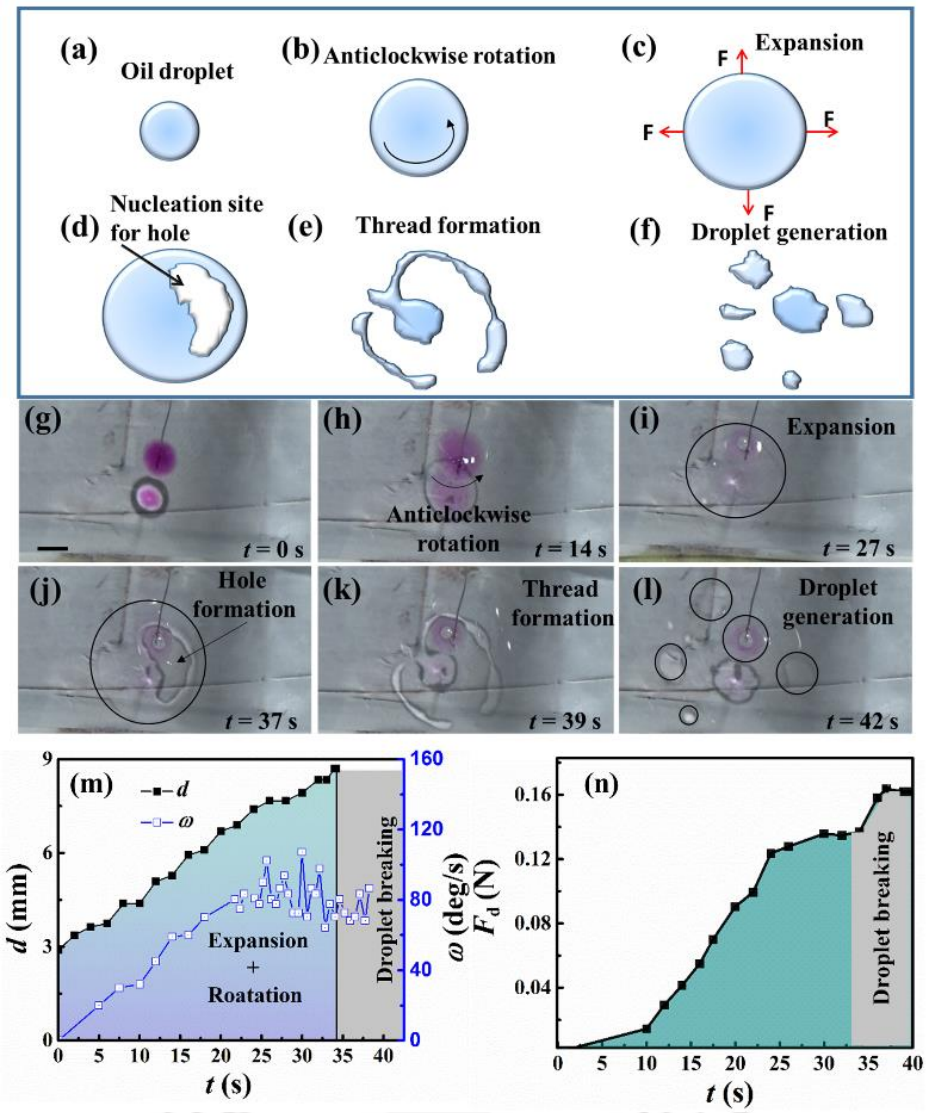

Figure 4.7. Schematic images (a) – (f) show the typical breaking of a spinning hexadecane droplet under the influence of the Lorentz force. Images (g) – (l) show the real-time images of the same phenomenon. In this experiment, ϕ_0 =1 µl, B =120 mT, and ψ = 300 V. The plots (m) and (n) show the variations in the diameter of the droplet (d), speed of rotation (ω), and drag force (F_d) on the droplet with time (t). The scale bar is 2.5 mm as shown in image (g). Other necessary properties are tabulated in Table 4.1.

The motion shown here initiated with the spreading of the droplet in the EWOL setup at the initial stages due to the EHD stresses accumulated near the three-phase contact line

and also because of the centripetal force originating from the rotation of the droplet. The combined influence of the electric and magnetic fields generated enough centripetal force, which helped the droplet to spread while rotating at a higher speed on a strongly slipping water surface. The water surface also provided the necessary shear after a prolonged rotation to cause the cohesive failure and slowly disintegrate the droplet into many parts. Plots (m) and (n) show the typical variations in the diameter of the droplet (D), speed of rotation (ω), and drag force (F_d) on the droplet with time (t). In parallel to the spreading and rotation, a few bubbles were also observed during the droplet rotation due to the electrolysis of water. The bubbles acted as nucleation sites for the breakup of the droplet although the cohesive failure took place mainly due to a higher degree of shear exerted [plot (n)] on the spreading droplet during its rotation at a relatively higher speed [plot (m)]. Briefly, the Figures 4.5 – 4.7 show some interesting rotational behaviours and subsequent breaking of droplets employing an EWOL setup.

4.4 SUMMARY

In summary, we have shown a host of technologically important motions of a droplet on an electrowetting setup composed of an oil microdroplet resting on liquid water layer. The study uncovers that the oil droplet could be deformed only after a critical strength of the applied electric field when it overpowers the restoring surface tension and viscous forces. Beyond a critical limit of the electric field, the droplet showed spreading, oscillation, and ejection motions on the water surface with the increase in the applied field intensities. Smaller and less viscous droplets showed speed of ejection as high as 5 body length per second owing to the lower drag force at the oil-water interface. A simple theoretical model based energy equations corresponding to the Neumann's triangle modified with the electric field component has been proposed to theoretically calculate the change in the

contact angle of the droplet and the subsequent change in the diameter during spreading. Placing the EWOL setup on a permanent magnet could engender interesting rotational motion, which was attuned to the change in the electric or magnetic field intensity. Even the direction of rotation could be controlled by changing the direction of the poles or the applied electric field. A simple theoretical model based on Stokes flow could explain the Lorentz force induced rotational motion of the oil droplet. Increasing the speed of rotation led to the spreading of the droplet under the influence of the centripetal force, which in conjunction with the EHD stress at the oil-water interface led to the cohesive failure of the droplet to form a number of miniaturized ones. The reported oscillatory and rotational motions of the incompressible droplet could be employed as stirrers or impellers inside the microfluidics devices for mixing or pumping applications. Further, the droplet ejection could be employed to develop futuristic devices such as the payload transporters or drug delivery vehicles.

REFERENCES

1. M.G. Lippmann, *Ann. Chim. Phys*, 1875, **5,** 494-549.
2. A. Frumkin, *J. Phys. Chem. (USSR)*, 1938, **12**, 337-345.
3. G. Taylor, *Proc. R. Soc. Lond. A Math. Phys. Sci.*, 1964, **280**, 383-397.
4. J. Lee and C. J. Kim, *Proc. IEEE MEMS*, 1998, 538-543.
5. Y. Wang and Y.-P. Zhao, *Soft Matter*, 2012, **8**, 2599-2606.
6. D. J. Lomax, P. Kant, A. T. Williams, H. V. Patten, Y. Zou, A. Juel, and R. A. W. Dryfe, *Soft Matter*, 2016, **12**, 8798-8804.
7. F. Taherian, F. Leroy, L.O. Heim, E. Bonaccurso, and N. F. A. van der Vegt, *Langmuir*, 2016, **32**, 140-150.
8. G. Beni, and S. Hackwood, *Appl. Phys. Lett.*, 1981, **38**, 4, 207-209.
9. F. Mugele, and J. C. Baret, *J. Phys. Condens. Matter*, 2005, **17**, 705-774.
10. C. Quilliet, and B. Berge, *Curr. Opin. Colloid Interface Sci.*, 2001, **6,** 34-39.

11. F. Mugele, M. Duits, and D. van den Ende, *Adv. Colloid Interface Sci*., 2010, **161**, 115-123.
12. F. Mugele, *Soft Matter* 2009, **5**, 3377-3384.
13. H. H. Girault, *Nat. Mater*., 2006, **5**, 851-852.
14. D. D. Joseph and Y. Y. Renardy, Fundamentals of Two-Fluid Dynamics, Part I: Mathematical Theory and Applications (Springer, Berlin), 1993.
15. S. Chandrasekhar, *Hydrodynamic and Hydromagnetic Stability* (Oxford University Press, New York), 1981.
16. P. A. Davidson, *An Introduction to Magnetohydrodynamics* (Cambridge University Press, Cambridge), 2001.
17. M. Dhindsa, J. Heikenfeld, W. Weekamp and S. Kuiper, *Langmuir*, 2011, **27**, 5665-5670.
18. B. Berge, *C. R. Acad. Sci. II*, 1993, **317**, 157-163.
19. S. J. Lee, J. Hong, K. H. Kang, I. S. Kang, and S. J. Lee, *Langmuir*, 2014, **30**, 1805-1811.
20. Q. Yang, B. Q. Li, and Y. Ding, *Soft Matter*, 2013, **9**, 3412-3423.
21. A. Sharma, V. Tiwari, V. Kumar, T. K. Mandal, and D. Bandyopadhyay, *Electrophoresis*, 2014, **35**, 2930-2937.
22. J. Chaudhuri, S. Timung, C. B. Dandamudi, T. K. Mandal, and D. Bandyopadhyay, *Electrophoresis*, 2017, **38**, 278-286.
23. S. Timung, J. Chaudhuri, M. P. Borthakur, T. K. Mandal, G. Biswas, and D. Bandyopadhyay, *Electrophoresis*, 2017, **38**, 1450-1457.
24. F. Mugele, A. Staicu, R. Bakker, and D. van den Ende, *Lab Chip*, 2011, **11**, 2011-2016.
25. P. Dubois, G. Marchand, Y. Fouillet, J. Berthier, T. Douki, F. Hassine, S. Gmouh and M. Vaultier, *Anal. Chem.*, 2006, **78**, 4909-4917.
26. N. Miljkovic, D. J. Preston, R. Enright, and E. N. Wang, *Appl. Phys. Lett.*, 2014, **105**, 013111:1-5.
27. M. Bhattacharjee, V. Pasumarthi, J. Chaudhuri, A. K. Singh, H. Nemade, and D. Bandyopadhyay, *Nanoscale*, 2016, **8**, 6118–6128.
28. R. Peng, J. Chen, and S. Zhuang, *J. Opt. Soc. Am. A*, 2008, **25**, 2644-2650.
29. K. L. Wang, and T. B. Jones, *Langmuir* 2005, **21**, 4211–4217.

30. D. Y. Kim, and A. J. Steckl, *ACS Appl. Mater. Interfaces*, 2010, **2**, 3318-3323.
31. H. H. Shen, S. K. Fan, C. J. Kim, and D. J. Yao, *Microfluid. Nanofluid.*, 2014, **16**, 965-987.
32. S. Deladi, J. F. Suijver, Y. S. Shi, K. Shahzad, B. M. de Boer, A. J. J. Rademakers, C. van der Vleuten, L. Jankovic, E. Bongers, E. Harks, and S. Kuiper, *Appl. Phys. Lett.*, 2010, **97**, 064102:1-3.
33. F. Krogmann, W. Mönch and H. Zappe, *J. Opt. A-Pure and Appl. Op.*, 2006, **8**, 330-336.
34. D. Chatterjee, B. Hetayothin, A. R. Wheeler, D. J. King and R. L. Garrell, *Lab Chip*, 2006, **6**, 199-206.
35. S. K. Cho, H. J. Moon, and C. J. Kim, *J. Microelectromech. Syst.*, 2003, **12**, 70–80.
36. S. Kumar, M. R. Ali Faridi, A. K. Dasmahapatra and D. Bandyopadhyay, *RSC Adv.*, 2016, **6**, 107049-107056.
37. H. J. J. Verheijen and M. W. J. Prins, *Langmuir*, 1999, **15**, 6616–6620.
38. J. Y. Chen, A. Kutana, C. P. Collier, and K. P. Giapis, *Science*, 2005, **310**, 1480–1483.
39. N. Verplanck, E. Galopin, J. C. Camart, and V. Thomy, *Nano Lett.*, 2007, **7**, 813–817.
40. J. L. Campbell, M. Breedon, K. Latham, and K. Kalantar-Zadeh, *Langmuir*, 2008, **24**, 5091–5098.
41. G. Manukyan, J. M. Oh, D. van den Ende, R. G. H. Lammertink, and F. Mugele, *Phys. Rev. Lett.*, 2011, **106**, 014501:1-4.
42. M. S. Dhindsa, N. R. Smith, J. Heikenfeld, P. D. Rack, J. D. Fowlkes, M. J. Doktycz, A. V. Melechko, and M. L. Simpson, *Langmuir*, 2006, **22**, 9030-9034.
43. T. Krupenkin, and J. A. Taylor, *Nat. Commun.*, 2011, **2**, 448:1-7.
44. A. R. Wheeler, *Science* 2008, **322**, 539–540.
45. R. Dey, A. Daga, S. DasGupta, and S. Chakraborty, *Appl. Phys. Lett.*, 2015, **107**, 034101:1-5.
46. C. Hao, Y. Liu, X. Chen, Y. He, Q. Li, K. Y. Li and Z. Wang, *Sci. Rep.*, 2014, **4**, 6846:1-7.

47. A. A. Kornyshev, A. R. Kucernak, M. Marinescu, C. W. Monroe, A. E. S. Sleightholme, and M. Urbakh, *J. Phys. Chem. C*, 2010, **114**, 14885-14890.
48. R. A. Hayes, and B. J. Feenstra, *Nature*, 2003, **425**, 383-385.
49. B. Sun, and J. Heikenfeld, *J. Micromech. Microeng.*, 2008, **18**, 025027:1-8.
50. W. Ritchie, *Phil. Trans. R. Soc.*, 1832, **122**, 279-298.
51. H. S. Kabbani, M. J. Mack, S. W. Joo, and S. Qian, *J. Fluids Eng.*, 2008, **130**, 091204:1-6.
52. J. Jang, and S. S. Lee, *Sens. Actuators A-Phys.*, 2000, **80**, 84-89.
53. A.V. Lemoff, and A. P. Lee, *Sens. Actuators B-Chem.*, 2000, **63**, 178-185.
54. H. H. Bau, J. Zhong, and M. Yi, *Sens. Actuators B-Chem.*, 2001, **79**, 207-215.
55. H. H. Bau, J. Zhu, S. Qian, and Y. Xiang, *Sens. Actuators B-Chem.*, 2003, **88**, 205-216.
56. J. Zhong, M. Yi, and H. H. Bau, *Sens. Actuators A- Phys.*, 2002, **96**, 59-66.
57. A. Gelb, J. P. Gleeson, J. West and O. M. Roche, *SIAM J. Appl. Math.*, 2004, **64**, 1294-1310.
58. M. Yi, S. Qian and H. H. Bau, *J. Fluid Mech.*, 2002, **468**, 153-177.
59. S. Qian, J. Zhu, and H. H. Bau, *Phys. Fluids*, 2002, **14**, 3584-3592.
60. S. Qian, and H. H. Bau, *Mech. Res. Commun.*, 2009, **36**, 10-21.
61. M. C. Weston, M. D. Gerner and I. Fritsch, *Anal. Chem.*, 2010, **82**, 3411-3418.
62. P. D. S. Reddy, D. Bandyopadhyay, S. W. Joo, A. Sharma, and S. Qian, *Phys. Rev. E*, 2011, **83**, 036313:1-14.
63. D. Bandyopadhyay, P. D. S. Reddy, A. Sharma, S. W. Joo, and S. Qian, *Theor. Comp. Fluid Dyn.*, 2012, **26**, 23-28.
64. J. L. Aragones, J.P. Steimel, and A. Alexander-Katz, *Nat. Commun.*, 2016, **7,** 11325:1-9.
65. E. A. van Nierop, A. Ajdari and H. A. Stone, *Phys. Fluids*, 2006, **18**, 038105:1-4.
66. P. Than, L. Preziosi, D. D. Josephl and M. Arney, *J. Colloid Interface Sci.*, 1988, **124**, 552-559.
67. H. B. d. Aguiar, A. G. F. d. Beer, M. L. Strader and S. Roke, *J. Am. Chem. Soc.*, 2010, **132**, 2122-2123.
68. P. Ehrlich, *J. Res. Natl. Stand.*, 1953, **51**, 185-188.
69. C. G. Malmberg and A. A. Maryott, *J. Res. Natl. Bur. Stand.*, 1956, **56**, 1-8.

70. S. Mhatre and R. Thaokar, *Ind. Eng. Chem. Res.*, 2014, **53**, 13488-13496.
71. US pat., US 6274067 B1, 2001.
72. U. Lei, C. Y. Yang and K. C. Wu, *Appl. Phys. Lett.*, 2006, **89**, 181908:1-3.
73. A. Homsy, S. Koster, J. C. T. Eijkel, A. van den Berg, F. Lucklum, E. Verpoorte and N. F. de Rooij, *Lab Chip*, 2005, **5**, 466-471.

Chapter 5

Self-organized Superspreading of Droplets to form Fluid-Toroids

5.1 INTRODUCTION

The solid objects can be of various size and shapes because of their capacity to retain the same owing to the presence of the restoring elastic forces [1-6]. In comparison, the supremacy of the capillary forces ensures that ever-yielding fluidic objects always settle with the shapes of minimum surface energy [7,8]. One of the very long-standing challenges in this regard has been the fabrication of metastable liquid sheets [9], threads [10], toroids [11], or ellipsoids [12], which transiently show up in many artificial as well as natural processes. For example, the dolphins or smokers are famous for creating toroidal rings [13,14] while the formation and collapse of DNA-protein nano-toroids at the sub-cellular level is also fascinating scientific phenomenon, yet to be understood in details [15]. The freely falling droplets [16-18] or bubbles [19], the droplets bouncing on the super-repellant surfaces [20], or solid objects hitting the liquid surface momentarily develop shapes resembling toroid, crown, doughnut, peanut, prolate, or oblate geometrical patterns. A bubble or a droplet can also form a torus or triangle when mechanically vibrated [21] or rotated under the electromagnetic fields [22,23]. In general, to minimize the surface energy most of the fluidic objects with non-minimum surface energies transform into spherical droplets undergoing the capillary instability.

Centuries back, Plateau assisted by the able hands of Mensbrugghe pioneered the development of toroidal fluidic objects by piercing a liquid droplet at the center with a metal shaft before rotating at different speeds [24] Since then, lots of efforts have been invested on the development of liquid objects of metastable shape and size [25-27]. A number of theoretical works have demonstrated the diverse stability characteristics of toroidal liquid objects resting on the sold surface [28, 29]. A recent seminal study has shown that rather than rotating the droplet another alternative can be to inject a less

viscous liquid into a rotating bath of a more viscous and immiscible liquid to form a toroidal object [11, 30-31]. In this case, the kinetic stabilization of the interfacial deformation originating from the interplay between the centripetal, viscous, and capillary forces leads to the formation of the liquid-toroid. However, almost all the experimental methodologies invented so far employ rotation of either the droplet or the surrounding medium to develop the toroidal fluidic structures. There is no report as such, which can form toroidal objects composed of fluids in absence of rotational influence.

Herein, we demonstrate that a simple chemical trigger can self-organize an oil droplet on a water surface into a toroidal shape in absence of any rotational influence. The abrupt reduction of interfacial tension due to the chemical trigger stimulates a rapid spreading of the oil droplet on the water surface to develop the metastable toroidal structure. High speed imaging of the process uncovers the inclusive dynamics consisting of seven stages: (i) droplet spreading, (ii) formation of toroid connected to a thin liquid-sheet, (iii) separation of the toroid and liquid-sheet, (iv) dewetting of the liquid-sheet on the eater surface to form microdroplets, (v) expansion of the toroid, (vi) breakup of the toroid into threads, and (vii) formation of microdroplets from the toroid. A parametric study with the variations in the viscosities of the fluids and the interfacial tensions at the fluid boundaries uncover two different pathways of toroid formation: laminar mode – where the symmetric toroids are observed at lower Reynolds (*Re*) number and turbulent mode – formation of the asymmetric toroids at a higher *Re*. Simple theoretical models have been developed based on the thin film equations of a liquid droplet resting on a fluid surface and subsequently a linear stability analysis is performed to predict, (i) the cross-sections of a toroid resting on a liquid surface under the varied experimental conditions and (ii) length scale of the disintegration of the toroids on a soft-deformable liquid surface.

Interestingly, at the intermediate stages, the toroid formation phenomenon is also associated with an oil-sheet formation on the water surface. The dewetting of this oil-sheet forms an 'oil-in-water' microemulsion inside the toroidal territory, which is found to be very different from the previously reported dewetting of thin films on the homogeneous [33-46], patterned [47-50], or slipping [51] surfaces to develop ordered micro or nanostructures [52-55]. The proposed methodology to develop the metastable fluidic objects such as toroids, sheets, or threads and their breakup can be useful for a number of applications such as emulsifiers [56], 3D-printing [57], droplet or digital microfluidics [58-60], microreactors [61].

5.2 EXPERIMENTAL SECTION

5.2.1 Materials

Pentanol ($C_5H_{11}OH$), 99.8% methanol (CH_3OH), 99.5% ethanol (C_2H_5OH) and oleic acid ($C_{18}H_{34}O_2$) were procured from Merck (India) Ltd. Surfactant, polysorbate – Tween 20 ($C_{58}H_{114}O_{26}$) was purchased from Sisco Research laboratories Pvt. Ltd. Rhodhamine 6G dye ($C_{28}H_{31}ClN_2O_3$), toluene (C_7H_8) and polystyrene [$(C_8H_8)_n$ – (M_W 2500 g mol^{-1}] were purchased from Sigma Aldrich (India). All the chemicals were of analytical grade and used without further purification. The Milli-Q grade water was used to prepare all the solutions and also for cleaning the glassware.

5.2.2 Methods

For experimental setup, a glass petri dish of 90 mm diameter was initially filled with 30 ml of water. After that, 20 µl of oleic acid was dispensed through a micropipette on the water bath, which led to the formation of an oleic acid droplet or lens on the water surface. Following this, 5 µl pentanol was dispensed on the oleic acid droplet, which

broke down the oleic acid droplet into smaller ones. The breaking of the oleic acid droplet was recorded with a digital camera (Make – Cybershot DSC-HX100V, Sony Corp., Japan). The dynamics were also followed under an upright microscope (Make - Leica DM 2500) with a high speed-high resolution digital camera (Make – Fastcam Mini UX100, Photron Ltd.). The image analyses of the movies were performed by open source imageJ software. Similar experiments were performed with, (i) pentanol was replaced by a solution of water and surfactant keeping the other components similar to aforementioned system, (ii) oleic acid was replaced by silicone oil, (iii) glycerol is added to the water bath at the bottom, and (iv) oleic acid was replaced by a solution of polystyrene in toluene.

Table 5.I. Experimental determination of physical properties [62]

Materials	**Viscosity (Pa s)**	**Surface tension (mN/m)**	**Density (kg/m^3)**	**Solubility**
Water	0.001	69.3	1000	
Oleic acid	0.0277	42.0	895	Insoluble in water
Glycerol	0.90568	62.4	1260	Soluble in water
Pentanol	0.004	32.1	814	Soluble in water (25 g/L)
Methanol	0.00543	22	792	Soluble in water
Ethanol	0.00109	22	789	Soluble in water
Propanol	0.00192	20	803	Soluble in water
Hexadecane	0.003	27	770	Insoluble in water

The surface and interfacial tensions were measured at room temperature (25°C) using a digital tensiometer (Make – Krüss, K9) employing the du Noüy ring (Pt/Ir) method where ASTM standard procedure D1331-11 (2001) was followed. Table I shows the typical values of surface or interfacial tensions measured for the fluids used in this study. The viscosity of the fluids was measured using an interfacial rheometer (Make – Anton Paar,

Physica MCR 301) in which the cone and plate setup was used to measure the bulk viscosity. Table 5.1 shows the typical values of viscosities measured for the fluids used.

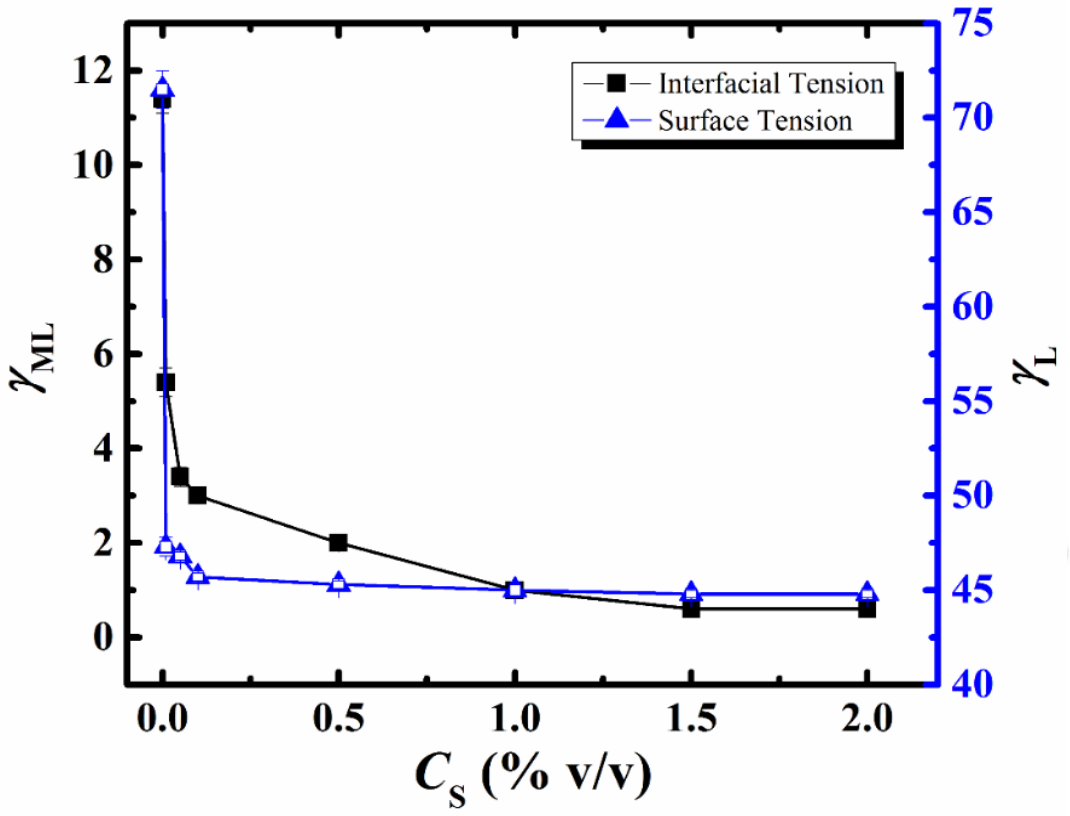

Figure 5.1. The variations in the interfacial tensions at the oil-water interface (γ_{ML}) and water-air interface (γ_L) with the variation in the surfactant loading (C_S, % v/v).

Figure 5.1 shows the typical variations in the variations in the interfacial tensions at the oil-water interface (γ_{ML}) and water-air interface (γ_L) with the variation in the surfactant loading (C_S, % v/v). The data were evaluated from the tensiometer experiments for the materials, (a) water loaded with surfactant, and (b) oleic acid-water interface loaded with surfactant. The plots suggest that in both the situations the interfacial tensions reduced significantly.

5.2.3 Theoretical Formulation

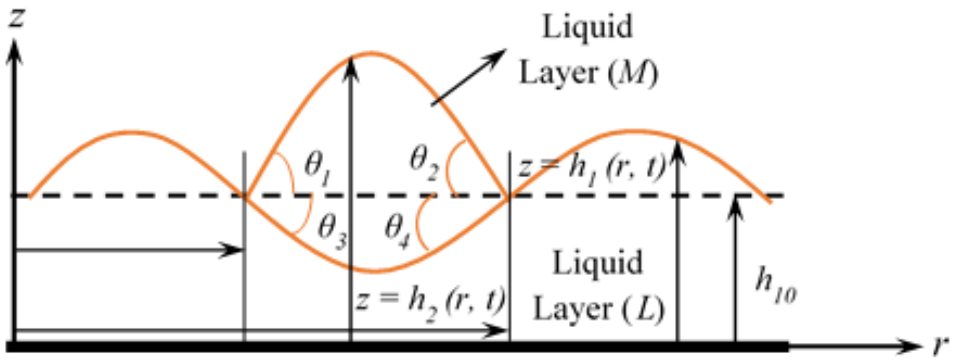

Figure 5.2. Front view or cross-sectional view of the toroid represented schematically. The lower liquid layer (L) film and the combined lower and middle (M) liquid layer film thicknesses are denoted by h_1 (r, t) and h_2 (r, t), respectively. The mean film thickness of the lower layer is h_{10}. Inner and outer radii of the middle liquid layer are denoted by r_1 and r_2 (> r_1), respectively. The contact angles of the both middle and lower liquid layers with the mean lower film thickness at the inner edge [outer edge] are specified as θ_1 and θ_3 [θ_2 and θ_4], respectively.

The typical thickness profile of the toroid formed by the liquid layers (L and M) is explained by solving a static base state obtained within the framework of the nonlinear long-wave hydrodynamics theory for thin liquid bilayers with free surface [45,46]. Figure 5.2 schematically illustrates the front view geometry of the problem and introduces all important variables such as film thicknesses of the liquid layers, radii and contact angles at the inner and the outer contact lines. A cylindrical coordinated system (r, ϕ, z) is used where r, ϕ and z represent the radial, the azimuthal and the axial coordinates, and t represents time. Owing to the symmetry of the problem, it is natural to assume an axisymmetric toroid and we will restrict the formulation in the r and z-direction only. We follow the convention where the subscript i denotes the lower layer L (i = 1) and the middle layer M (i = 2). For the i^{th} layer: $\mathbf{v}_i \left\{v_{r_i}, v_{z_i}\right\}$, μ_i, γ_i, and p_i denoted the velocity

vector, viscosity, surface tension and static pressure in the liquid films, respectively, whereas γ_{ij} denotes the interfacial tension at the liquid-liquid interface.

We assumed that both the *L* and *M* layers are Newtonian thus, the equations of motion for the two layers in the long-wave regime, $-\partial p_i/\partial r+\mu_i\,\partial^2 v_{r_i}/\partial z^2=0$ and $-\partial p_i/\partial z=0\Rightarrow p_i\neq f(z)$, together with the continuity equation for the incompressible films, $\partial/\partial r\left(rv_{r_i}\right)+r\,\partial v_{z_i}/\partial z=0$, govern the hydrodynamics of the viscous bilayer shown in the figure 5.1. Following this, no-slip ($v_{r_1}=0$) and impermeability ($v_{z_1}=0$) boundary conditions at the liquid-solid interface ($z=0$), continuity of velocities ($v_{r_1}=v_{r_2}$ and $v_{z_1}=v_{z_2}$) at the liquid-liquid interface ($z = h_1(r, t)$), together with the tangential ($\mu_2\,\partial v_{r_2}/\partial z-\mu_1\,\partial v_{r_1}/\partial z=0$, and, $\partial v_{r_2}/\partial z=0$, respectively) and normal stress balances ($p_1=p_a-\gamma_2\,\partial^2 h_2/\partial r^2-\gamma_{12}\,\partial^2 h_1/\partial r^2$, and, $p_2=p_a-\gamma_2\,\partial^2 h_2/\partial r^2$) at the liquid-liquid ($z = h_1(r, t)$) and liquid-air ($z = h_2(r, t)$) interfaces are used to solve the components of the velocity vector. Here, p_a is the ambient gas pressure. Replacing the solutions of the velocities into the kinematic conditions for individual layers, $\partial h_i/\partial t+v_{r_i}\big|_{h_i}\,\partial h_i/\partial r=v_{z_i}\big|_{h_i}$, lead to the following set of nonlinear partial differential equations (PDEs) for the evolving interfaces of the liquid layers [45],

$$r\frac{\partial h_1}{\partial t}-\frac{\partial}{\partial r}\left[\frac{r}{\mu_1}\left(\frac{h_1^3}{3}\frac{\partial p_1}{\partial r}+\frac{h_1^2\left(h_2-h_1\right)}{2}\frac{\partial p_2}{\partial r}\right)\right]=0, \tag{5.2.1}$$

$$r\frac{\partial h_2}{\partial t}-\frac{\partial}{\partial r}\left[\frac{r}{\mu_2}\left(\left(\frac{\left(h_2-h_1\right)^3}{3}+\frac{\mu_2 h_1\left(h_2-h_1\right)}{\mu_1}\left(h_2-\frac{h_1}{2}\right)\right)\frac{\partial p_2}{\partial r}+\frac{\mu_2}{\mu_1}\frac{h_1^2}{2}\left(h_2-\frac{h_1}{3}\right)\frac{\partial p_1}{\partial r}\right)\right]=0. \tag{5.2.2}$$

Above set of nonlinear PDEs are made non-dimensional using the following dimensionless variables, $H_1 = h_1/h_{10}$, $H_2 = h_2/h_{10}$, $R = r/h_{10}$, $P_i = p_i/\left(\gamma_{12}/h_{10}\right)$, $M = \gamma_2/\gamma_{12}$, $T = t/\left(h_{10}\mu_1/\gamma_{12}\right)$, $\mu_r = \mu_2/\mu_1$. The resulting non-dimensional equations are,

$$R\frac{\partial H_1}{\partial T} - \frac{\partial}{\partial R}\left[R\left(\frac{H_1^3}{3}\frac{\partial P_1}{\partial R} + \frac{H_1^2\left(H_2 - H_1\right)}{2}\frac{\partial P_2}{\partial R}\right)\right] = 0, \tag{5.2.3}$$

$$R\frac{\partial H_2}{\partial T} - \frac{\partial}{\partial R}\left[R\left(\begin{array}{l}\left(\dfrac{\left(H_2 - H_1\right)^3}{3\mu_r} + H_1\left(H_2 - H_1\right)\left(H_2 - \dfrac{H_1}{2}\right)\right)\dfrac{\partial P_2}{\partial R} + \\ \dfrac{H_1^2}{2}\left(H_2 - \dfrac{H_1}{3}\right)\dfrac{\partial P_1}{\partial R}\end{array}\right)\right] = 0, \tag{5.2.4}$$

$$P_1 = P_a - MH_{2RR} - H_{1RR}, \tag{5.2.5}$$

$$P_2 = P_a - MH_{2RR}. \tag{5.2.6}$$

Typically with our aim to obtain radial thickness of the toroid, we have considered the base-state solutions of the two interfaces (L – M interface and M – air interface) introducing the following perturbations, $H_1\left(R,T\right) = H_{10}(R) + \varepsilon H_{10}'(R,T)$ and $H_2\left(R,T\right) = H_{20}(R) + \varepsilon H_{20}'(R,T)$, where $\varepsilon << 1$. By replacing these expressions into the Eqs. (5.2.3) – (5.2.6), and retaining only the base states and imposing the zero film thickness condition [28] at the contact lines ($H_{20}\big|_{R_1} - H_{10}\big|_{R_1} = 0$ and $H_{20}\big|_{R_2} - H_{10}\big|_{R_2} = 0$), we have the equilibrium equations as,

$$M\left(\frac{H_{10}^3}{3} + \frac{H_{10}^2\left(H_{20} - H_{10}\right)}{2}\right)\frac{d^3H_{20}}{dR^3} + \frac{H_{10}^3}{3}\frac{d^3H_{10}}{dR^3} = 0, \tag{5.2.7}$$

$$M\left(\frac{\left(H_{20}-H_{10}\right)^3}{3\mu_r}+H_{10}\left(H_{20}-H_{10}\right)\left(H_{20}-\frac{H_{10}}{2}\right)+\frac{H_{10}^2}{2}\left(H_{20}-\frac{H_{10}}{3}\right)\right)\frac{dH_{20}}{dR^3}+ \\ \frac{H_{10}^2}{2}\left(H_{20}-\frac{H_{10}}{3}\right)\frac{dH_{10}}{dR^3}=0 \quad . \qquad (5.2.8)$$

Along with the boundary conditions at fixed radii R_1 and R_2, contact angles of the both interfaces with mean lower film thickness at R_1 and R_2 can also be postulated as $dH_{20}/dR\big|_{R_1}=\tan\theta_1$, $dH_{10}/dR\big|_{R_1}=-\tan\theta_3$, $dH_{20}/dR\big|_{R_2}=-\tan\theta_2$, $dH_{10}/dR\big|_{R_2}=\tan\theta_4$ [28-29]. Eqs. (5.2.7) and (5.2.8) together with the boundary conditions stated above are solved numerically by employing the commercial package Mathematica™.

5.3 RESULTS AND DISCUSSION

Image (I) in the Figure 5.3 schematically shows the experimental setup in which a 90 mm glass petri dish was initially filled with 30 ml water (lower layer, '*L*') and an immiscible 20 µl oleic acid droplet (middle layer, '*M*') was dispensed on the water surface. It is well known that oleic acid forms a droplet-lens when it is dispensed in a little excess on a water surface although it has a lower surface tension than water. Image (I) also shows that the oleic acid droplet resting on the water surface satisfy the surface energy balances expressed by the Neumann's triangle, $\alpha+\beta+\theta=2\pi$, $\gamma_{LA}+\gamma_{ML}\cos\beta+\gamma_{MA}\cos\alpha=0$, $\gamma_{MA}+\gamma_{LA}\cos\alpha+\gamma_{ML}\cos\theta=0$, and $\gamma_{ML}+\gamma_{MA}\cos\theta+\gamma_{LA}\cos\beta=0$, where α, β, and θ are the angles as shown, γ_{LA}, γ_{ML} and γ_{MA} corresponds to the interfacial tensions of water-air, oil-water, and oil-air interfaces, respectively. Following this, a 5 µl liquid droplet (upper layer, '*U*') composed of water loaded with surfactants (C_S^U, 0.05 % v/v) was dispensed on the oleic acid droplet. The densities of the fluids were chosen in such a

manner that they ensured that the middle (upper) layer floats on the lower (middle) layer ($\rho_L > \rho_M > \rho_U$), as shown in the Table 5.1.

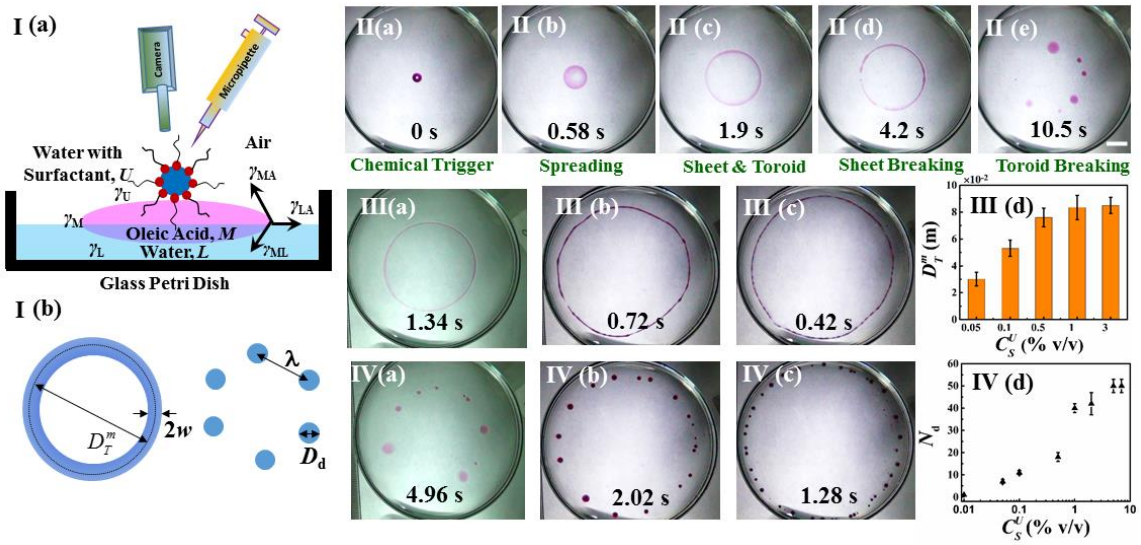

Figure 5.3. Image (I) schematically shows the experimental setup in which a glass petri dish was filled with a water layer (lower layer, *L*) and a droplet of oleic acid (middle layer, *M* and volume, ϕ_M = 20 µl) was dispensed on it. Thereafter, a chemical trigger (upper layer *U*, volume ϕ_U = 5 µl) of water droplet loaded with surfactants (C_S^U ,% v/v) was dispensed. The symbols γ_{ML}, γ_{MA}, and γ_{LA} denote the interfacial tensions in which the subscripts *M*, *L*, and *A* denote middle and lower layer, and the bounding fluid air, respectively. The symbols γ_U, γ_M, and γ_L denote the surface tension of the respective phases. Images II(a) – II(e) show the top view of the spatiotemporal evolution of the oleic acid droplet when C_S^U was 0.05 %. Images (a) initial configuration (0 s), (b) droplet spreading (0.58 s), (c) sheet and toroid formation (1.9 s), (d) toroid formation and breaking of sheet (4.2 s), and (e) droplets from toroid-braking (10.5 s) where the scale bar is 1 cm. The images III(a) – III(c) show the variation in the maximum diameter (D_T^m) of the toroid when C_S^U was, 0.1%, 0.5%, and 1%, respectively. Plot III(d) shows the variation in D_T^m with C_S^U . The images IV(a) – IV(c) show the variation in the number of droplets (N_d) formed due to the toroid-breaking when C_S^U was, 0.1%, 0.5%, and 1%, respectively. The plot IV(d) shows the variation in N_d with C_S^U .

The images II(a) and II(b) shows that the water loaded with surfactants led to the rapidly spreading of the oleic acid droplet. The system was chosen in such a manner that the configuration had the combination of surface tension as, $\gamma_L > \gamma_M > \gamma_U$, which resulted in a positive spreading coefficient, $S_{MUL} = \gamma_{UL} - \gamma_{MU} - \gamma_{ML} > 0$, suitable for the droplet spreading [63, 64]. The experimental and theoretical values of surface tension necessary for the calculation of spreading coefficients are provided in the Table 5.1. The images II(c) – II(e) suggest that the advancing front of the rapidly spreading droplet on the soft, deformable, and low friction oil-water interface formed a thin oleic acid sheet in the middle surrounded by a toroidal rim at the periphery. With time, the thin oil sheet in the middle broke away from the peripheral toroid, as shown by the image II(d) before the toroid Rayleigh-Plateau instability to form a collection of droplets, as shown by the image II(e). Interestingly, the size, shape, and stability of the toroid formed could be controlled by varying the surfactant loading (C_S^U) in the upper droplet. The images III (a) – (c) and plot III(d) show the increase in the toroidal diameter with increase in C_S^U. Further, the images IV(a) – (c) show increase in the number of droplets [N_d, plot IV(d)] and reduction in the average diameter [D_d, plot IV(e)] after the breaking of the toroid with increase in C_S^U. Importantly, the aforementioned methodology could be also employed to create toroids of fluids other than oleic acid such as silicone oil or hexadecane when the conditions $\rho_L > \rho_M > \rho_U$ and $\gamma_L > \gamma_M > \gamma_U$ were met.

In fact, the chemical trigger could also be changed from water loaded with surfactants. For example, we repeated the same experiment where a 5 µl n-pentanol droplet was dispensed as a chemical trigger on the 20 µl oleic acid droplet resting on water surface.

Again, the chosen fluids for this experiment ensured that, $\rho_L > \rho_M > \rho_U$ and $\gamma_L > \gamma_M > \gamma_U$ .Pentanol is a moderately volatile liquid, partially/sparingly soluble with water and oleic acid at room temperature, and well known for its surfactant like behavior, which enables its use as a co-surfactant to generate microemulsions [62, 65].

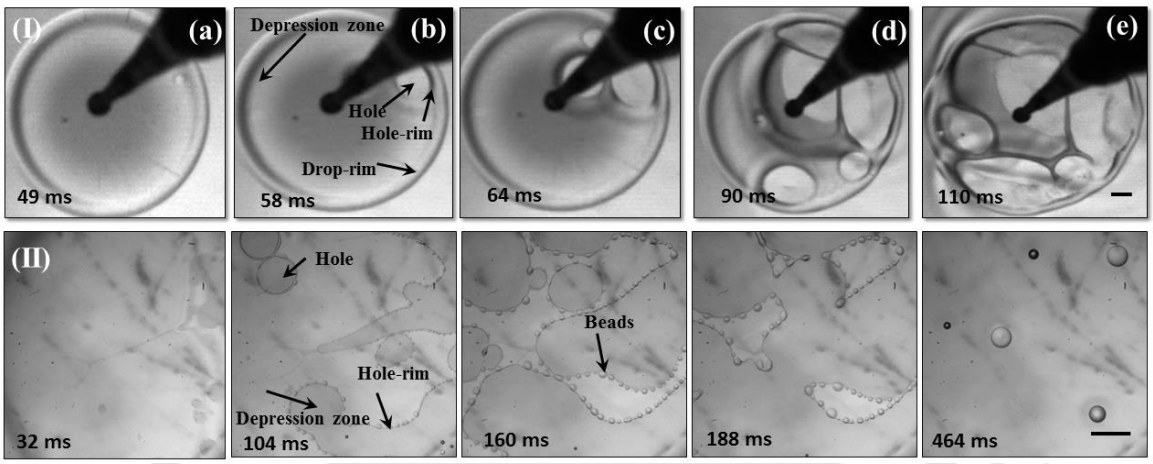

Figure 5.4. Images (a) – (e) in the row (I) show the steps to toroid formation of an oleic acid droplet (layer *M*) on water surface (layer *L*) with a pentanol trigger from the top (layer *U*). Images (a) – (e) show snapshots after 49 ms, 58 ms, 64 ms, 90 ms, and 110 ms, respectively, when ϕ_M = 20 µl and ϕ_U = 5 µl. The scale bar shown on the image I(e) is 1 cm. Images (a) – (e) in the row (II) show the time evolution of the magnified zone of an oil-sheet breakup under pentanol trigger after, 32 ms, 104 ms, 160 ms, 188 ms, and 46 ms, respectively, when μ_r = 27, ϕ_M = 1 µl and ϕ_U = 0.5 µl. The scale bar shown on the image II(e) is 1 mm.

Remarkably, the high speed high resolution video images I(a) – (e) in the Figure 5.4 show that pentanol trigger led to a series of interesting phenomena, in addition the events observed in the Figure 5.3. For example, in the beginning, addition of the pentanol trigger reduced the interfacial tension at the oleic acid and pentanol interface, which led to the rapid spreading of the oleic acid droplet, as shown in the image I(a). Following this, as the oleic acid droplet was stretched horizontally due to the rapid spreading, a thin sheet of oleic acid was formed at the central part surrounded by a toroidal drop-rim at the

boundaries. With time, a number of holes appeared near the drop-rim where a zone of depression was formed at junction of the central sheet and toroidal periphery, as shown by the images I(a) – I(c). Thereafter, the holes grew fast to achieve equilibrium contact angle and hole-rims coalesced with each other to form a network of oleic acid ribbons, as shown in the images I(c) – I(e). Finally, the drop-rim was completely detached from central part of the droplet to form an outer toroidal ring, which underwent Rayleigh-Plateau instability to form microdroplets. We could reproduce the aforementioned phenomenon for a number of other chemical triggers such as methanol, ethanol, and propanol.

The images II(a) – (e) and the captured the details of the dewetting of the oleic acid sheet on the water surface under microscope. The sheet breaking was initiated by the formation of holes due to the stretching of the sheet while the droplet spread on water surface. Interestingly the contact line near the dewetted liquid sheets possessed periodic 'beads', which were previously observed for the dewetting layers on the soft and slippery surfaces. The breaking of the oil-sheet showed some of the distinct features of the liquid sheet instabilities such as the destabilization due to oscillations and perforations alongside the unique rim-instabilities near the contact line, as reported previously. Figures 5.3 and 5.4 uncovered that the surfactant-water (SW) chemical trigger led to a much slower spreading and a symmetric toroid formation as compared to the much faster asymmetric toroid formation in case of the pentanol trigger. Figure 5.5 summarizes various characteristics of the reported phenomenon with the variation in the type of the chemical triggers, oil droplets, and the water sublayer. The plots (a) and (b) in this figure show the typical variation in the normalized diameter of the spreading front of the oil droplet, $\bar{d}_M = d_M / d_M^0$, with time (t) for the SW and pentanol triggers.

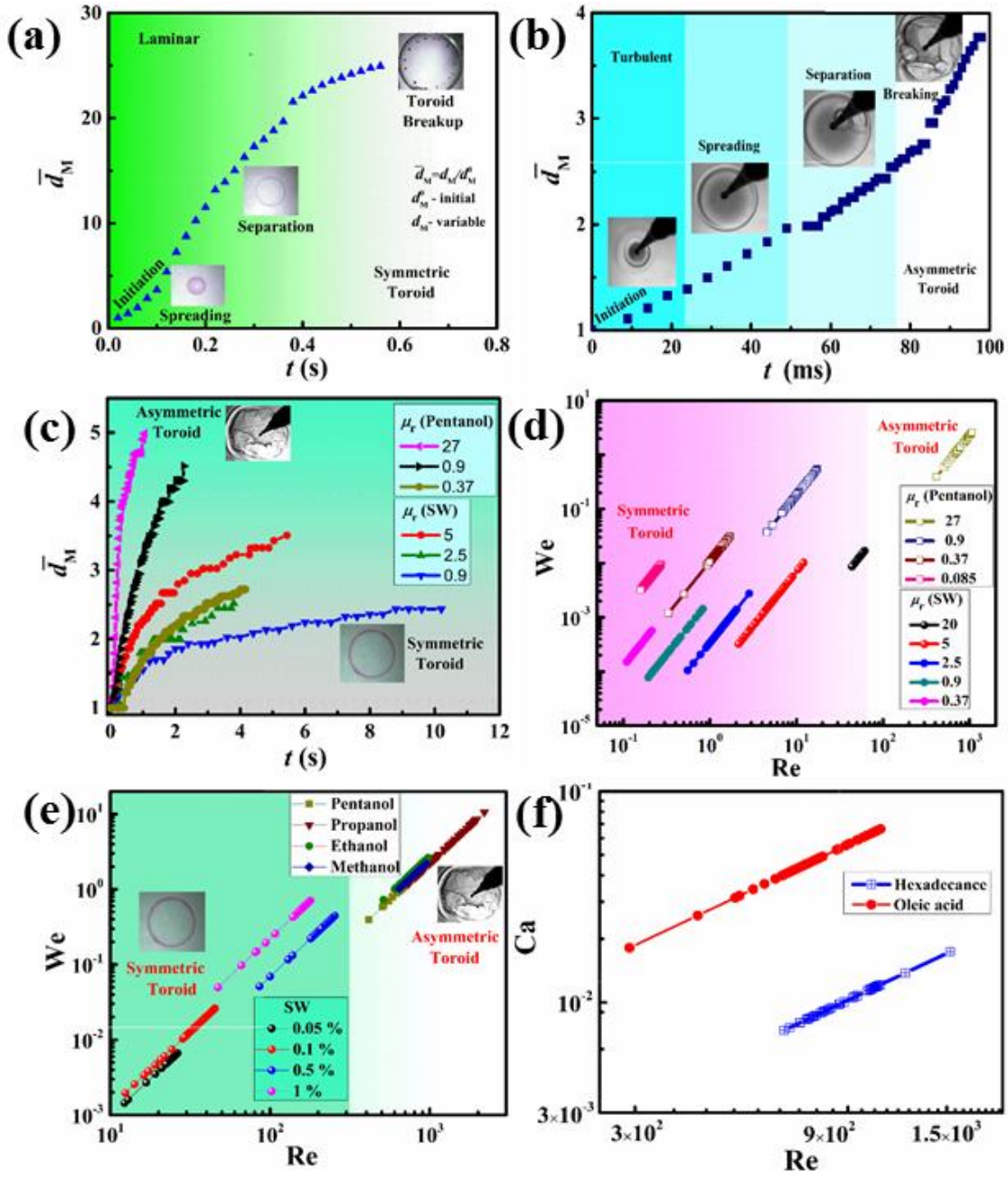

Figure 5.5. Plot (a) shows the variation of the normalized diameter of the spreading front of the oil droplet, $\bar{d}_M = d_M / d_M^0$, with time (t) for the surfactant-water (SW) chemical trigger when C_S^U was 0.5 %. Here d_M and d_M^0 are the variable and initial diameters of the oil droplet. Plot (b) shows variation of the $\bar{d}_M$ with t for the pentanol chemical trigger. Plot (c) shows the variation of the $\bar{d}_M$ with t when $\mu_r = \mu_M / \mu_L$ was varied for the chemical trigger, C_S^U = 0.5 % and pentanol. Plot (d) shows the variation in the Weber

number (We, $\rho_M v_M^2 d_M / \gamma_M$) with Reynolds number (Re, $\rho_M v_M d_M / \mu_M$) at different μ_r for the chemical trigger, C_S^U = 0.5 % and pentanol. Plot (e) shows the variation in We with Re for different chemical triggers such as C_S^U = 0.05% – 1%, methanol, ethanol, propanol, and pentanol. Plot (f) shows the variation in the capillary number (Ca, $\mu_M v_M / \gamma_M$) with Re for two different middle layers, hexadecane oil and oleic acid, with the chemical trigger pentanol. In all the plots, ϕ_M = 20 µl, ϕ_U = 5 µl, and μ_M = 1 mPa s and for plot (f), μ_L = 3 mPa s.

It may be noted here that we considered the maximum diameter of the oil droplet at a given time to experimentally determine the $\bar{d}_M$, which meant at the initial stages $\bar{d}_M$ was the diameter inclusive of the oil-sheet and the peripheral toroid while near the end it was the end-to-end diameter of the toroid. The plots show a non-monotonic variation in $\bar{d}_M$ with *t* at the different stages of the phenomenon, including, initiation, droplet spreading, sheet-toroid separation, sheet breakup and toroid breakup stages. While the system with pentanol trigger showed a much faster kinetics associated with the asymmetric breaking, the SW trigger showed a much slower kinetics. Interestingly, the plot (c) shows that introduction of glycerol to the water sub-layer could slow down the kinetics of the asymmetric droplet spreading (μ_r = 27) and transform the toroid formation mechanism into the symmetric one when μ_r = 0.37. In fact, the kinetics of the oil-droplet spreading and toroid formation became much slower even for the SW cases, as shown in the plots. Importantly, with the reduction in μ_r, the end-to-end diameter of the toroid formed (maximum value of $\bar{d}_M$) became much smaller, as shown in the plot (c). The viscosity of bottom fluid is influence the speed of the process and tune the number of droplets (N_d).

Further, we analyzed the dynamics of the oil layer with the help of the parameters such as the instantaneous spreading velocity (v_M), initial diameter (d_M^0), surface tension (γ_M), density (ρ_M), and dynamic viscosity (μ_M) of the oil-droplet, which led to the dimensionless Weber number (We, $\rho_M v_M^2 d_M^0 / \gamma_M$), Reynolds number (Re, $\rho_M v_M d_M^0 / \mu_M$), and the capillary number (Ca, $\mu_M v_M / \gamma_M$). In these calculations, the instantaneous spreading velocity (v_M) was evaluated from the variation in d_M at small time intervals Δt, from the plots (a) – (c). The plot (d) in the Figure 5.5 shows the typical variation in the Re with We when SW (C_S^U = 0.5 %) and pentanol triggers were employed and subsequently μ_r was reduced by introducing glycerol to water. The plot clearly shows the conditions where the drop spreading and toroid formation was symmetric and laminar flow regime (We < 0.1 and Re < 10), pseudo-symmetric and transition flow regime (0.1<We < 5 and 10 < Re < 100), and asymmetric and turbulent flow regime (We > 5 and Re > 100) [67-78]. The plot (e) in the Figure 5.5 shows the typical variation in the Re with We when the trigger was varied from SW with different surfactant loading to different types of alcohols such as methanol, ethanol, propanol and pentanol. Again, the plot shows the symmetric and laminar flow regime (We < 0.1 and Re < 10), pseudo-symmetric and transition flow regime (0.1<We < 5 and 10 < Re < 100), and asymmetric and turbulent flow regime (We > 5 and Re > 100) with the variation in the type of the chemical trigger. Further, plot (f) in the Figure 5.5 shows that replacing the oil droplet from more viscous oleic acid to less viscous hexadecane could lead to a faster spreading and toroid formation, which was reflected in the reduction of Ca and increase in Re.

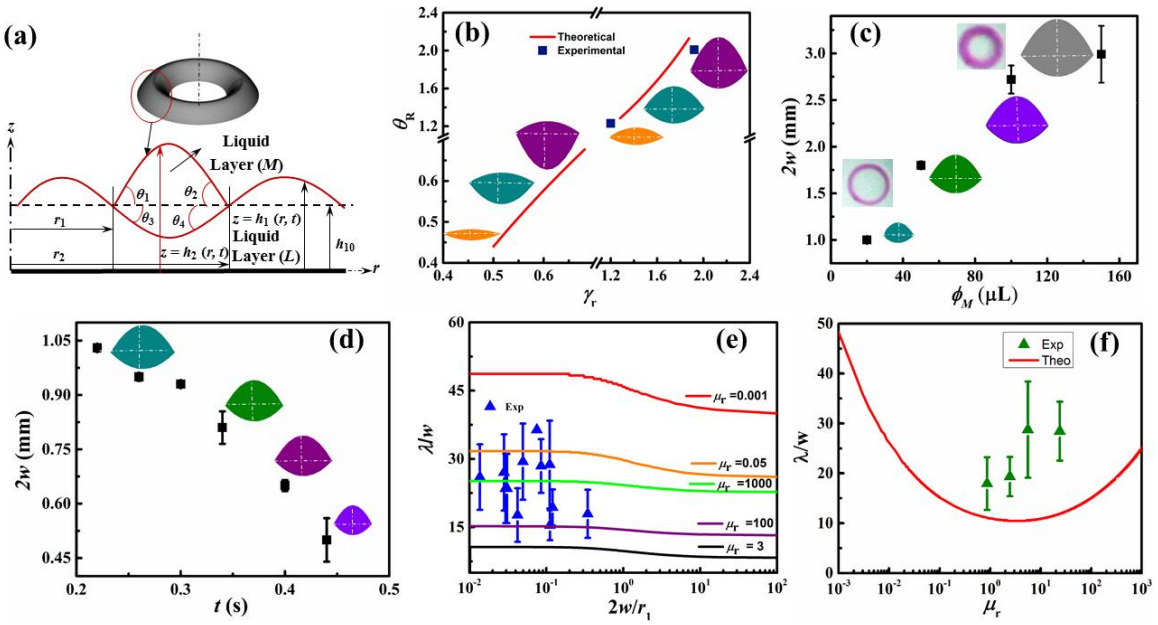

Figure 5.6. Front view or cross-sectional view of the toroid where the lower liquid layer (*L*) film and the combined lower and middle (*M*) liquid layer film thicknesses are denoted by h_1 (*r*, *t*) and h_2 (*r*, *t*), respectively. The mean film thickness of the lower layer is h_{10}. Inner and outer radii of the middle liquid layer are denoted by r_1 *and* r_2 (> r_1), respectively. The contact angles of the both middle and lower liquid layers with the mean lower film thickness at the inner edge [outer edge] are specified as θ_1 and θ_3 [θ_2 and θ_4], respectively. Image (a) show the Side view of the toroid and upper part and lower part of toroid at *45°*, Change Shape of the toroid in Plot (b) shows the contact ratio θ_r with the surface tension γ_R, Plot (c) Thickness verses height of the toroid varying with initial volume of ϕ_M = 20, 50, 100, 150 µl, μ_L=0.001 pa. s, ρ_L= 1000 kg/m^3, C_S^U = 0.5 %, ϕ_U=5µl, γ_{ML}= 48 and γ_{MA} =32 mN/m^2, Plot (d) show the experimental thickness of toroid different time evolution, μ_L=0.001 pa s, ρ_L= 1000 kg/m^3, γ_{ML}=48 and γ_{MA} =32 mN/m^2, C_S^U = 0.5 %, ϕ_M=20µl, ϕ_U=5µl, Plot (e) shows the spacing between the droplet for ratio of different thickness / toroid radius, Plot (f) shows the spacing between the droplet for different viscosity ratio ($\mu_r = \mu_M/\mu_L$).

Image 5.6 (a) schematically illustrates the front view geometry of the problem and introduces all important variables such as film thicknesses of the liquid layers, radii and

contact angles at the inner and the outer contact lines. Our aim to obtain theoretical radial thickness of the toroid, we have considered the base-state solutions of the two interfaces (L – M interface and M – air interface) introducing the following perturbations, $H_1(R,T) = H_{10}(R) + \varepsilon H'_{10}(R,T)$ and $H_2(R,T) = H_{20}(R) + \varepsilon H'_{20}(R,T)$, where $\varepsilon << 1$. The base states and imposing the zero film thickness condition [28] at the contact lines ($H_{20}|_{R_1} - H_{10}|_{R_1} = 0$ and $H_{20}|_{R_2} - H_{10}|_{R_2} = 0$), we have obtain the two equilibrium equations 5.2.7 and 5.2.8.

Along with the boundary conditions at fixed radii R_1 and R_2, contact angles of the both interfaces with mean lower film thickness at R_1 and R_2 can also be postulated as $dH_{20}/dR|_{R_1} = \tan\theta_1$, $dH_{10}/dR|_{R_1} = -\tan\theta_3$, $dH_{20}/dR|_{R_2} = -\tan\theta_2$, $dH_{10}/dR|_{R_2} = \tan\theta_4$. We have solved the equation (5.2.7) and (5.2.8) together with the boundary conditions stated above are solved numerically by employing the commercial package Mathematica™. Image 5.6 (a) shows the side view of the toroid which is calculated by the equation (5.2.7) and (5.2.8) where we have observed toroid upper part and lower part have different shapes, which is dependent upon the surface tension of three layer. In plot 5.6 (b-d) show the inserted images which shows different shapes of the toroid with time evolution for different interfacial tension, different volume and different time at 0.5 % surfactant of U layer on M layer and reaching the equilibrium thickness which further fragmented into small segments and to form droplets. The toroid expands until it does no reach equilibrium thickness when $G = \Delta\gamma \cdot A > 1$. Here G is Gibbs free energy, $\Delta\gamma$ is change in surface tension, A is surface area of toroid. Toroid is stable or in equilibrium condition where Gibbs free energy $G < 1$ [79].

During the experiment, there are several possible configurations of toroid, which depend upon the surface tension of all the three mediums. Plot 5.6 (b) shows the variation of the contact ratio $\theta_r = \theta_1/\theta_3$ with the surface tension ratio ($\gamma_R = \gamma_1/\gamma_2$). The plot indicates the cross section of the toroid changes from oblate, prolate, rugby ball to pear shapes under different conditions [80]. Plot 5.6 (c) shows that the thickness ($2w$) of the toroid changes with varying initial volume ϕ_M, as observed in the experiments. Plot 5.6 (d) shows that the decrease in the thickness of the toroid ($2w$) with time (t) for 0.5 % surfactant water in *U* layer on *M* layer, which is also found to be comparable with the experimental results. Plot 5.6 (e) show the ratio (λ/w) of spacing between the generated droplets and thickness of toroid for ratio ($2w/ r_1$) of different thickness and initial radius (r_1) of the toroid. Plot 5.6 (f) show the ratio (λ/w) of spacing between the generated droplet and thickness of toroid for different viscosity ratio (μ_r) of the between *M* layer and *L* layer. The theoretical results are almost similar to the experimental results for different viscosity ratio (μ_r).

The rows (I) – (III) in the Figure 5.7 shows the spatiotemporal variation in the flow morphologies when the surfactant loading inside the SW chemical trigger was varied. While the columns correspond to the surfactant loading of 0.01%, 0.05%, 0.1%, 0.5%, and 1%, respectively, the images in the row (I) corresponds to the initial state, row (II) corresponds to the maximum diameter of the toroid (D_T^m), and the row (III) corresponds to droplets formed after the toroid breaks. The images (f) – (g) show spacing between the droplets (λ/w), (λ/r) reduced, and average diameter of the droplets (D_d) reduced with the variation in C_S^U .

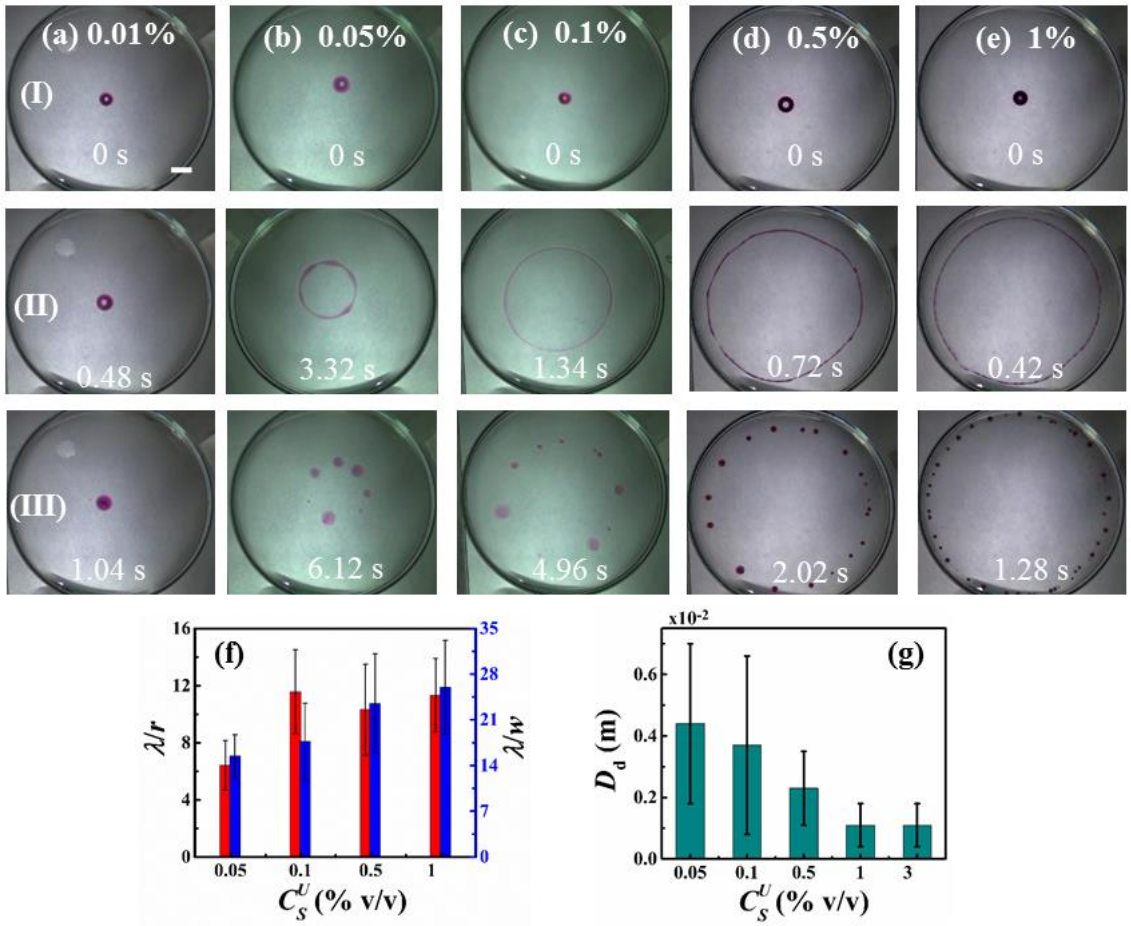

Figure 5.7. Images in the columns (a) – (e) show the snapshots of the time evolution of a toroidal object when the surfactant concentration (C_S^U, % v/v) was varied from 0.01% – 1% in the SW chemical trigger (surfactant loaded water droplet, ϕ_U = 5 µl). The rows (I) – (III) show the introduction of the chemical trigger, the maximum diameter of the toroid formed, and breaking of the toroid into droplet, respectively. The respective time for evolution are shown on the images. The volume of the oleic acid middle layer was kept constant at, ϕ_M =20 µl in all the experiments. The images (f) – (g) show the variations in the normalized spacing between the droplets, λ/w and λ/r alongside the average diameter of the droplets (D_d) due to the breakup of the oil-toroid with C_S^U. In this figure, the parameter, λ/w, is ratio of the dimensional distance between the droplets to the radius of the oil-toroid of diameter, 2w. The parameter, λ/r, is ratio of the dimensional distance between the droplets to the radius of the oil-droplet, r, after breakup of the toroid. The scale bar shown in the image I(a) corresponds to 1 cm.

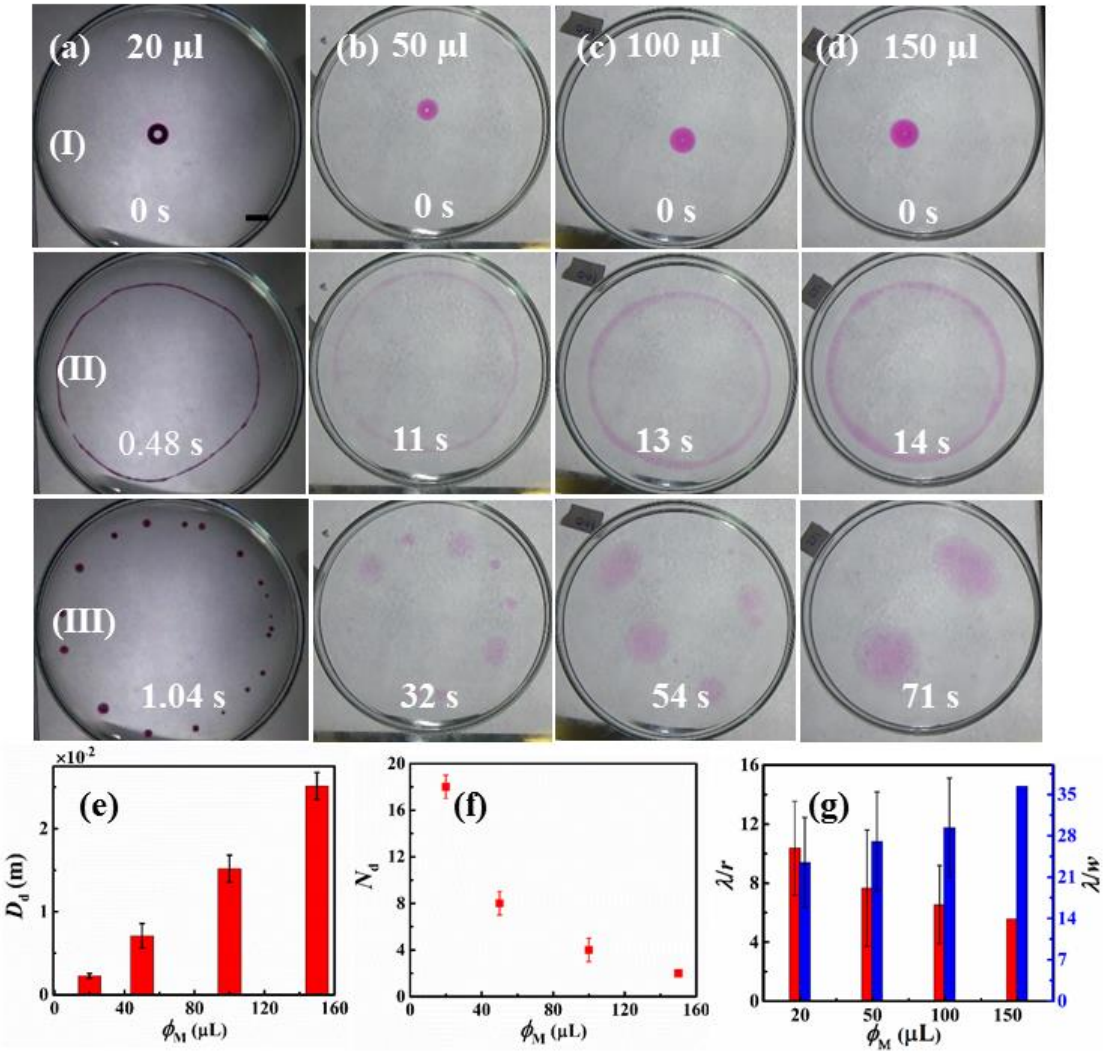

Figure 5.8. Images in the columns (a) – (d) show the snapshots of the time evolution of a toroidal object when ϕ_M was varied from 20 – 150 µl keeping the SW trigger volume ϕ_U = 5 µl and C_S^U = 0.5% v/v. The rows (I) – (III) show the introduction of the chemical trigger, the maximum diameter of the toroid formed, and breaking of the toroid into droplet, respectively. The images (e) – (g) show the variations in D_d, N_d, λ/w, and λ/r with ϕ_M. The scale bar shown in the image I(a) corresponds to 5 mm.

The rows (I) – (III) in the Figure 5.8 shows the spatiotemporal variation in the droplet morphologies when C_S^U = 0.5% v/v and the oil droplet volume ϕ_M was varied from 20 – 150 µL, as shown on the image (a) – (d). The images in the row (I) corresponds to the

initial state, row (II) corresponds to the maximum diameter of the toroid (D_T^m), and the row (III) corresponds to droplets formed after the toroid breaks. The images (e) – (g) show average diameter of droplet (D_d), number of droplet (N_d) and spacing between the droplets (λ/w), (λ/r) reduced with the variation in C_S^U .

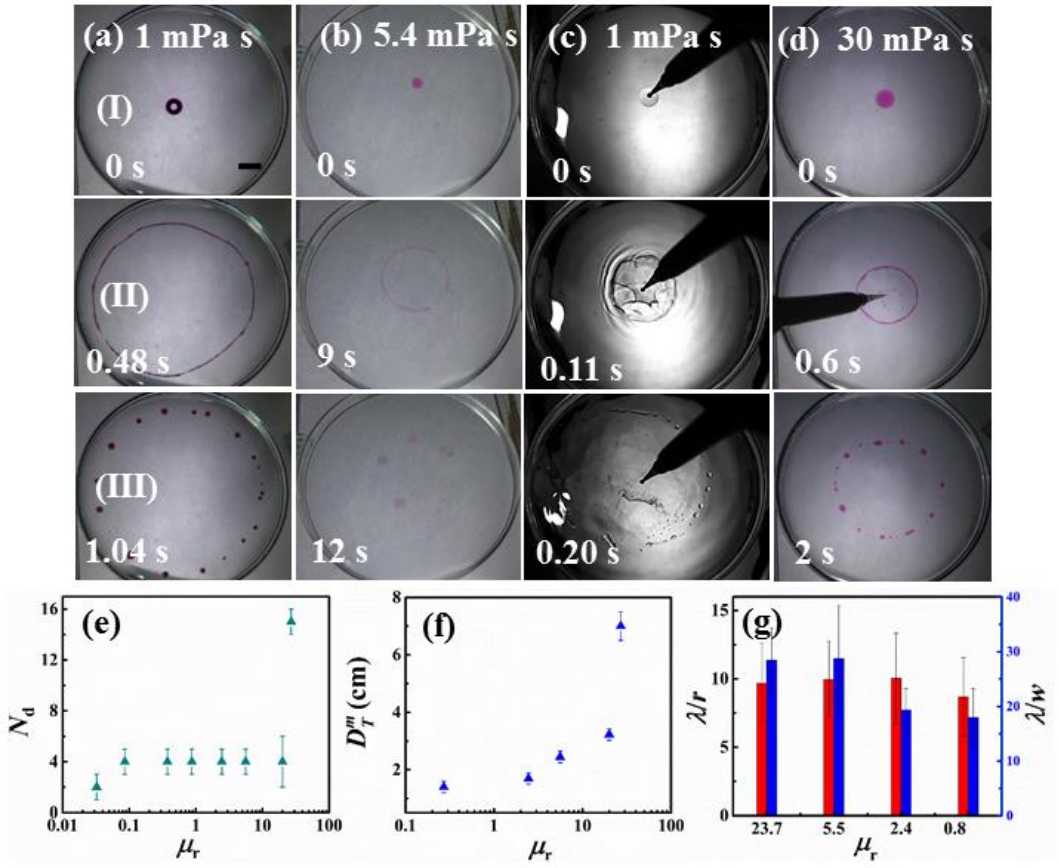

Figure 5.9. Images in the columns (a) – (b) show the snapshots of the time evolution of a toroidal object when μ_r was varied from 27 and 5 keeping the SW trigger volume ϕ_U = 5 µl and ϕ_M = 20 µl. Images in the columns (b) – (d) show the snapshots of the time evolution of a toroidal object when μ_r was varied from 27 and 0.9 keeping the pentanol trigger volume ϕ_U = 5 µl and ϕ_M = 20 µl. The rows (I) – (III) show the introduction of the chemical trigger, the maximum diameter of the toroid formed, and breaking of the toroid into droplet, respectively. The images (e) – (g) show the variations in N_d, D_T^m, λ / w, and λ / r with μ_r for surfactant trigger (C_S^U ,0.5% v/v). The scale bar shown in the image I(a) corresponds to 5 mm.

We observe that the torus can break via Rayleigh-Plateau instabilities to form a number of spherical droplets depends upon the *L* layer of viscosity as shown by the series of images in Figure 5.9 (a-d). The first row of image corresponds to the initial state, right after the surfactant droplet is dropped, the second row of image corresponds to a time slightly before break up, and the third row of images corresponds to the end of the process, right after break up had occurred. The image 5.9 (a-b) in I-III row show the change in the size of the toroid with the change of viscosity (μ_r) where the trigger by the surfactant. In the image 5.9 (c-d) I-III row show the asymmetric to symmetric toroid of the droplet with (μ_r) where the trigger by the surfactant. We obtained the different range of number of droplet (N_d) for viscosity of *L* layer as shown in Figure 5.9 (e). The viscous force restricts the fast spreading of the droplet and also decrease the generated number of droplets. For the low viscous ratio μ_r have decrease the diameter of the toroid as shown in Plot 5.9 (f). The plot (g) shows spacing between the droplets (λ/w), (λ/r) with the variation in μ_r . After spreading of the droplet, a sheet is formed which further generated the holes. These number of holes (N_h/A) per unit area were increased upto 46 ms after that these holes collapses and create different segments with further form a sheets as shown in Plot 5.10 (a) and image 5.4 (b).

Plot 5.10 (b) shows the number of droplets per unit area (N_d/A) of different droplet size (D_d) of oil generated which is best way to produce one shot emulsification of the droplet. Plot 5.10 (c) and image 5.4 (c) are showing the number of beads per unit length (N_b/L_c) for different time scale. The beads are merging with the time increase and finally form a drop as shown in image 5.3 (e). Plot 5.10 (d) and image 5.4 II(b) shows the growth rate of these holes (R_h) which is grow upto 1 μm to 200 μm within 70 ms.

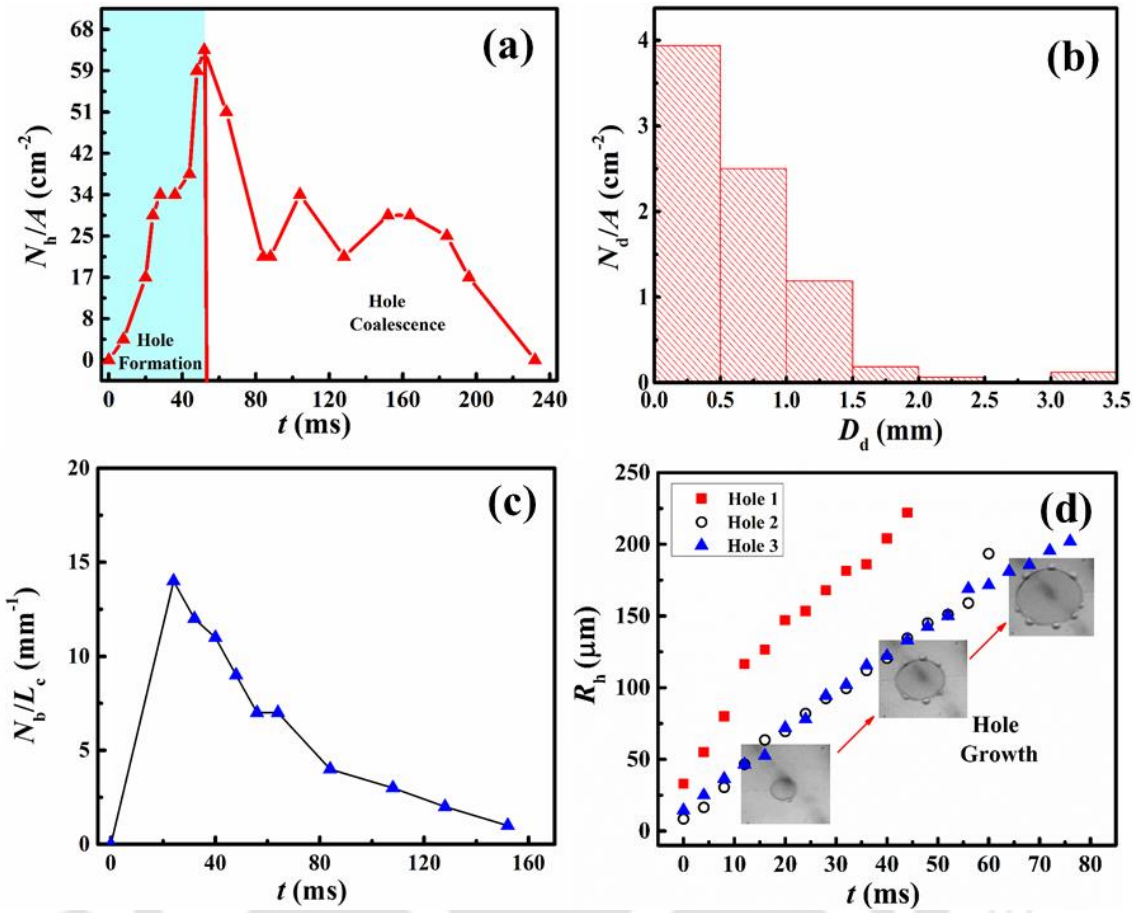

Figure 5.10. The plot (a) shows the variation in the number density of holes (N_h / A) with t when the oil-sheet and oil-toroid separate from each other under the pentanol trigger scale, as shown in the row (I) of the figure 5.3. The plot (b) shows the typical number of droplets per unit area (N_d / A) and their average size (D_d) distribution due to the breakup of the oil-sheet, as shown in the row (I) of the figure 5.3. The plot (c) shows the variation in the number of beads per unit length of the contact line (N_b / L_c) with t when the oil-sheet dewet the water-sublayer, as shown in the row (II) of the figure 5.3. The plot (d) shows the variation in the hole-radius (R_h) with time t for three different holes when the oil-sheet dewet the water-sublayer, as shown in the row (II) of the figure 5.3. The experimental conditions for this plot was kept similar to as mentioned in the row (II) of the figure 5.3 as, μ_r = 27, ϕ_M =1 μl, and ϕ_U = 0.5 μl.

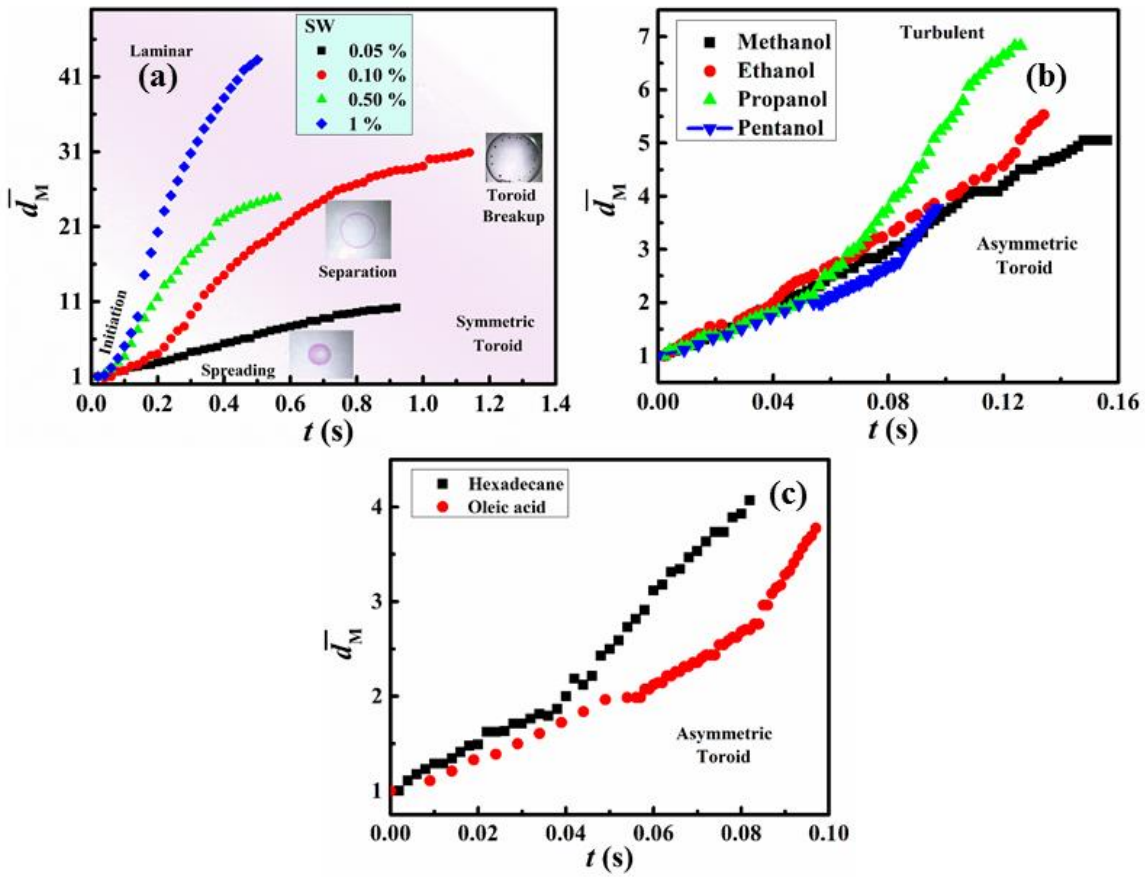

Figure 5.11. Plot (a) shows the variation of the normalized diameter of the spreading front of the oil droplet, $\bar{d}_M = d_M / d_M^0$, with time (t) for the SW chemical trigger when C_S^U was varied from 0.05% to 1 %. Plot (b) shows variation of the $\bar{d}_M$ with t for the methanol, ethanol, propanol, and pentanol chemical triggers. Plot (c) shows variation of the $\bar{d}_M$ with t when the middle fluid was altered from oleic acid to hexadecane and the chemical trigger was pentanol. In all the experiments, μ_r = 27, ϕ_M =20 µl, and ϕ_U = 5 µl whereas in the plot (c), μ_r = 3 for hexadecane system.

Plot 5.11. (a) and Images 5.3 (b) show the diameter growth of the drop to toroid formation ($\bar{D}$) which are for different surfactant water composition (C_S^U) of upper layer. Initially, drop become unstable and form sheet which further sheets break and form the toroid which breaks and generate the droplets as shown Images 5.3 (b). Plot 5.11 (b) shows the diameter growth ($\bar{D}$) of the drop to toroid formation which is for different

alcohol (C^U) of upper layer which shows this system is very fast and breaking is unstable and generate many number of droplet as shown in Plot 5.10 (c). Plot 5.11 (c) shows the diameter growth of the drop to toroid formation which is for different oil (C_M).

5.4 SUMMARY

In summary, we investigate breaking of oil droplet on a water surface stimulated by an external chemical trigger such as a surfactant. The breaking phenomena is controlled by the kinetic parameters such as viscosity and thermodynamic parameters such as the droplet size, surface tensions of the fluids or the surfactant loading in the chemical trigger. The droplet breaking is in the slow laminar regime when the fluids are highly viscous whereas a turbulent breakup is observed for the case when the fluids are of low viscosity. We show that the tuning of the laminar to turbulent regimes are possible by tuning the various thermodynamic and kinetic process parameters. Phase diagrams are presented to show the different regimes of droplet breakup such as spreading, sheet and toroid formation, toroid expansion, sheet breakup, toroid breakup, and microdroplet formation. The study highlights a new phenomena associated with toroid formation on soft surface in absence of any rotational influence.

REFERENCES

1. R. K. McGeary, *J. Am. Ceram. Soc.*, 1961, **44**, 513-522.
2. S. Kumar, A. K. Singh, A. K. Dasmahapatra, T. K. Mandal, and D. Bandyopadhyay, *Carbon*, 2015, **89**, 31-40.
3. A. Bala Subramaniam, M. Abkarian, L. Mahadevan, and H. A. Stone, *Nature*, 2005, **438**, 930.
4. W. Wang, W. Duan, A. Sen, and T. E. Mallouk, *Proc. Natl. Acad. Sci. U.S.A*, 2013, **110**, 17744-17749.
5. A. Arinstein, M. Burman, O. Gendelman, and E. Zussman, *Nat. Nano*, 2007, **2**, 59-62.

6. B. Song, B. Liu, Y. Jin, X. He, D. Tang, G. Wu, and S. Yin, *Nanoscale*, 2015, **7**, 930-935.
7. S. H. Kang, B. Pokroy, L. Mahadevan, and J. Aizenberg, *ACS Nano*, 2010, **4**, 6323-6331.
8. Cyril Isenberg, The Science of Soap Films and Soap Bubbles,1978.
9. L. V. Zhang, J. Toole, K. Fezzaa, and R. D. Deegan, *J. Fluid Mech.*, 2012, **690**, 5-15.
10. D. T. Papageorgiou, *Phys. Fluids*, 1995, **7**, 1529-1544.
11. E. Pairam and A. Fernández-Nieves, *Phys. Rev. Lett.*, 2009, **102**, 234501:1-4.
12. S. Yun and G. Lim, *J. Fluid Mech.*, 2014, **752**, 266-281.
13. T. J. Pedley, *J. Fluid Mech.*,1968, **32**, 97-112.
14. K. Marten, K. Shariff, S. Psarakos, and D. J. White, *Sci. Am. (Int. Ed.)*, 1996, **275,** 82-87.
15. M. J. Urban, P. K. Dutta, P. Wang, X. Duan, X. Shen, B. Ding, Y. Ke, and N. Liu, *J. Am. Chem. Soc.*, 2016, **138**, 5495-5498.
16. R. Gunn and G. D. Kinzer, *Journal Meteorol.*, 1949, **6**, 243-248.
17. S. Hu and R. C. Kinter, *AIChE Journal*, 1955, **1**, 42-48.
18. M. K. Tripathi, K. C. Sahu, and R. Govindarajan, *Sci. Rep.*, 2014, **4**, 4771:1-9.
19. R. Clift, J. R. Grace and M. E. Weber, Bubbles, Drops and Particles (Academic, New York, 1978).
20. Y. C. Jung and B. Bhushan, *Langmuir*, 2008, **24**, 6262-6269.
21. F. Zoueshtiagh, H. Caps, M. Legendre, N. Vandewalle, P. Petitjeans, and P. Kurowski, *Eur. Phys. J. E*, 2006, **20**, 317-325.
22. S. Kumar, B. Sarma, A. Dalal, D. Basu, A. K. Dasmahapatra and D. Bandyopadhyay, *Farad. Discuss.*, 2017, **199**, 115-128.
23. R. J. A. Hill and L. Eaves, *Phys. Rev. Lett.*, 2008, **101**, 1-4.
24. J. Plateau, Experimental and Theoretical Statics of Liquids Subject to Molecular Forces (Gauthier-Villars, Paris, 1873).
25. E. M. Terentjev, *Nat. Mater.*, 2002, **1**, 149-150.
26. J. M. Long, X. Qin and G. F. Wang, *J. Appl. Phys.*, 2015, **117**, 054310:1-6.
27. R. A. Brown and L. E. Scriven, *Proc. R. Soc. Lond. A Math. Phys. Engg. Sci.*, 1980 **371**, 331-357.
28. A. G. González, J. A. Diez and L. Kondic, *J. Fluid Mech.*, 2013, **718**, 246-279.

29. S. H. Davis, *J. Fluid Mech.*,1980, **98**, 225-242.
30. E. Pairam, J. Vallamkondu, V. Koning, B. C. van Zuiden, P. W. Ellis, M. A. Bates, V. Vitelli, and A. Fernandez-Nieves, *Proc. Natl. Acad. of Sci.*, 2013, **110**, 9295-9300.
31. A. A. Fragkopoulos, E. Pairam, E. Berger, P. N. Segre, and A. Fernandez-Nieves, *Proc. Natl. Acad. of Sci.*, 2017, **114**, 2871-2875.
32. A. Oron, S. H. Davis, and S. G. Bankoff, *Rev. Mod. Phys.*, 1997, **69**, 931-980.
33. R. V. Craster and O. K. Matar, *Rev. Mod. Phys.*, 2009, **81**, 1131-1198.
34. G. Reiter, *Phys. Rev. Lett.*, 1992, **68**, 75-78.
35. A. Sharma, *Langmuir*, 1993, **9**, 861-869.
36. J. Bischof, D. Scherer, S. Herminghaus, and P. Leiderer, *Phys. Rev. Lett.*, 1996, **77**, 1536-1539.
37. R. Xie, A. Karim, J. F. Douglas, C. C. Han, and R. A. Weiss, *Phys. Rev. Lett.*,1998, **81**, 1251-1254.
38. A. Sharma and R. Khanna, *Phys. Rev. Lett.*, 1998, **81**, 3463-3466.
39. S. Herminghaus, K. Jacobs, K. Mecke, J. Bischof, A. Fery, M. Ibn-Elhaj, and S. Schlagowski, *Science*, 1998, **282**, 916-919.
40. R. Konnur, K. Kargupta, and A. Sharma, *Phys. Rev. Lett.*, 2000, **84**, 931-934.
41. U. Thiele, M. G. Velarde, and K. Neuffer, *Phys. Rev. Lett.*, 2001, **87**, 016104:1-4.
42. L. Brusch, H. Kühne, U. Thiele, and M. Bar, *Phys. Rev. E*, 2002, **66**, 011602:1-5.
43. N. Chiara, R. E. Drew, B. Elmar, B. Hans-Jurgen, and S. J. C. Vincent, *Rep. Prog. Phys.*, 2005, **68**, 2859.
44. D. Bandyopadhyay, R. Gulabani, and A. Sharma, *Ind. & Engg. Chem. Res.*,2005, **44**, 1259-1272.
45. D. Bandyopadhyay and A. Sharma, *J. Chem. Phys.*, 2006, **125**, 054711:1-13.
46. K. Kargupta and A. Sharma, *Phys. Rev. Lett.*, 2001, **86**, 4536-4539.
47. A. A. Nepomnyashchy, A. A. Golovin, A. E. Tikhomirova, and V. A. Volpert, *Phys. Rev. E*, 2006, **74**, 021605:1-10.
48. R. Mukherjee, D. Bandyopadhyay, and A. Sharma, *Soft Matter*, 2008, **4**, 2086-2097.
49. A. Sehgal, D. Bandyopadhyay, K. Kargupta, A. Sharma, and A. Karim, *Soft Matter*, 2012, **8**, 10394-10402.
50. M. Ghezzi, S. C. Thickett, and C. Neto, *Langmuir*, 2012, **28**, 10147-10151.
51. A. Verma and A. Sharma, *Macromolecules*, 2011, **44**, 4928-4935.

52. N. Bhandaru, A. Das, N. Salunke, and R. Mukherjee, *Nano Letters*, 2014, **14**, 7009-7016.

53. M. Ghezzi, P. Y. Wang, P. Kingshott, and C. Neto, *Adv. Mater. Interfaces*, 2015, **2,** 1-10.

54. B. Ravi, R. Mukherjee, and D. Bandyopadhyay, *Soft Matter*, 2015, **11**, 139-146.

55. S. Peng, D. Lohse, and X. Zhang, *ACS Nano*, 2015, **9**, 11916-11923.

56. J. M. P. Gutierrez, T. Hinkley, J. W. Taylor, K. Yanev, and L.Cronin, *Nature Commoun.*, 2014, **5**, 1-8.

57. J. R. Tumbleston, D. Shirvanyants, N. Ermoshkin, R. Janusziewicz, A. R. Johnson, D. Kelly, K. Chen, R. Pinschmidt, J. P. Rolland, A. Ermoshkin, E. T. Samulski, and J. M. DeSimone, *Science*, 2015, **347**, 1349-1352.

58. A. Koh, D. Kang, Y. Xue, S. Lee, R. M. Pielak, J. Kim, T. Hwang, S. Min, A. Banks, P. Bastien, M. C. Manco, L. Wang, K. R. Ammann, K. I. Jang, P. Won, S. Han, R. Ghaffari, U. Paik, M. J. Slepian, G. Balooch, Y. Huang, and J. A. Rogers, *Sci. Transl. Med.*, 2016, **8**, 1-13.

59. L. Mazutis, J. Gilbert, W. L. Ung, D. A. Weitz, A. D. Griffiths, and J. A. Heyman, *Nat. Protocols*, 2013, **8**, 870-891.

60. S. Kumar, M. R. Ali Faridi, A. K. Dasmahapatra, and D. Bandyopadhyay, *RSC Adv.*, 2016, **6**, 107049-107056.

61. P. Dubois, G. Marchand, Y. Fouillet, J. Berthier, T. Douki, F. Hassine, S. Gmouh, and M. Vaultier, *Anal. Chem.*, 2006, **78**, 4909-4917.

62. E. A. van Nierop, A. Ajdari, and H. A. Stone, *Phys. Fluids*, 2006, **18**, 038105:1-4.

63. J. N. Israelachvili, Intermolecular and Surface Force (Academic Press, London, 1992).

64. C. J. Van Oss, M. K. Chaudhury, and R. J. Good, *Chem. Rev.*, 1988, **88**, 927-941.

65. F. Comelles and J. Sanchez Leal, *J. Disper. Sci. Technol.*, 1998, **19**, 521.

66. N. Dombrowski and R. P. Fraser, *Phil. Trans. R. Soc. Lond. A*, 1954, **247,** 101-130.

67. J. Wang, M. Do-Quang, J. J. Cannon, F. Yue, Y. Suzuki, G. Amberg, and J. Shiomi, *Sci. Rep.*, 2015, **5**, 8474:1-7.

68. A. S. Mohamed, M. A. Herrada, A. M. Gañán-Calvo, and J. M. Montanero, *Phys. Rev. E*, 2015, **92**, 1-6.

69. R. D. Deegan, P. Brunet, and J. Eggers, *Nonlinearity*, 2008, **21**, C1-C11.

70. X. Deng, F. Schellenberger, P. Papadopoulos, D. Vollmer, and H.-J. Butt, *Langmuir*, 2013, **29**, 7847-7856.

71. J. S. Lee, S. J. Park, J. H. Lee, B. M. Weon, K. Fezzaa, and J. H. Je, *Nat. Commun.*, 2015, **6,** 1-8.

72. L. V. Zhang, J. Toole, K. Fezzaa, and R. D. Deegan, *J. Fluid Mech.*, 2012, **690**, 5-15.

73. B. Derby, *Annu. Rev. Mater. Res.*, 2010, **40**, 395-414.

74. C. Josserand and S. T. Thoroddsen, *Annu. Rev. Fluid Mech.*, 2016, **48**, 365-391.

75. T. Tran, H. J. J. Staat, A. Prosperetti, C. Sun, and D. Lohse, *Phys. Rev. Lett.*, 2012, **108**, 036101:1-5.

76. E. Villermaux and B. Bossa, *J. Fluid Mech.*, 2011, **668**, 412-435.

77. H. Lastakowski, F. Boyer, A. L. Biance, C. Pirat, and C. Ybert, *J. Fluid Mech.*, 2014, **747**, 103-118.

78. K. Willis and M. Orme, *Exp. Fluids*, 2003, **34**, 28-41.

79. R. Yanashima, A. A. Garcia, J. Aldridge, N. Weiss, M. A. Hayes, and J. H. Andrews, *PLoS ONE*, 2012, **7**, 1-6.

80. C. J. Lister and J. Butterworth, *Nature*, **497**, 190-191.

Chapter 6

Summary and scope for future work

6.1 SUMMARY

In the present thesis, we have described a host of interesting behaviors related to a number of solid and soft motors. The solid motors were prepared using glass beads coated with the smart materials such as graphene whereas the soft motors were synthesized from water or oil loaded with functional materials. Further, the dynamics of the non-deformable solid and deformable liquid motors were studied under the influence by external field, chemical potential gradient, surface tension force, Lorenz force, electrical and magnetic fields. The dynamics of prototypes developed have also been supported with the theoretical calculation using Neumann construction force surface tension, Lorenz force, drag force, Stokes-Einstein equation and stability analysis. The major conclusions from the study are summarized chapter wise.

Multifunctional graphene superbots for chemo-magneto-galvanotaxis

- The RGO superbots were responsive towards the electrical, magnetic, and chemical triggers.
- The chemical locomotion recorded a maximum speed ~13 body lengths per second, the external magnetic field could move the motor at a speed many fold larger than the chemical trigger. The RGO microbots under electrical field across the electrode was also shown directional motion on the water surface. The superbots also shows the both control motion by magnetic and pH taxis.
- The microbot performed interesting task such as ‘approach’, ‘attach’, ‘drag’, and ‘drop’ of polymeric inert payloads of ~1000 times heavier and ~13 times bigger in size.

- This superbots could find important applications in clinical restoration of stenotic blood vessels, cleaning of blockages in blood vessels, drug delivery, and diverse bio-carriers.

Magnetically guided push-pull motility of liquibots for drug-delivery

- The attractive (repulsive) of paramagnetic (diamagnetic) salt laden liquibots were show motion under remotely magnetic guidance.
- The paramagnetic (diamagnetic) waterbot could migrate, ~8 body length/s (~ 1 body length/s) under remote magnetic guidance, which could further be increased by enhancing the strength of the external magnetic field.
- The waterbot was split into many smaller parts on an oil coated solid surface and then arranged in the shapes of polygons.
- A liquibot based 'Packman'^{TM} game was also demonstrated on the slippery solid surfaces under the varying magnetic guidance.
- This liquibots experiments is suitable in diverse droplet microfluidic applications.

Electric field induced spreading, oscillation, ejection, spinning, and breaking of oilbots

- Instead of the electrowetting on solid surface, the droplet showed spreading, oscillation, and ejection motions on the slippery (water) beyond a critical limit of the electric field.
- Smaller and less viscous droplets showed speed of ejection as high as ~5 body length per second owing to the lower drag force at the oil-water interface.

- A simple theoretical model based energy equations corresponding to the Neumann's triangle modified with the electric field component has been proposed to theoretically calculate the change in the contact angle of the droplet and the subsequent change in the diameter during spreading.
- The EWOL setup on a permanent magnet could engender interesting both (clockwise and anticlockwise) direction rotational motion, which was attuned to the change in the electric or magnetic field intensity and direction.
- A simple theoretical model based on Stokes flow could explain the Lorentz force induced rotational motion of the oil droplet. Increasing the speed of rotation led to the spreading of the droplet under the influence of the centripetal force, which in conjunction with the EHD stress at the oil-water interface led to the cohesive failure of the droplet to form a number of miniaturized ones.
- The reported oscillatory and rotational motions of the incompressible droplet could be employed as stirrers or impellers inside the microfluidics devices for mixing or pumping applications.

Self-organized superspreading of droplets to form fluid-toroids

- The oil droplet forms a lens on water surface which follows the Neumann tringle, which became unstable by the varying of the surface tension of layers.
- By surfactant or alcohol trigger, oil droplet deformed with elliptical to sheet, sheet to toroid, and generated daughter droplets.
- The laminar to turbulent dynamics of oil layer was influence with viscosity and surface tension of three layer of which further explained by dimensionless numbers, $\bar{D}$, We, Ca, and Re number.

- The linear stability analysis provides the basis for the cross-sectional shapes of the toroid with change in the process parameters. The experimental spacing between the droplet on the slipping surface was compared and contrasted with the help of linear stability analysis.

6.2 FUTURE SCOPE OF RESEARCH

In this thesis, the presented work can be extended in many different ways. Some of the interesting systems are as follows.

- The work in Chapter 2 explains how graphene based superbot shows the controlled motion under different external fields. In future, the exploration and synthesis of the other 2D material like MoS_2, phosphorene, silicene and single molecule can be used for micro/nanomotor with the biocompatibility to human body. The miniaturization of the size of the microbot into nanobots can facilitate motions under ultrasonication, infrared, X-rays, and light.
- The work in Chapter 3 shows the pull and push motion of paramagnetic and diamagnetic salt loaded water droplet under magnetic field. In future, the miniaturized the size of droplet, Janus liquibots, and active droplets can be synthesized and used for microfluidic application. These liquibots can be used as a microreactor and sensors.
- Chapter 4 details in explaining the deformation of oil droplet on slippery surface under electric and electromagnetic field. In this regard, the magnetic particle laden oil can also give different types of deformation under external field, applicable for electrospraying, pumping, mixing and drug delivery.
- Summarizing Chapter 5 shows an external trigger to a floating oil drop on the slippery surface can generate miniaturized droplets. During this

phenomena, the work done can be employed for harvesting high density power. Instead of the oil and water, studies on the active fluids can be the next step to explore the hydrodynamics of the complex fluids.

6.3 PUBLICATIONS AND CONFERENCES

6.3.1 Publications

1. **S. Kumar**, A. K. Singh, A. K. Dasmahapatra, T. K. Mandal, D. Bandyopadhyay, Graphene based multifunctional superbots. ***Carbon,*** 2015, **89**, 31-40.
2. **S. Kumar**, Md. Rashid Ali Faridi, A. K. Dasmahapatra, T. K. Mandal, D. Bandyopadhyay**,** Magnetic field Induced push-pull motility of liquibots**,** ***RSC Advance***, 2016, **6**, 107049-107056.
3. **S. Kumar**, B. Sarma, A. K. Dasmahapatra, A. Dalal, D. N. Basu, and D. Bandyopadhyay, Field Induced Anomalous Spreading, Oscillation, Ejection, Spinning, and Breaking of Oil Droplets on Strongly Slipping Water Surface, ***Faraday Discussion***, 2017, **199**, 115-128**.**
4. **S. Kumar**, S. Timung, A. Ghosh, A. K. Dasmahapatra, and D. Bandyopadhyay, Dewetting of Microdroplets on Soft Surfaces for Immediate Digitization of Femtoliter Droplets (**Under preparation**).
5. **S. Kumar**, A. K. Dasmahapatra, and D. Bandyopadhyay, Dynamics of the Nanodroplet on gradient surface (**Under preparation**).
6. N. M. Das, **S. Kumar**, D. Bandyopadhyay**,** UV–ozone Mediated Miniaturization of dewetted polymeric Nanostructure on graphene oxide flakes for enhanced raman scattering, ***Carbon,*** 2017, **121**, 612-624.

7. M. Bazant, R. Bennewitz, L. Bocquet, N. Brilliantov, R. Dey, C. Drummond, R. Dryfe, H. Girault, K. Hatzell, K. Kornev, A. A. Kornyshev, I. Kratochvilova, A. Kucernak, M. Kulkarni, **S. Kumar**, A. Lee, S. Lemay, H. Medhi, A. Mount, F. Mugele, S. Perkin, M. Rutland, G. Schatz, David Schiffrin, E. Smela, E. Smirnov, M. Urbakh, and A. Yaroshchuk, Electrotunable wetting, and micro- and nanofluidics: general discussion, ***Faraday Discuss.***, 2017, **199**, 195–237.

6.3.2 Patents

1. International Patent Application: A Point-of-Care Hand Tremor Detection System, Mitradip Bhattacharjee, Dipankar Bandyopadhyay, and **Sunny Kumar**, PCT/IN2017/050366, date of filing 29-08-2017.

2. Indian Patent Application: Mitradip Bhattacharjee, Dipankar Bandyopadhyay, **Sunny Kumar**, A Point-Of-Care Hand Tremor Detection System, Indian Patent Application TEMP/E-1/18774/2017-KOL dated 26-05-2017 (Ref. No 201731018530).

6.3.3 Conferences

1. **S. Kumar,** M. Bhattacharjee, S. Timung, A. K Dasmahapatra and D. Bandyopadhyay "Marangoni effect induced droplet motion for energy harvesting", **EMCA-2014**, CGCRI, Kolkata.
2. **S. Kumar**, S. Thakur, A. K Dasmahapatra and D. Bandyopadhyay "Parametric study of graphene oxide deposition by Langmuir Blodgett trough assembly", **REFLUX - 2015**, IIT Guwahati.
3. **S. Kumar** et al. "Graphene based Micro motor" in **3rd Indo-German Workshop** from 23-26 February 2016 in IIT Guwahati.
4. N.M. Das, **S. Kumar**, D. Bandyopadhyay, UV ozone treated catalytic inhibition of

polystyrene droplets over Graphene Oxide nano sheets, **NANOSMAT-**2016**,** Portugal.

5. B. Sarma, **S. Kumar**, A. Dalal, D. N. Basu, A. K. Dasmahapatra, and D. Bandyopadhyay, "Instability and Breaking of Aqueous Droplet on a Dielectric Coated Electrode", **CompFlu,** 12-14 December 2016, in Hyderabad, India.
6. Md R. Ali Faridi, **S. Kumar**, A. K. Dasmahapatra, D. Bandyopadhyay, "Active liquibot under magnetic field" **Microfluidics, Liquid Handling and Lab on a Chip-2017**" Mumbai, India.
7. **S. Kumar**, B. Sharma, A. Dalal, D. Basu, A. K. Dasmahapatra and D. Bandyopadhyay, "Field Induced Anomalous Spreading, Oscillation, Ejection, Spinning, and Breaking of Oil Droplets on Strongly slipping Water Surface", **Chemical Physics of Electroactive Materials Faraday Discussion,** Cambridge U. K.**,** 2017.
8. **S. Kumar,** A. K. Dasmahapatra, D. Bandyopadhyay, "Dynamics of liquibots under magnetic field", **Research Conclave 2017**, IIT Guwahati, India.
9. S. Mitty, **S. Kumar**, A. K. Dasmahapatra, D. Bandyopadhyay, Wettability of water droplet on PDMS and Graphene micro/nano patterned surface, **ICETINN 2017,** Majitar, Sikkim, India.
10. B. Sharma, **S. Kumar**, A. Dalal, D. Basu, A. K. Dasmahapatra and D. Bandyopadhyay "Directional motion of Nanoparticle Laden Droplets on Micro-Fiber Highway", **Nano India 2017**, IIT Delhi, India.
11. B. Sharma, **S. Kumar**, A. Dalal, D. Basu, A. K. Dasmahapatra and D. Bandyopadhyay "On demand manipulation of nanoparticle laden nanoparticle microdroplets", **Reflux 2017**, IIT Guwahati, India.

12. B. Sharma, **S. Kumar**, A. Dalal, D. Basu, A. K. Dasmahapatra and D. Bandyopadhyay, **"**Morphology of Electrified droplets on dielectric coated electrode", **Research Conclave 2017,** IIT Guwahati, India.

APPENDIX

The linear stability equation (5.3.8) is solved by the given code in Mathematica.

$$\gamma\alpha\theta = 0.032;$$
$$\gamma\theta\beta = 0.046;$$
$$\gamma\alpha\beta = 0.072;$$
$$sol = Solve\left[\begin{matrix}\{\gamma\alpha\theta + \gamma\alpha\beta x + \gamma\theta\beta y == 0, \gamma\alpha\theta y + \gamma\theta\beta + \gamma\alpha\beta z == 0, \gamma\alpha\theta x + \gamma\theta\beta z + \gamma\alpha\beta == 0\}, \\ \{x, y, z\}\end{matrix}\right];$$
$$x1 = Part[x/.sol, 1]; y1 = Part[y/.sol, 1]; z1 = Part[z/.sol, 1];$$
$$\alpha 1r = \arccos[x1];$$
$$\theta 1r = \arccos[y1];$$
$$\beta 1r = \arccos[z1];$$
$$\alpha 1d = \arccos[x1] * \frac{180}{\pi};$$
$$\theta 1d = \arccos[y1] * \frac{180}{\pi};$$
$$\beta 1d = \arccos[z1] * \frac{180}{\pi};$$
$$total = \alpha 1d + \theta 1d + \beta 1d;$$
$$\theta 1 = Pi - \alpha 1r;$$
$$\theta 3 = Pi - \beta 1r;$$
$$\gamma 2 = 0.032;$$
$$\gamma 12 = 0.046;$$
$$\mu 1 = 1.; \mu 2 = 0.01; \mu = \frac{\mu 1}{\mu 2}; r1 = 0.018; r2 = 0.01903;$$
$$sol = NDSolve[\{\left(\gamma 2 * \left(\frac{(3.*h20[r]) - h10[r]}{(2.*h10[r])}\right)\right) h20'''[r] + (\gamma 12 * h10'''[r]) == 0,$$
$$\left(\gamma 2 * \left(\begin{matrix}\left(\frac{\mu * (h20[r] - h10[r])^3}{3.}\right) + \left(((h20[r] - h10[r]) * h10[r]) * \left(h20[r] - \frac{h10[r]}{2.}\right)\right) + \\ \frac{(h10[r])^2}{2.}\left(h20[r] - \frac{h10[r]}{3.}\right)\end{matrix}\right)\right)$$
$$h20'''[r] + \left(\gamma 12 * \left(\frac{(h10[r])^2}{(2.)}\left(h20[r] - \frac{h10[r]}{3.}\right)\right)\right) h10'''[r]) == 0, h20[r1] == 0., h10[r1] == 0.,$$

$h20[r2] == 0., h10[r2] == 0., h20'[r1] == \tan[\theta 1], h10'[r1] == -\tan[\theta 3]\}, \{h10, h20\}, \{r, r1, r2\}];$

$Plot\left[Evaluate\left[\{h10[r], h20[r]\} /. sol \right], \{r, r1, r2\}, PlotRange \to All \right]$

$solh10 = Part\left[Evaluate\left[h10[r] /. sol \right], 1 \right];$

$solh20 = Part\left[Evaluate\left[h20[r] /. sol \right], 1 \right];$

$Write["D:\\data.dat", "Variables = ", "h1", "h2", "r"];$

$Write["D:\\data.dat", "ZONE\ T = ", "Viscosity", "I = "];$

$r11 = r1;$

$count1 = 0;$

$While[(r11 \le r2),$

$h11 = solh10 /. (r \to r11);$

$h21 = solh20 /. (r \to r11);$

$Write\left["D:\\data.dat", OutputForm\left[TableForm\left[\{\{h11, h21, r11\}\}, TableSpacing \to \{0, 6, 6\} \right] \right] \right];$

$If\ [r11 \le 650000, r11 = r11 + 0.0001, r11 = r11 + 0.0001];$

$count1 = count1 + 1;$

]

$Close["D:\\data.dat"];$

$Eq1 = -h20'[r2] /. sol;$

$Eq2 = h10'[r2] /. sol;$

$S1 = Part[Eq1, 1];$

$S2 = Part[Eq2, 1];$

$\theta 2 = Simplify[\arctan[S1]];$

$\theta 4 = Simplify[\arctan[S2]];$

$\theta 2d = \frac{\theta 2 * 180}{\pi};$

$\theta 4d = \frac{\theta 4 * 180}{\pi};$